The University Of Sheffield.

Access to Electronic Thesis

Author:	Deepa Kamath Kasaragod
Thesis title:	Enhanced Contrast in OCT Imaging of Tissues using Birefringence, Scattering and Speckle Signatures
Qualification:	PhD

This electronic thesis is protected by the Copyright, Designs and Patents Act 1988. No reproduction is permitted without consent of the author. It is also protected by the Creative Commons Licence allowing Attributions-Non-commercial-No derivatives.

If this electronic thesis has been edited by the author it will be indicated as such on the title page and in the text.

Enhanced contrast in OCT imaging of tissues using birefringence, scattering and speckle signatures

PhD thesis

by

Deepa Kamath Kasaragod

Submitted in accordance with the requirements for the degree of

Doctor of Philosophy

The University of Sheffield

Department of Materials Science & Engineering

March 2012

Under the supervision of

Dr. Stephen J. Matcher

The work presented in this thesis work was carried out at North Campus, Department of Materials Science and Engineering, University of Sheffield, Sheffield, UK. The author is grateful to EPSRC grant number EP/F020422/1 for the full financial support towards the completion of this project.

I verify that all material included in this thesis work which do not include my own contribution have been acknowledged for and properly referenced.

ABSTRACT

Title: Enhanced contrast in OCT imaging of tissues using birefringence, scattering and speckle signatures

Deepa Kamath Kasaragod

Supervisor: Dr. Stephen J. Matcher, University of Sheffield

The three objectives listed here are the main aim presented in each of the chapters of this thesis. The research work carried out with respect to fulfilling these objectives is one step closer towards extending the possibility of non-invasive imaging modality of OCT and PS-OCT in the field of orthopaedics and tissue engineering.

- Non-invasive technique to understand the depth-dependent 3D collagen framework of articular cartilage.
- Non-invasive technique to discriminate between different types of connective tissue based on angle-resolved backscattering profiles
- Computer based tissue discrimination based on the speckle textural analysis of the OCT images obtained

Articular cartilage was imaged using two different schemes of implementation of PS-OCT: time domain PS-OCT and swept source based continuous polarisation modulation PS-OCT system. Detailed analysis is presented for time-domain PS-OCT data obtained from bovine articular cartilage sample over multi-angle measurements and a comparative study of the phase retardance profiles obtained from experimental data is done with those obtained from a layered model of articular cartilage using extended Jones matrix calculus. This includes a noise model chosen for

the time domain PS-OCT system to add noise bias to the simulated results. Optimiser algorithms are developed based on this model. This study shows the possibility of using PS-OCT imaging towards non-invasive technique to study the microstructure of articular cartilage.

The technique of multi-angle imaging in PS-OCT has also been used in the study of angle-resolved backscattering, with the information regarding the reflectivity profiles as obtained from a normal OCT system used for the study. The two connective tissues under study are bovine tendon sample and bovine articular cartilage sample. Articular cartilage is predominantly made of Type II collagen fibrils which are finer and more uniform in nature compared to that in tendon tissue which is predominantly Type I collagen fibrils of larger diameters and coarser packing arrangements. Single scattering model of OCT is used to obtain the angle-resolved backscattering curves and Rayleigh Gans scattering approximation based simulation is carried out to elucidate and understand the results obtained.

Speckle texture analysis is carried out to extract sub-resolution based information from OCT towards computer-based classification of different types of OCT images. This has been carried out first on tissue phantoms made of agar-intralipid solutions of different concentrations. Statistical features are extracted and grouped into 3-set features to obtain scatter-plots and receiver operating characteristic curves that determine the correctness of the classification obtained of a particular group of OCT images from the total sample set. With initial success from tissue phantom based speckle textural analysis, this has been extended to study the data classification ability of normal skin from tissue engineered skin with different types of melanoma cell-lines invasion as well as discriminate different types of melanoma invasion of tissue-engineered skin from each other.

ACKNOWLEDGEMENTS

A note of gratitude to……..

Dr. Steve Matcher for being an excellent critic of my research work, the guidance and supervision of my PhD work.

Dr. Marco Bonesi, Dr. Nikola Krstajic & Dr. Louise Smith, previous group members for their support and help

Dr. James Jacobs & Dr. Zenghai Lu for their help and support with the use of OCT systems and for the wonderful time working together.

Dr. Aileen Crawford & Dr. Rebecca Goodchild for help with bovine sample collection and dissection

Prof. Richard Hogg & his group members for a wonderful working environment

EPSRC for the funding support

All my friends and housemates who have contributed in some way or the other to make my life abroad eventful.

My family for their patience and emotional support throughout my PhD studies.

Deepa

TABLE OF CONTENTS

LIST OF FIGURES

LIST OF TABLES

OVERVIEW

Chapter 1 is the introduction chapter that describes the mathematical techniques and formulations used in polarisation optics for the study and analysis of polarised light and its interaction with any medium (isotropic or anisotropic). Polarised light and its interaction and the resulting effects in biological tissues are also given. A brief description of the theory, applications as well as development in the field of OCT and PS-OCT is also presented. A detailed description of polarised light interaction in collagen fibres in articular cartilage is also presented along with a detailed description of the background and research and discussions on the 3D complicated organisation of collagen fibres in articular cartilage and the relevance and current status of study of OCT imaging on articular cartilage is given.

Chapter 2 gives a detailed theoretical description of the two PS-OCT systems used for the study presented in this thesis: a bulk optics based time domain PS-OCT and a continuous polarisation modulation swept source based PS-OCT system. The EJMC used as a theoretical basis to study multi-layered birefringent biological tissues like articular cartilage is explained in detail followed by the PS-OCT experimental details and their analysis. This includes the contents published in the following journal

"Kasaragod et al., (2011). Theoretical framework for the analysis of optical anisotropy in birefringent biological tissues with polarization-sensitive optical coherence tomography. Optical Coherence Tomography and Coherence Techniques V, 8091".

"Kasaragod et al., (2012). Experimental validation of an extended Jones matrix calculus model to study the 3D structural orientation of the collagen fibers in articular cartilage using polarization-sensitive optical coherence tomography, Bio. Med. Opt. Exp.,"Vol. 3, Iss. 3, pp. 378-387."

Chapter 3 reports a comparative study of the angle-resolved back-scattering profiles obtained from OCT for two different types of collagen fibres found in tendon and articular cartilage and its implications is being described with comparative studies carried out using Rayleigh-Gans scattering approximation. This includes the contents published in the following journal

"Kasaragod et al., (2011). Comparative study of the angle-resolved backscattering properties of collagen fibers in bovine tendon and cartilage. J Biomed Opt, 16(8), 080501".

Chapter 4 deals with the a study to the possibility of implementation of automated detection of the OCT images of different concentrations of agar-Intralipid solutions as well as different types of melanoma invasion in tissue engineered skin based on the speckle texture analysis of the OCT images obtained. This is covered in the conference proceeding

"Kasaragod et al., (2010). Speckle texture analysis of optical coherence tomography images. Speckle 2010: Optical Metrology, 7387"

Chapter 5 discusses the results and conclusions of the main results reported in the above chapters. A brief summary of the overall work presented in this thesis is given with a short discussion on the further scope of work that could be carried out based on the conclusions and insight gained from the research work carried out so far.

CHAPTER 1

Background and Introduction

1.1. Summary

In this chapter, an introduction to the different aspects of mathematical representation of the polarised light is given followed by an introduction to the polarisation properties of biological tissues and its interpretation. In short, a description of the following is given in this chapter: Jones matrix, Stokes-Mueller matrix, Poincare sphere as well as quaternion and group theoretical approach. A brief introduction to the theory, applications and development of OCT modality is given. Further on moving to the area of polarisation sensitive detection based on OCT imaging modality: polarisation-sensitive optical coherence tomography (PS-OCT). An insight into the 3D collagen network of articular cartilage and the previous work carried out to study the microstructure of articular cartilage as well as the relevance of OCT imaging in this respect is discussed towards the end of this chapter.

1.2. Introduction

A light wave is transverse in nature with the direction of the propagation of the light beam perpendicular to the mode of the vibration of the wave. A unique characteristic property of the transverse nature is polarisation property possessed by the wave which describes the mode of oscillations described by these waves. Depending on how the extremity of the electric field vector changes over time, an electromagnetic wave could be classified as polarised, partially polarised or unpolarised. The polarimetric formalism that describes the transformation of the electromagnetic beam of light upon interaction with the media of propagation helps us to obtain information about the nature of the medium based on the change in the polarisation state occurring. Polarisation changes also occur in different phenomena occurring in nature including, scattering, reflection, selective absorption including dichroism as well as double refraction in certain crystals like quartz, calcite, etc. These effects also manifest in the biological tissue samples as changes in polarisation response which forms the main basis of the research work presented in this thesis. Starting from the early 19^{th} century, different formalisms have been introduced to study the polarimetric response of a system using mathematics as the tool. In no particular order, these formalisms are being discussed in Section 1.2. Particular importance is given to the representation of a birefringent element (a retarder) which is the most common representation that is dealt here in the study of the polarimetric response of the biological tissues using PS-OCT system.

1.3. Mathematical representation of polarized light and polarisation effects:

1.3.1. Jones formalism:

In a sequence of journal papers titled "A new calculus for the treatment of optical systems" starting from year 1941, Jones described a new mathematical treatment to describe polarisation of a coherent system. For a completely polarised light, the electric vector was described as a 2×1 matrix in terms of orthonormal basis vectors as

$$\begin{pmatrix} E_x \\ E_y \end{pmatrix} = \begin{pmatrix} a_x e^{-i\delta_x} \\ a_y e^{-i\delta_y} \end{pmatrix} \tag{1.1}$$

Any non-depolarising optical element could be described using Jones matrix which is a 2×2 matrix that relates the incident polarisation state of the light to the output polarisation state of the light upon propagation through the optical element. It is given as:

$$\begin{pmatrix} E_x^{'} \\ E_y^{'} \end{pmatrix} = \begin{pmatrix} J_{11} & J_{12} \\ J_{21} & J_{22} \end{pmatrix} \begin{pmatrix} E_x \\ E_y \end{pmatrix} \tag{1.2}$$

In general, any elliptical retarder can be described using three parameters, the phase retardance between the two electric field components δ, orientation angle θ of the polarisation state and circularity ϕ, given by:

$$J_{ellipticalretarder} = \begin{pmatrix} e^{i\delta/2}\cos^2\theta + e^{-i\delta/2}\sin^2\theta & (e^{i\delta/2} - e^{-i\delta/2})\cos\theta\sin\theta e^{-i\phi} \\ (e^{i\delta/2} - e^{-i\delta/2})\cos\theta\sin\theta e^{i\phi} & e^{i\delta/2}\sin^2\theta + e^{-i\delta/2}\cos^2\theta \end{pmatrix} \tag{1.3}$$

which for a linear retarder ($\phi = 0$)reduces to

$$J_{linearretarder} = \begin{pmatrix} e^{i\delta/2}\cos^2\theta + e^{-i\delta/2}\sin^2\theta & (e^{i\delta/2} - e^{-i\delta/2})\cos\theta\sin\theta \\ (e^{i\delta/2} - e^{-i\delta/2})\cos\theta\sin\theta & e^{i\delta/2}\sin^2\theta + e^{-i\delta/2}\cos^2\theta \end{pmatrix} \tag{1.4}$$

which is a unitary representation of waveplate and rotators as put forward by Jones to completely characterise a birefringent element. This formalism is however limited to the optical systems that are not depolarising in nature and cannot be used to describe partially polarised light.

1.3.2. Stokes vectors:

Stokes parameters describe the polarisation state of any electromagnetic beam in terms of its intensity. Also, any type of light beam: polarised, unpolarised or partially polarised could be represented using this notation.

Table 1.1: Jones and Stokes vectors for various types of polarised light beam

Polarised nature of the light beam	Jones Vectors	Stokes Vectors
Linearly polarised	$\begin{pmatrix}1\\0\end{pmatrix}\begin{pmatrix}0\\1\end{pmatrix}$	$\begin{pmatrix}1\\1\\0\\0\end{pmatrix}\begin{pmatrix}1\\-1\\0\\0\end{pmatrix}$
Linearly polarised with fast axis oriented at 45^{o}	$\frac{1}{\sqrt{2}}\begin{pmatrix}1\\1\end{pmatrix}\frac{1}{\sqrt{2}}\begin{pmatrix}1\\-1\end{pmatrix}$	$\begin{pmatrix}1\\0\\1\\0\end{pmatrix}\begin{pmatrix}1\\0\\-1\\0\end{pmatrix}$
Circularly polarised	$\frac{1}{\sqrt{2}}\begin{pmatrix}1\\i\end{pmatrix}\frac{1}{\sqrt{2}}\begin{pmatrix}1\\-i\end{pmatrix}$	$\begin{pmatrix}1\\0\\0\\-1\end{pmatrix}\begin{pmatrix}1\\0\\0\\1\end{pmatrix}$
Unpolarised	-	$\begin{pmatrix}1\\0\\0\\0\end{pmatrix}$

The four Stokes parameters are generally represented using the notation

$$\vec{S} = \begin{pmatrix} I \\ Q \\ U \\ V \end{pmatrix} \text{or} \begin{pmatrix} S_0 \\ S_1 \\ S_2 \\ S_3 \end{pmatrix} \tag{1.5}$$

$$\begin{aligned} I &= E_x E_x^* + E_y E_y^* = A_x^2 + A_y^2 \\ Q &= E_x E_x^* - E_y E_y^* = A_x^2 - A_y^2 \\ U &= E_x E_y^* + E_y E_x^* = 2A_x A_y \cos\delta \\ V &= i(E_x E_y^* - E_y E_x^*) = 2A_x A_y \sin\delta \end{aligned} \tag{1.6}$$

where $\delta = \delta_x - \delta_y$.

Stokes representation along with the Mueller formalism described below henceforth gives a general description of any polarisation state of the electromagnetic wave. Also, the Poincare representation described in Section 1.3.4 is the geometrical representation of the polarisation nature of the electromagnetic beam based on the Stokes parameters which is described in detail.

1.3.3. Mueller matrices:

Mueller matrix representation is a 4×4 matrix that transforms the incident Stokes vector to the output Stokes vector upon propagation through an optical element.

$$\vec{S}_{out} = \begin{pmatrix} I_{out} \\ Q_{out} \\ U_{out} \\ V_{out} \end{pmatrix} = \begin{pmatrix} m_{11} & m_{12} & m_{13} & m_{14} \\ m_{21} & m_{22} & m_{23} & m_{24} \\ m_{31} & m_{32} & m_{33} & m_{34} \\ m_{41} & m_{42} & m_{43} & m_{44} \end{pmatrix} \begin{pmatrix} I_{in} \\ Q_{in} \\ U_{in} \\ V_{in} \end{pmatrix} = M\vec{S}_{in} \tag{1.7}$$

Thus, Mueller matrix possess 16 independent parameters at the maximum unlike Jones matrix which has seven independent parameters to define an optical element for its real and imaginary parts over four matrix elements. Every Jones matrix has an equivalent Mueller matrix given by:

$$M = U(J \otimes J^*)U^{-1} \tag{1.8}$$

$$U = \begin{pmatrix} 1 & 0 & 0 & 1 \\ 1 & 0 & 0 & -1 \\ 0 & 1 & 1 & 0 \\ 0 & i & -i & 0 \end{pmatrix} \tag{1.9}$$

However, only non-depolarising Mueller matrix could be transformed back to corresponding Jones matrix (Le Roy-Brehonnet *et al.,* 1997).

1.3.4. Poincare sphere:

Poincare sphere relates the ellipsometric parameters to the Stokes vectors in a 3D space as follows:

$$\begin{aligned} I &= c^2 \\ Q &= c^2 \cos 2\varepsilon \cos 2\theta \\ U &= c^2 \cos 2\varepsilon \sin 2\theta \\ V &= c^2 \sin 2\varepsilon \end{aligned} \tag{1.10}$$

with $\tan 2\theta = \frac{U}{Q}$ and $\tan 2\varepsilon = \frac{V}{\sqrt{Q^2 + U^2}}$

where, 2θ and 2ε determine the latitude and longitude in a Poincare sphere (Figure 1.1).

On a sphere of unit radius, the polarisation state is represented by a vector $\vec{S} = \begin{pmatrix} Q/I \\ U/I \\ V/I \end{pmatrix}$ and magnitude of this vector defines the degree of polarisation (DOP)

$$DOP = \frac{\sqrt{Q^2 + U^2 + V^2}}{I} \qquad 1.11$$

The points on the Poincare represents the normalised Stokes vectors and for any polarising element representing the linear birefringent element or diattenuation, the optic axis lie in the Q-U plane (Park *et al.*, 2005b)

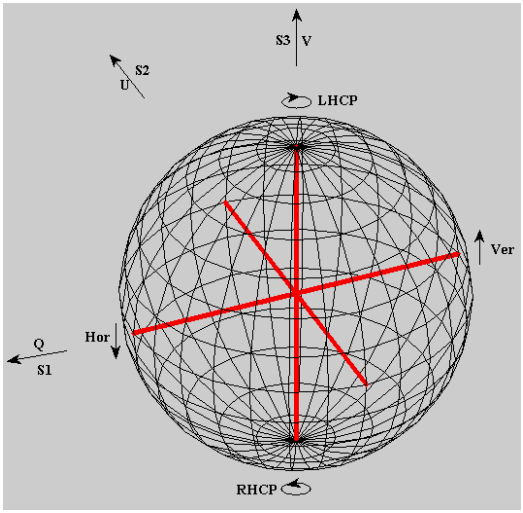

Figure 1.1: Poincare sphere for the representation of polarisation state in terms of Stokes vectors.

1.3.5. Other approaches

Although the above mentioned formalisms have build up a stance in polarisation optics analysis, certain vector field algebraic methods used in polarisation optics is also worth including in here in this chapter. It includes the quaternion approach (Richartz & Hsu, 1949)

and Pauli-algebraic method using the 2×2 basis matrices commonly known as Pauli's spin vectors (Whitney, 1971). These approaches however could be related to different aspects of group theoretical approach to studying polarisation optics.

A quaternion could be written based on the complex numbers $Q = q_0 + iq_1 + jq_2 + kq_3$ which follows the identity $i^2 = j^2 = k^2 = ijk = -1$.

Expressed in 2×2 or 4×4 form, quaternion could also be given as:

$$Q = \begin{pmatrix} q_0 + iq_3 & iq_1 - q_2 \\ iq_1 + q_2 & q_0 - iq_3 \end{pmatrix} or \begin{pmatrix} q_0 & -q_1 & -q_2 & -q_3 \\ q_1 & q_0 & -q_3 & q_2 \\ q_2 & q_3 & q_0 & -q_1 \\ q_3 & -q_2 & q_1 & q_0 \end{pmatrix} \qquad 1.12$$

This could also be expressed in terms of Cayley-Klein parameters as

$$Q = \begin{pmatrix} q_0 + iq_3 & iq_1 - q_2 \\ iq_1 + q_2 & q_0 - iq_3 \end{pmatrix} = \begin{pmatrix} \alpha & \beta \\ \gamma & \delta \end{pmatrix} \qquad 1.13$$

Hence, this represents the operation in SU(2) in group theoretical approach which is similar to the Jones matrix approach given for birefringence analysis. However, rotation element is expressed using quaternion representation which is equivalent to Mueller matrix approach as well as the O^{3+} rotation in 3D space in group theory.

$$Q = a\sigma_0 + i(x\sigma_1 + y\sigma_2 + z\sigma_3) \qquad 1.14$$

Any retarder or rotator (unitary matrix) could be written as a linear superposition of Pauli's spin matrices given by:

$$U = a_0\sigma_0 + a_1\sigma_1 + a_2\sigma_2 + a_3\sigma_3 \qquad 1.15$$

where, $\sigma_0 = \begin{pmatrix} 1 & 0 \\ 0 & 1 \end{pmatrix}$ is the identity matrix and $\sigma_1 = \begin{pmatrix} 1 & 0 \\ 0 & -1 \end{pmatrix}, \sigma_2 = \begin{pmatrix} 0 & 1 \\ 1 & 0 \end{pmatrix}, \sigma_3 = \begin{pmatrix} 0 & -i \\ i & 0 \end{pmatrix}$ are the Pauli's spin matrices used in quantum optics , which is also equivalent to quaternion approach as

$$Q = q_0 + iq_1 + jq_2 + kq_3 = q_0\sigma_0 + q_1.(i\sigma_1) + q_2.(i\sigma_2) + q_3.(i\sigma_3) \qquad 1.16$$

1.4. Polarimetric response of biological tissues.

Section 1.3 gives an introduction to all the available mathematical tools that are used to study the polarimetric response of the system under investigation. This section describes how to put into application these mathematical tools to understand the polarimetric response of biological tissues.

1.4.1. Linear and Circular birefringence

Any polarised light beam consists of two orthogonal components which interact with the optical medium differently depending on the nature of the medium. Biological tissues are often treated as anisotropic medium which implies that the two orthogonal components of the polarized light beam encounter different refractive index for its propagation along the media. This can be referred to as two modes called the ordinary and the extraordinary modes similar to the double refraction effects seen in anisotropic crystal. The two modes henceforth propagate at different speed along the medium and the direction of higher refractive index is termed the slow axis and the orthogonal direction with smaller refractive index as the fast axis. The typical range of difference of the two refractive indices in biological tissues lies around $0 - 6\times10^{-3}$. The term $\Delta n = n_e - n_o$ is called the linear birefringence of the medium.

Circular birefringence is seen as the difference in the refractive indices as seen by circularly polarised light when it passes through an optical medium. This in effect is manifested as a rotation of the linear polarisation of the incident light beam as any linear polarised light could be effectively decomposed to a combination of right and left circular polarised light. However, in this thesis circular birefringence is not dealt with owing to the fact that circular birefringence effect is cancelled out in the double pass propagation occurring in OCT image acquisition.

1.4.2. Form and Intrinsic birefringence

The reason for the manifestation of linear birefringence in biological tissues could be attributed to two main factors. Intrinsic birefringence is related to the compact helical molecular structural ordering found in biomolecules, which leads to the dipole moment due to the anisotropic charge distribution based on the geometry of molecular arrangement. Form birefringence is more to do with the nature of ordering of the crystalline structure of biomolecules or fibrils as embedded in a background medium of different refractive index. Although the origin of these two mechanisms is different, they are based on length scales well below the wavelength of light being used in investigation.

1.4.3. Apparent and True Birefringence

Collagen is the most common component of the fibrous tissue found in the extracellular matrix of the connective tissue. It is commonly found in tissues like tendon, ligament, skin, cartilage, intervertebral disc, bone, cornea, blood vessels, etc. Collagen fibre is the main subject of investigation in the work discussed in this thesis. Collagen fibril could be thought of as a uniaxial positive birefringent crystal, which possess two modes of light beam propagation one along the long axis of the fibre and the other orthogonal to the long axis.

Bringing in the concept of anisotropic crystal optics, Ugryumova *et al.* came forward with the terms: true birefringence and apparent birefringence which discusses the dependence of the obtained birefringence on the angle the incident light beam makes with the optic axis (Ugryumova *et al.*, 2005). As pictorially shown in the Figure1.2, the obtained apparent birefringence is a function of the angle which the incident beam of polarized light makes with the long axis of the collagen fibril. Hence, true birefringence is given by $\Delta n = n_e - n_o$ and apparent birefringence is obtained as $n - n_o$, where n is given by the optical indicatrix equation as:

$$\frac{1}{n^2} = \frac{\sin^2 \theta_c}{n_e^2} + \frac{\cos^2 \theta_c}{n_o^2} \qquad 1.17$$

with θ_c describing the angle that the long axis of collagen fibril makes with incident light beam. Henceforth, it would be possible to extract information regarding the arrangement of the collagen fibrils in a biological tissue based on the apparent birefringence obtained at multiple angles of incidence of the light beam. A description of how this concept is used in our study to extract depth-resolved information about the 3D structural orientation of collagen fibres in the complicated structure of articular cartilage is described in detail in chapter 2.

1.4.4. Phase retardance:

Phase retardance is how the linear birefringence gets represented in a PS-OCT image. Linear birefringence induces a difference in the phase as the two modes propagate along the anisotropic optical medium which is given by

$$\delta = \frac{2\pi}{\lambda} \Delta n z \qquad 1.18$$

Where δ is the phase retardance seen over a depth of propagation of z in a medium of birefringence Δn. This is manifested owing to the fact that refractive index of the material studied is dependent on the polarisation state of the light beam incident on it. The phase retardance appears as banding patterns in the retardance images obtained using PS-OCT and the nature of banding depends on the type of the tissue as well the direction of the incident beam onto the sample. That is high apparent birefringence is obtained when viewed along the direction orthogonal to the collagen fibres and low apparent birefringence when imaged in the direction of the long axis of the collagen fibres (Figure 1.2).

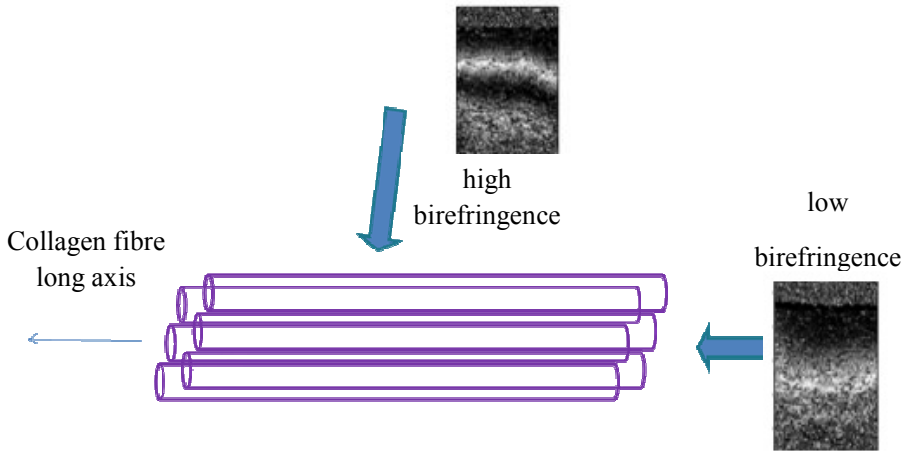

Figure 1.2: Pictorial depiction of the apparent birefringence seen in articular cartilage when the obtained birefringence varies depending on the angle which the wave vector of incident beam of light makes with the optic axis of the collagen fibre

Thus phase retardance images obtained over multi-angles of incidence gives an overall picture of the orientation of the collagen fibres in a biological tissue including the depth resolved orientation information. Chapter 2 gives a detailed description of the theory behind use of phase retardance images to extract depth-resolved information about collagen fibre axis orientation.

1.4.5. Diattenuation/Dichroism:

Dichroism is the differential absorption properties shown by anisotropic material which is manifest as the differential absorption coefficients for the two orthogonal components of the light beam that leads to change in the polarisation state of the light interacting with the media. Thus if P_1 and P_2 are the electric field attenuation coefficients for the Eigen polarisation states then, diattenuation, d could be given by:

$$d = \frac{P_1^2 - P_2^2}{P_1^2 + P_2^2} \qquad 1.19$$

Kemp *et al.* coins the term biattenuance to describe the differential absorption of propagating modes of light in anisotropic media owing to dichroism or scattering effects (Kemp *et al.*, 2005). While polarisation dependence of real part of refractive index of the anisotropic material leads to birefringence effect, dichroism is the result of polarisation dependence of imaginary part of refractive index that describes the attenuation factor of propagation. Diattenuation measurements in biological samples have been reported by various research groups (Jiao *et al.*, 2003a; Park *et al.*, 2004; Todorovic *et al.*, 2004). Park *et al.* have carried out detailed analysis regarding diattenuation in chiken muscle and tendon and have shown that birefringence calculations would not be greatly affected if diattenuation effects are ignored (Park*, et al.*, 2004). Also, as OCT wavelengths do not fall under the strong absorption spectrum of light in the biological tissues, diattenuation characterisation in biological samples are not considered relevant for PS-OCT based studies (Park *et al.*, 2006).

1.5. Optical Coherence Tomography:

Optical coherence tomography is the optical analogue version of ultrasound based on low coherent interferometric detection of back scattered light. The interferometer involved could be a Michelson or Mach-Zender interferometer. This was developed as an extended concept from the optical coherence domain reflectometry which provides location information with regard to the delay seen in the optical backscattering (Huang *et al.*, 1991). When applying this concept to the tomographic imaging of biological tissues, the same concept of low-coherence gating yields the depth-resolved data (A-scans) followed by a series of lateral scans called the B-scans that yield the tomographic image over a certain location of the tissue being imaged. The broadband light source used, owing to the recent developments in semiconductor optics (Fercher *et al.*, 2003; Unterhuber *et al.*, 2004), provides the necessary axial resolution of the imaging given by:

$$\Delta l = \frac{2\ln 2}{\pi}\frac{\lambda^2}{\Delta\lambda} \tag{1.20}$$

where, $\Delta\lambda$ is the bandwidth of the light source centred at wavelength λ.

while, the detection optics is responsible for the lateral resolution as described by

$$\Delta l_{lat} = 2\sqrt{\ln 2}\,\frac{\lambda}{\pi\theta_s} \tag{1.21}$$

where, θ_s gives the angular spread of the beam based on the numerical aperture of the lens used.

This is a main feature of this optical imaging technique compared to confocal microscopy based imaging with axial and lateral resolution independent of each other. Since its inception

in 1991, based on the first paper by Huang *et al.* (Huang, *et al.*, 1991) OCT have come a long way from research based applications in to commercial product launched in the field of ophthalmology. Several functional imaging modalities based on OCT have also come up including Doppler OCT (Chen *et al.*, 1997; Izatt *et al.*, 1997), spectroscopy based OCT (Leitgeb *et al.*, 2000; Schmitt *et al.*, 1998), polarization-sensitive OCT (de Boer & Milner, 2002). There are two important schemes of OCT: time domain OCT and Fourier domain OCT. These two schemes are just the differences pertaining in the implementation owing to data acquisition in either time domain or Fourier domain and are equivalent to each other owing to the applicability of Wiener-Khintchine theorem.

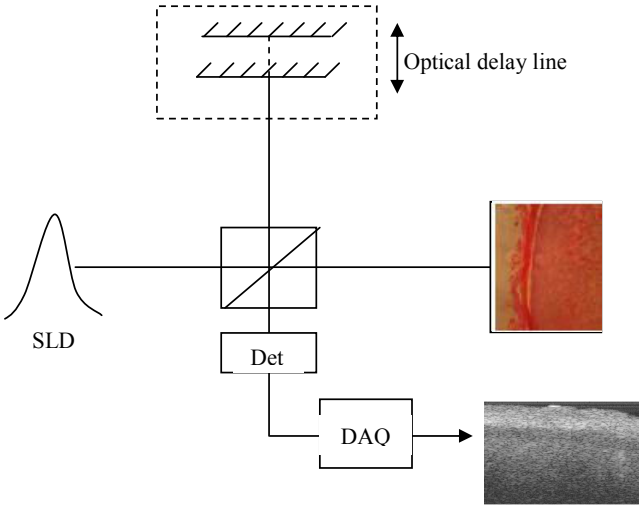

Figure 1.3: Schematic of the time domain OCT system; SLD- low coherence superluminescent diode, DAQ- Data acquisition card, Det- Detectors.

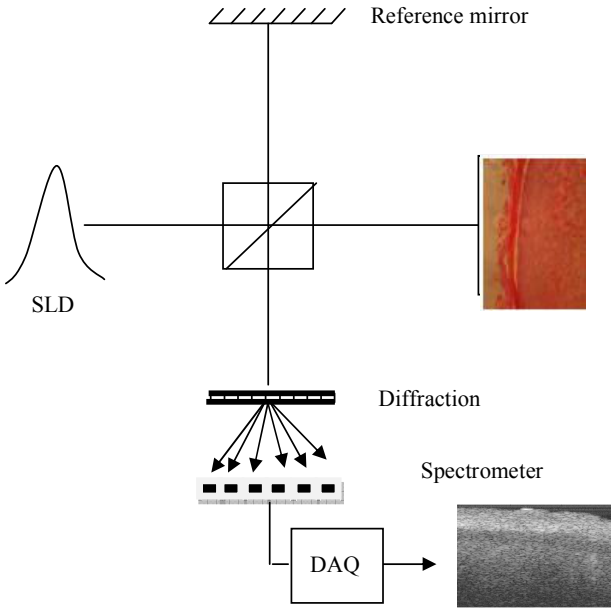

Figure 1.4: Schematic of the Fourier domain OCT system; SLD- low coherence superluminescent diode, DAQ- Data acquisition card.

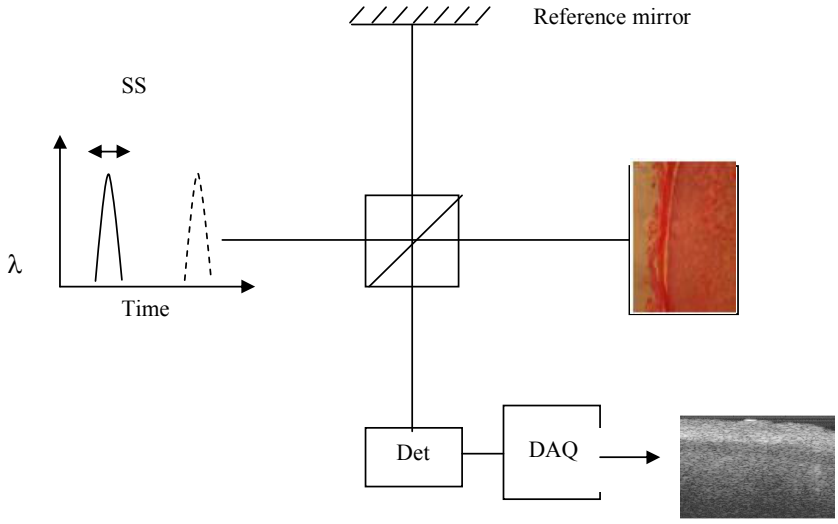

Figure 1.5: Schematic of the Swept source based OCT system; SS – wavelength sweeping laser source, DAQ- Data acquisition card, Det- Detectors.

Fourier domain OCT system could be broadly classified again into two types of implementation: Spectral domain OCT and swept-source OCT. Pictorial description of all the three implementations is given (Figure 1.3 - 1.5).

In this study, two imaging systems based on the polarisation-sensitive detection version of OCT is used. One is a bulk optics based time domain PS-OCT and the other is a fibre-based swept source based PS-OCT. A brief overview of PS-OCT is provided in the next section.

1.6. Polarisation-sensitive optical coherence tomography

PS-OCT system could mainly analyse the polarisation changes occurring due to the following main mechanisms:

1. Depolarisation or polarization scrambling (Gotzinger *et al.,* 2008; Pircher *et al.,* 2004a, 2004b; Pircher *et al.,* 2004c)
2. Birefringence which could be form birefringence or intrinsic birefringence as discussed in the sections above. (Baumgartner *et al.*, 2000; de Boer *et al.*, 1997; Everett *et al.*, 1998)
3. Diattenuation (Kemp*, et al.*, 2005; Park*, et al.*, 2004; Todorovic*, et al.*, 2004)

It was based on the linear algebraic treatment of the Jones matrix that the concept of polar decomposition was introduced (Whitney, 1971). This decomposition helps us to obtain the parameters that characterises the retardance and transmission properties of the optical medium.

Polar decomposition of the Jones matrix gives us the factorisation into two matrices as follows:

$$J = J_P J_R = J_R J_P^{'} \tag{1.22}$$

where, J_R is a unitary matrix representing a retarder and $J_P, J_P^{'}$ is the Hermitian matrix that represents a polariser (Lu & Chipman, 1994). Birefringence information of the tissue is obtained from J_R, which is dependent on three parameters as given in Equation 1.3, where δ gives the phase retardance value. Diattenuation described by J_P is given by Equation 1.19 and the analysis with respect to PS-OCT imaging is often simplified using the assumption that the birefringence and attenuation share a common optic axis (Jiao & Wang, 2002b).

Moreover, singular value decomposition could be used to reduce the matrix, J to the following

$$J = STV^{\dagger} \tag{1.23}$$

where, $J_R = SV^{\dagger}$, $J_P = VTV^{\dagger}$ and $V^{\dagger}, S$ are unitary matrices. Using a simpler matrix decomposition scheme based on matrix diagonalisation, the values of relative optic axis orientation, birefringence and diattenuation are obtained from a PS-OCT system as described in Equation 2.26 in Section 2.4 of Chapter 2.

First paper reporting on PS-OCT implementation was by Hee *et al.* in 1992, in which they have reported it as an extension of an optical coherence-domain interferometer system capable of giving depth-resolved phase difference information of a birefringent biological sample with high spatial resolution (Hee *et al.,* 1992). This was reported on an 830nm zero-order quarter wave plate, a longitudinal KDP based electro optic modulator and calf coronary artery. This concept of polarisation-sensitive detection was combined with an OCT system at around 800nm by de Boer *et al.* in 1997 to obtain 2D birefringence image of bovine tendon

(de Boer*, et al.*, 1997). They also reported on change in the birefringence of the bovine tendon sample upon thermal irradiation using laser pulses. The polarisation analysis used in these systems was based on Jones matrix formalism. One of the systems used for the study reported here is based on this implementation scheme of first generation bulk optics based TD-PS-OCT system, the theoretical details of which would be discussed in greater details in Chapter 2. Everett *et al.* first reported on a 1.3μm wavelength based PS-OCT system introducing single mode fibres to couple bulk optics system to detectors in a PS-OCT system. Birefringence data in porcine myocardium was discussed (Everett, *et al.,* 1998). de Boer *et al.* further substantiate the potential of PS-OCT for carrying out burn depth assessment in 1998 paper on PS-OCT studies on porcine tendon and skin by showing the reduction of birefringence upon denaturation of collagen fibres during thermal damage of the tissue (de Boer *et al.*, 1998). A detailed analysis on the noise present during the birefringence measurements using a time domain PS-OCT system was presented by Schoenenberger *et al.* which included a detailed theoretical analysis on the sources of systematic noise (Schoenenberger *et al.,* 1998). With adoption of coherent detection scheme in PS-OCT, de Boer *et al.* used depth resolved Stokes parameters to study birefringence. (de Boer *et al.,* 1999). Yao *et al.* introduced for the first time the concept of Mueller matrices characterize the polarisation properties exhibited by the biological tissues using PS-OCT system (Yao & Wang, 1999). However, Jiao *et al.* simplified the whole procedure of interpreting 16 images in a Mueller based PS-OCT system, with the study showing that OCT detection is non-depolarizing which implies simpler calculus method based on Jones matrix could provide full information from a PS-OCT system (Jiao & Wang, 2002a; Jiao *et al.*, 2000). Based on the phase sensitive detection adopted in TD-PS-OCT, Hitzenberger *et al.* devised a formula to obtain the relative optic axis measurements from the system (Hitzenberger *et al.*, 2001). It

was also put forward by Jiao *et al.* that the full orientation details could be obtained from PS-OCT studies with the use of two orthogonal pair of light polarisation states in the system. This idea was extended with a dual beam set up with use of two SLED's with orthogonal polarisation state incident onto the interferometer (Jiao & Wang, 2002b).

With the technological advances in the optical design of OCT system, fibre based implementations of OCT systems were launched which paved the way for *in-vivo* imaging and flexibility towards clinical applications (Park *et al.*, 2001; Roth *et al.*, 2001; Saxer *et al.*, 2000). The misinterpretation of birefringence measurements in fibre based system with random birefringence of single mode fibres used were studied and various solutions were provided. This included implementation of PS-OCT system with polarisation maintaining fibres (Zhang *et al.*, 2003), surface calibration technique to account for fibre birefringence (Jiao *et al.*, 2003b; Park*, et al.*, 2004). Jiao *et al.* put forward the surface calibration technique for their Mueller matrix based PS-OCT implementation (Jiao*, et al.*, 2003b). Similar scheme was adopted by Park *et al.* for the Jones matrix based PS-OCT system to avoid the fibre birefringence affecting the birefringence measurements of the sample (Park*, et al.*, 2005b).This implementation has been adopted in the fibre based system used for our study described in Chapter 2 (Lu *et al.*, 2011).

Higher sensitivity and imaging speeds compared to TD-PS-OCT systems were obtained by the advent of Spectral Domain PS-OCT (SD-PS-OCT) systems (Choma *et al.*, 2003; de Boer *et al.*, 2003; Leitgeb *et al.*, 2003). Gotzinger *et al.* 2005 used two separate spectrometers to record the orthogonal polarisation signals in their SD-PS-OCT system (Gotzinger *et al.*, 2005). Other groups have also demonstrated similar SD-PS-OCT using two spectrometers at 840nm as well as 1300nm (Chen *et al.*, 2005; Park *et al.*, 2005a). Additional cost issues of

using two spectrometers and the requirement for synchronisation between the two to avoid artefacts in birefringence analysis prompted the implementation reported with single line scan camera detection. Different schemes have been reported in literature with regard to single line scan camera detection for SD-PS-OCT. (Baumann *et al.*, 2007; Cense *et al.*, 2007; Fan *et al.*, 2007; Fan & Yao, 2010; Oh *et al.*, 2008; Schmoll *et al.*, 2010; Yasuno *et al.*, 2002; Zhao & Izatt, 2009)

Jiao *et al.* introduced the concept of continuous polarisation modulation in TD-PS-OCT systems, which allowed for acquisition of Jones matrix of the sample from a single A-scan measurement as it was equivalent to sequential measurement with varying incident polarisation states (Jiao *et al.*, 2005). This concept was adopted by Yamanari *et al.* for a Fourier domain implementation of the scheme with modulation along the B-scan (Yamanari *et al.*, 2006). The second system used for the study reported here is a swept source based continuous polarisation modulation based PS-OCT system following the scheme implemented by Yamanari *et al.* (Yamanari *et al.,* 2008) but with certain component upgrades as detailed in Chapter 2. However, one of the drawback of this type of implementation is the inability to use full range of the imaging depth owing to the use of the real-valued cosine transform rather than the complex-valued Fourier transform for obtaining signal (Wojtkowski *et al.*, 2002). The conjugacy artefact could be avoided using higher speed digitiser and polarisation frequency with the implementation details given in Chapter 2. The other methods that could be used for full range measurements by removing the mirror images obtained in Fourier domain OCT include implementation schemes with use of phase modulator (Zhang *et al.*, 2004), frequency shifter (Davis *et al.*, 2005), 3×3coupler (Sarunic *et al.*, 2005), numerical dispersion encoding method (Hofer *et al.*, 2009; Hofer *et al.*, 2010), phase modulation along B-scan (Fan*, et al.*, 2007; Yamanari *et al.*, 2010; Yasuno *et al.*, 2006).

Over years, different schemes of PS-OCT system implementations have been reported (Al-Qaisi & Akkin, 2008, 2010; Gotzinger *et al.*, 2009; Liu *et al.*, 2009; Moneron *et al.*, 2007; Wang *et al.*, 2010).

1.7. Applications of PS-OCT:

As a functional extension of structural imaging of OCT, PS-OCT has wide applications in biological and non-biological applications. These include application to burn depth imaging in skin with a loss of birefringence during thermal damage (de Boer*, et al.*, 1998; Jiao*, et al.*, 2003a; Park*, et al.*, 2001; Schoenenberger*, et al.*, 1998; Srinivas *et al.*, 2004; Todorovic *et al.*, 2008), cornea (Fanjul-Velez *et al.,* 2010; Gotzinger *et al.,* 2004; Hitzenberger *et al.,* 2006), Retinal imaging (Cense *et al.,* 2009a; Cense *et al.,* 2009b; Ducros *et al.,* 2001; Gotzinger, *et al.,* 2008; Pircher *et al.,* 2006), coronary plaque assessment in atherosclerosis (Giattina *et al.,* 2006; Kuo *et al.,* 2007; Nadkarni *et al.,* 2009), dentistry (Baumgartner, *et al.,* 2000; Fried *et al.,* 2002; Jones *et al.,* 2006) endoscopy (Pierce *et al.,* 2005), muscular dystrophy (Pasquesi *et al.,* 2006) and osteoarthritis .

In the later sections the study carried out on articular cartilage and osteoarthritis using PS-OCT will be discussed in greater details. The main theme of investigation in this thesis is the application of PS-OCT to the study of articular cartilage. Chapter 2 presents the detailed study carried out in analysing the PS-OCT data to understand the microstructure of articular cartilage and the possibility of carrying out further studies to establish the possibility of application of PS-OCT imaging towards understanding the subsequent changes that could occur in the birefringence information with the onset of osteoarthritis and its progression.

1.8. Articular cartilage:

Cartilage tissue found in animal body is broadly categorized under three types: elastic, hyaline and fibrocartilage. Section 3.2 of Chapter 3 discusses in more detail on the types of connective tissues and their dominant constituents. The cartilage found on the surface of the articulating joints called the articular cartilage is made of hyaline cartilage. This provides for the compressive and resistive powers during joint movement. Articular cartilage is mainly avascular in nature with nutrients for cell growth provided by diffusion process. This makes articular cartilage repair process very difficult (Anderson, 1962). Articular cartilage is composed of specialized cells called chondrocytes with majority of percentage of the tissue formed by water (65-80%). The extracellular matrix of this connective tissue consists of collagen fibre which is a fibrous protein that provides for the structural network of the articular cartilage tissue. Collagen fibre which is mainly Type II collagen provides the tensile strength to the tissue.

1.8.1. Ultrastructure of articular cartilage:

Starting from the late 19^{th} century, work has been carried out to study the fibrous ultrastructure of the articular cartilage with the split-line technique put forward by HultKrantz in 1898 that gives a gross idea of the orientation of the collagen fibres in the top surface layer (Hultkrantz, 1898). However, there has been no proper consensus regarding split lines actually representing the preferred collagen fibre orientation. Based on this split line method and polarised light microscopy (PLM) studies, Benninghoff put forward the classic arcade model for the 3D structure of articular cartilage (Benninghoff, 1925) (Figure 1.6). Largely based on the morphological structure, collagen matrix and with varying density of chondrocyte cells in along the depth of the articular tissue, it can be broadly divided into

zonal structural layers depending on the orientation of the collagen fibre matrix: 1) Superficial zone, which accounts for roughly 10% of the total thickness of the tissue, with collagen fibres running parallel to the surface. 2) Transitional zone is the intermediate layer, which Benninghoff describes as containing collagen fibres that start from radial zone and then arcades down as it reaches the superficial zone interface. This arching gradually then falls back into radial zone. 3) Radial zone, where the collagen fibres run radially downwards into the calcified part of the tissue and 4) The interface between the radial zone and the calcified cartilage zone is called the tidemark (Figure 1.6).

Various other techniques have been reported in literature to study the the arrangement and orientation of the collagen fiber network in normal articular cartilage. These include scanning electron microscopy (SEM) (Clark, 1990; Jeffery *et al.*, 1991), differential interference contrast microscopy (Broom, 1984; Broom & Flachsmann, 2003) , small angle X-ray diffraction (Mollenhauer *et al.,* 2003; Muehleman *et al.,* 2004) as well as small angle X-ray scattering studies (Moger *et al.,* 2007), transmission electron microscopy (TEM), microscopic magnetic resonance imaging (μMRI), diffusion tensor MRI (dt-MRI), Fourier-transform infrared imaging (FTIR), X-ray diffraction, elastic scattering spectroscopy. However, these techniques excluding the MRI based imaging technique are based on measurement of the orientation along the 2D histological slice rather than the full 3D information of the collagen fibril.

It was using electron microscopy data that Jeffery *et al.* proposed the leaf-like lamellar model for the 3D fibrillar network of collagen fibre architecture in articular cartilage (Jeffery*, et al.*, 1991). This model unlike the arcade model possess a very organised arching of the collagen

fibres in the transitional zone with a definitive pattern to the arching of the collagen fibres from the radial zone towards the transitional zone (Figure 1.7).

Traditional method used to understand the orientation of the collagen architecture is PLM as used by Beninnghoff for putting forward the arcade model for articular cartilage ultrastructure. This method was the standard technique used before the advent of electron microscopy. However, over the years, PLM has been used to study the fibrillar network of collagen fibres in histological sectioned articular cartilage tissue (Kaab *et al.*, 1998), often used as a validation tool for other collagen ultrastrucutre imaging techniques (Bi *et al.*, 2005; de Visser *et al.*, 2008; Xia *et al.*, 2001), changes in the fibrillar network occuring during development (Rieppo *et al.*, 2009), etc. However, the main drawback with electron microscopy and PLM is that as the technique is 2D, the orientation information obtained could be misinterpreted based on the nature of sectioning of the slice carried out. The interpretation of the sections studied under PLM not cut along the split lines are reported to demonstrate different birefringence information (Changoor *et al.*, 2011). Recent studies have shown the dependence of T_2-weighted MRI imaging correlate with the normal articular cartilage ultrastructure (Nissi *et al.*, 2006; Xia*, et al.*, 2001; Zheng *et al.*, 2011). Dt-MRI measures the rate of diffusion of proton (water) molecules along the orderly fibrous biological tissues and the principal Eigen vector of the diffusion tensor so obtained is directly related to the long axis orientation of the collagen fibers (or any other fibrous macromolecule). Dt-MRI has been successfully reported to have been applied to find the orderly structure of fibrous tissues in brain , myocardium, normal human cartilage, intervertebral disc, etc (Deng *et al.,* 2007; Filidoro *et al.,* 2005; Meder *et al.,* 2006). However, the main drawback with this imaging technique is the trade off that has to be achieved between good spatial resolution and lower imaging time. To achieve higher resolution as

well accurate data interpretation from the background noise by improving signal to noise ratio requires either more averages or complex imaging pulse sequences which result in increased imaging times of the order of a few hours to a day or so for a sample. FTIR employs spectroscopy based imaging that identifies macromolecules based on their chemical compositions. The technique based on IR absorption band of vibrational energy involving the long peptide chain orientation in collagen fibril as well as the orientation of the amide I and amide II bonds in the collagen fibril (Bi*, et al.*, 2005; Xia, 2008; Xia *et al.*, 2007). The complications with FTIR are accurate analysis which needs accounting by accurate measurement of tissue thickness, polarisation artefact inherent in the system (Coats *et al.,* 2003), presence of other IR-active molecules like proteoglycans, etc (Bi, *et al.,* 2005).

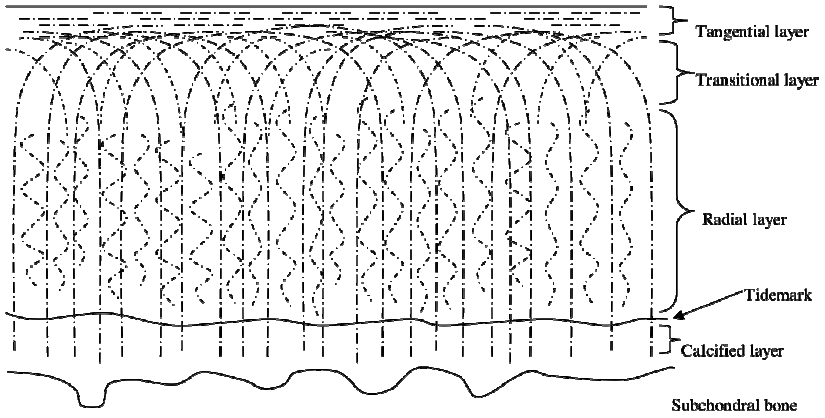

Figure 1.6: Zonal structure of the articular cartilage which gives the classic arcade structure of the collagen fibre orientation as put forward by Benninghoff based on PLM and split line studies. (Benninghoff, 1925)

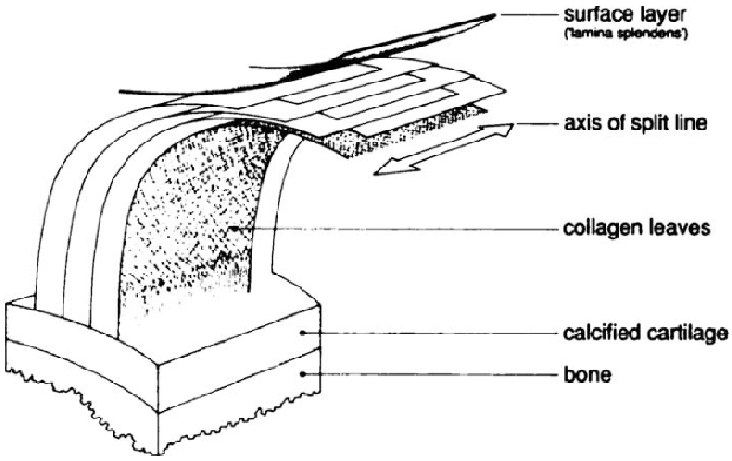

Figure 1.7: 3D lamellar sheet model of the articular cartilage (Jeffery, *et al.,* 1991)

Table 1.2: List of a few research works that studied the ultrastructure of articular cartilage

Author	Technique used	Tissue and animal studied	Comments
(Benninghoff, 1925)*	PLM, Split line technique	Human, dog, cat and rabbit articular cartilage	Proposed the classical arcade model of 4 distinct zonal layers in articular cartilage
(Mac, 1951)	PLM, phase contrast illumination	Ox and human	The structure proposed by them differed from that proposed by Benninghoff, that the collagen fibres are not radial but run oblique between articular cartilage and the subchondral bone. Also described an acellular bright surface layer called 'lamina splendens' which was disputed to be not seen by similar works carried out by other groups later.
(Weiss *et al.,* 1968)	Electron Microscope	Human	Reported a surface parallel orientation of collagen fibres but deeper that layer, the organisation is random orientation.
(Bullough & Goodfellow, 1968)	Electron Microscope, Split line technique	Human (various sites)	Supported general aspects of model put forward by Benninghoff

Table 1.2
contd….

(Clarke, 1971)	SEM	Human	Lower magnification supported Benninghoff model based structure, where as higher magnification revealed surface parallel collagen fibrils whereas elsewhere deeper a random orientation as reported by Weiss *et al.*
(Minns & Steven, 1977)	SEM	Human	Supported Benninghoff model with respect to the middle and radial zone orientation of collagen fibres
(Clark, 1985)	SEM	Rabbit	Supported general aspects of model put forward by Benninghoff
(Clark, 1991)	SEM	Human, dog and rabbit tibial plateau	Species comparison showed general pattern on collagen arrangement in these species. Also refers to the wrong interpretation of the random orientation of fibres in transitional zones to the wrong sectioning style
(Jeffery, *et al.,* 1991)*	SEM	Bovine metacarpal cartilage	Modified Benninghoff arcade model by proposing a leaf-like arrangement of the collagen fibres
(Kaab*, et al.*, 1998)	SEM	Tibial plateau of various mammalian species	Leaf-like arrangement in man, pig and dog More columnar arrangement in cow, sheep rabbit and rat

***** The main papers based on which work presented in later chapters is carried out.

The traditional method used in the diagnosis and treatment of articular cartilage degeneration include arthroscopy, radiography, MRI, high frequency ultrasound (Kim *et al.,* 1995; Sanghvi *et al.,* 1990), PLM as well as histology. Although arthroscopy is still prevalent tool in articular cartilage degeneration study, it is unable to detect the onset of articular cartilage degeneration without possible surface irregularities or abnormalities detected (Kijowski *et al.*, 2006). Also, there has been no definite tool to detect and evaluate articular cartilage degeneration or monitor the articular repair process. Radiography and MRI has been used as a non-invasive method trying to evaluate osteoarthritis based on the joint space narrowing. Normal MRI based technique have been used to diagnose cartilage degradation but only at

later stages owing to the low spatial resolution offered (Rubenstein *et al.*, 1997). There is a need for a non-invasive optical imaging tool providing required resolution over the 1-2mm thickness of the articular cartilage. It is to fill in this gap that this investigation is carried out to evaluate the possibility of use of PS-OCT to study the depth-dependent optical anisotropy information of articular cartilage. This study tries to establish PS-OCT as a non-invasive imaging tool to study the fibrillar network of collagen fibres in a normal articular cartilage tissue. Before proceeding to the main chapter reporting the main results of this investigation, a brief introduction to previous works related to OCT and articular cartilage is discussed in Section 1.8.2.

1.8.2. OCT and articular cartilage:

OCT being a non-invasive technique has been shown to be a potential tool for the study of onset, changes and diagnosis of osteoarthritis (O'Malley & Chu, 2011). Bear *et al.* have shown how OCT could be used to monitor the acute changes occuring during post traumatic osteoarthritis in tibial plateau explants from bovine knees (Bear *et al.,* 2010).

The greater potential of the non-invasive tool as presented by OCT lies in its ability to detect the early stages of changes occurring during the onset of osteoarthritis (Drexler *et al.,* 2001). Moreover, OCT has also been shown to be adaptable to arthroscopy to image the tissue in-vivo (Pan *et al.,* 2003). Drexler *et al.* showed the correlation between the polarization sensitivity as shown by polarized light microscopy of articular cartilage with the birefringence changes obtained using PS-OCT. Earlier research had pointed towards presence and absence of band patterns or birefringence as a diagnostic tool to distinguish between normal and osteoarthritic tissue using PS-OCT (Brezinski *et al.,* 1999; Drexler, *et al.,* 2001; Li *et al.,* 2005). However, studies carried out by later groups do not agree with the fact that

absence of birefringence bands implies diseased tissue. Ugryumova *et al.* have shown that the variations of birefringence patterns obtained depends on the angle of light beam that makes with the optic axis of the collagen fibre of the articular tissue (Ugryumova*, et al.*, 2005). This has been supported by PS-OCT results reported by Xie *et al.* (Xie *et al.,* 2006a, 2006b). Xie *et al.* has also proved that the optical phase retardance obtained from the articular cartilage is dependent only on the collagen network and not related to the proteoglycan content of the tissue which was quantified based on safranin-O staining studies (Xie, *et al.,* 2006a). Henceforth a detailed study underlying the relation between the incident direction of the light beam and the orientation along the depth of the articular cartilage has to be taken into account when interpreting the PS-OCT data and the birefringence information. Another factor to be considered is the heterogeneity of the orientation of the collagen fibre along the different sites of the articular cartilage sample (Clark, 1991; Xia *et al.,* 2002*)*. This has also been supported by PS-OCT studies (Matcher, 2009; Ugryumova, *et al.,* 2005; Xie *et al.,* 2008).

1.9. References:

Al-Qaisi, M. K., & Akkin, T. (2008). Polarization-sensitive optical coherence tomography based on polarization-maintaining fibers and frequency multiplexing. *Optics Express, 16*(17), 13032-13041.

Al-Qaisi, M. K., & Akkin, T. (2010). Swept-source polarization-sensitive optical coherence tomography based on polarization-maintaining fiber. *Optics Express, 18*(4), 3392-3403.

Anderson, C. E. (1962). The Structure and Function of Cartilage. *Journal of Bone and Joint Surgery-American Volume, 44*(4), 777-786.

Baumann, B., Gotzinger, E., Pircher, M., & Hitzenberger, C. K. (2007). Single camera based spectral domain polarization sensitive optical coherence tomography. *Optics Express, 15*(3), 1054-1063.

Baumgartner, A., Dichtl, S., Hitzenberger, C. K., Sattmann, H., Robl, B., Moritz, A. (2000). Polarization-sensitive optical coherence tomography of dental structures. *Caries Research, 34*(1), 59-69.

Bear, D. M., Szczodry, M., Kramer, S., Coyle, C. H., Smolinski, P., & Chu, C. R. (2010). Optical Coherence Tomography Detection of Subclinical Traumatic Cartilage Injury. *Journal of Orthopaedic Trauma, 24*(9), 577-582.

Benninghoff, A. (1925). Form und Bau der Gelenkknorpel in ihren Beziehungen zur Funktion. *Cell and Tissue Research, 2*(5), 783-862.

Bi, X., Li, G., Doty, S. B., & Camacho, N. P. (2005). A novel method for determination of collagen orientation in cartilage by Fourier transform infrared imaging spectroscopy (FT-IRIS). *Osteoarthritis and Cartilage, 13*(12), 1050-1058.

Brezinski, M. E., Herrmann, J. M., Pitris, C., Bouma, B. E., Boppart, S. A., Jesser, C. A. (1999). High resolution imaging of normal and osteoarthritic cartilage with optical coherence tomography. *Journal of Rheumatology, 26*(3), 627-635.

Broom, N. D. (1984). Further Insights into the Structural Principles Governing the Function of Articular-Cartilage. *Journal of Anatomy, 139*(Sep), 275-294.

Broom, N. D., & Flachsmann, R. (2003). Physical indicators of cartilage health: the relevance of compliance, thickness, swelling and fibrillar texture. *Journal of Anatomy, 202*(6), 481-494.

Bullough, P., & Goodfellow, J. (1968). The significance of the fine structure of articular cartilage. *Journal of Bone and Joint Surgery (British Volume), 50*(4), 852-857.

Cense, B., Gao, W., Brown, J. M., Jones, S. M., Jonnal, R. S., Mujat, M. (2009a). Retinal imaging with polarization-sensitive optical coherence tomography and adaptive optics. *Optics Express, 17*(24), 21634-21651.

Cense, B., Koperda, E., Brown, J. M., Kocaoglu, O. P., Gao, W., Jonnal, R. S. (2009b). Volumetric retinal imaging with ultrahigh-resolution spectral-domain optical coherence tomography and adaptive optics using two broadband light sources. *Optics Express, 17*(5), 4095-4111.

Cense, B., Mujat, M., Chen, T. C., Park, B. H., & de Boer, J. F. (2007). Polarization-sensitive spectral-domain optical coherence tomography using a single line scan camera. *Optics Express, 15*(5), 2421-2431.

Changoor, A., Tran-Khanh, N., Methot, S., Garon, M., Hurtig, M. B., Shive, M. S. (2011). A polarized light microscopy method for accurate and reliable grading of collagen organization in cartilage repair. *Osteoarthritis and Cartilage, 19*(1), 126-135.

Chen, T. C., Cense, B., Pierce, M. C., Nassif, N., Park, B. H., Yun, S. H. (2005). Spectral domain optical coherence tomography: ultra-high speed, ultra-high resolution ophthalmic imaging. *Archives of Ophthalmology, 123*(12), 1715-1720.

Chen, Z., Milner, T. E., Srinivas, S., Wang, X., Malekafzali, A., van Gemert, M. J. (1997). Noninvasive imaging of in vivo blood flow velocity using optical Doppler tomography. *Optics Letters, 22*(14), 1119-1121.

Choma, M. A., Sarunic, M. V., Yang, C. H., & Izatt, J. A. (2003). Sensitivity advantage of swept source and Fourier domain optical coherence tomography. *Optics Express, 11*(18), 2183-2189.

Clark, J. M. (1985). The organization of collagen in cryofractured rabbit articular cartilage: a scanning electron microscopic study. *Journal of Orthopaedic Research, 3*(1), 17-29.

Clark, J. M. (1990). The organisation of collagen fibrils in the superficial zones of articular cartilage. *Journal of Anatomy, 171*, 117-130.

Clark, J. M. (1991). Variation of Collagen Fiber Alignment in a Joint Surface - a Scanning Electron-Microscope Study of the Tibial Plateau in Dog, Rabbit, and Man. *Journal of Orthopaedic Research, 9*(2), 246-257.

Clarke, I. C. (1971). Articular cartilage: a review and scanning electron microscope study. 1. The interterritorial fibrillar architecture. *Journal of Bone and Joint Surgery (British Volume), 53*(4), 732-750.

Coats, A. M., Hukins, D. W., Imrie, C. T., & Aspden, R. M. (2003). Polarization artefacts of an FTIR microscope and the consequences for intensity measurements on anisotropic materials. *Journal of Microscopy, 211*(Pt 1), 63-66.

Davis, A. M., Choma, M. A., & Izatt, J. A. (2005). Heterodyne swept-source optical coherence tomography for complete complex conjugate ambiguity removal. *Journal of Biomedical Optics, 10*(6), 064005.

de Boer, J., Srinivas, S., Malekafzali, A., Chen, Z., & Nelson, J. (1998). Imaging thermally damaged tissue by Polarization Sensitive Optical Coherence Tomography. *Optics Express, 3*(6), 212-218.

de Boer, J. F., Cense, B., Park, B. H., Pierce, M. C., Tearney, G. J., & Bouma, B. E. (2003). Improved signal-to-noise ratio in spectral-domain compared with time-domain optical coherence tomography. *Optics Letters, 28*(21), 2067-2069.

de Boer, J. F., & Milner, T. E. (2002). Review of polarization sensitive optical coherence tomography and Stokes vector determination. *Journal of Biomedical Optics, 7*(3), 359-371.

de Boer, J. F., Milner, T. E., & Nelson, J. S. (1999). Determination of the depth-resolved Stokes parameters of light backscattered from turbid media by use of polarization-sensitive optical coherence tomography. *Optics Letters, 24*(5), 300-302.

de Boer, J. F., Milner, T. E., van Gemert, M. J. C., & Nelson, J. S. (1997). Two-dimensional birefringence imaging in biological tissue by polarization-sensitive optical coherence tomography. *Optics Letters, 22*(12), 934-936.

de Visser, S. K., Bowden, J. C., Wentrup-Byrne, E., Rintoul, L., Bostrom, T., Pope, J. M. (2008). Anisotropy of collagen fibre alignment in bovine cartilage: comparison of polarised light microscopy and spatially resolved diffusion-tensor measurements. *Osteoarthritis and Cartilage, 16*(6), 689-697.

Deng, X., Farley, M., Nieminen, M. T., Gray, M., & Burstein, D. (2007). Diffusion tensor imaging of native and degenerated human articular cartilage. *Magnetic Resonance Imaging, 25*(2), 168-171.

Drexler, W., Stamper, D., Jesser, C., Li, X. D., Pitris, C., Saunders, K. (2001). Correlation of collagen organization with polarization sensitive imaging of in vitro cartilage: Implications for osteoarthritis. *Journal of Rheumatology, 28*(6), 1311-1318.

Ducros, M. G., Marsack, J. D., Rylander, H. G., 3rd, Thomsen, S. L., & Milner, T. E. (2001). Primate retina imaging with polarization-sensitive optical coherence tomography. *Journal of the Optical Society of America A, 18*(12), 2945-2956.

Everett, M. J., Schoenenberger, K., Colston, B. W., & Da Silva, L. B. (1998). Birefringence characterization of biological tissue by use of optical coherence tomography. *Optics Letters, 23*(3), 228-230.

Fan, C., Wang, Y., & Wang, R. K. (2007). Spectral domain polarization sensitive optical coherence tomography achieved by single camera detection. *Optics Express, 15*(13), 7950-7961.

Fan, C., & Yao, G. (2010). Single camera spectral domain polarization-sensitive optical coherence tomography using offset B-scan modulation. *Optics Express, 18*(7), 7281-7287.

Fanjul-Velez, F., Pircher, M., Baumann, B., Gotzinger, E., Hitzenberger, C. K., & Arce-Diego, J. L. (2010). Polarimetric analysis of the human cornea measured by polarization-sensitive optical coherence tomography. *Journal of Biomedical Optics, 15*(5).

Fercher, A. F., Drexler, W., Hitzenberger, C. K., & Lasser, T. (2003). Optical coherence tomography - principles and applications. *Reports on Progress in Physics, 66*(2), 239-303.

Filidoro, L., Dietrich, O., Weber, J., Rauch, E., Oerther, T., Wick, M. (2005). High-resolution diffusion tensor imaging of human patellar cartilage: feasibility and preliminary findings. *Magnetic Resonance Medicine, 53*(5), 993-998.

Fried, D., Xie, J., Shafi, S., Featherstone, J. D., Breunig, T. M., & Le, C. (2002). Imaging caries lesions and lesion progression with polarization sensitive optical coherence tomography. *Journal of Biomedical Optics, 7*(4), 618-627.

Giattina, S. D., Courtney, B. K., Herz, P. R., Harman, M., Shortkroff, S., Stamper, D. L. (2006). Assessment of coronary plaque collagen with polarization sensitive optical coherence tomography (PS-OCT). *International Journal of Cardiology, 107*(3), 400-409.

Gotzinger, E., Baumann, B., Pircher, M., & Hitzenberger, C. K. (2009). Polarization maintaining fiber based ultra-high resolution spectral domain polarization sensitive optical coherence tomography. *Optics Express, 17*(25), 22704-22717.

Gotzinger, E., Pircher, M., Geitzenauer, W., Ahlers, C., Baumann, B., Michels, S. (2008). Retinal pigment epithelium segmentation by polarization sensitive optical coherence tomography. *Optics Express, 16*(21), 16410-16422.

Gotzinger, E., Pircher, M., & Hitzenberger, C. K. (2005). High speed spectral domain polarization sensitive optical coherence tomography of the human retina. *Optics Express, 13*(25), 10217-10229.

Gotzinger, E., Pircher, M., Sticker, M., Fercher, A. F., & Hitzenberger, C. K. (2004). Measurement and imaging of birefringent properties of the human cornea with phase-resolved, polarization-sensitive optical coherence tomography. *Journal of Biomedical Optics, 9*(1), 94-102.

Hee, M. R., Huang, D., Swanson, E. A., & Fujimoto, J. G. (1992). Polarization-Sensitive Low-Coherence Reflectometer for Birefringence Characterization and Ranging. *Journal of the Optical Society of America B-Optical Physics, 9*(6), 903-908.

Hitzenberger, C., Goetzinger, E., Sticker, M., Pircher, M., & Fercher, A. (2001). Measurement and imaging of birefringence and optic axis orientation by phase resolved polarization sensitive optical coherence tomography. *Optics Express, 9*(13), 780-790.

Hitzenberger, C. K., Gotzinger, E., & Pircher, M. (2006). Birefringence properties of the human cornea measured with polarization sensitive optical coherence tomography. *Bulletin of the Belgian Society of Ophtalmology*(302), 153-168.

Hofer, B., Povazay, B., Hermann, B., Unterhuber, A., Matz, G., & Drexler, W. (2009). Dispersion encoded full range frequency domain optical coherence tomography. *Optics Express, 17*(1), 7-24.

Hofer, B., Povazay, B., Unterhuber, A., Wang, L., Hermann, B., Rey, S. (2010). Fast dispersion encoded full range optical coherence tomography for retinal imaging at 800 nm and 1060 nm. *Optics Express, 18*(5), 4898-4919.

Huang, D., Swanson, E. A., Lin, C. P., Schuman, J. S., Stinson, W. G., Chang, W. (1991). Optical coherence tomography. *Science, 254*(5035), 1178-1181.

Hultkrantz, W. (1898). Über die Spaltrichtungen der Gelenkknorpel. *Verh. anat. Ges. (Jena), 12*, 248-256.

Izatt, J. A., Kulkarni, M. D., Yazdanfar, S., Barton, J. K., & Welch, A. J. (1997). In vivo bidirectional color Doppler flow imaging of picoliter blood volumes using optical coherence tomography. *Optics Letters, 22*(18), 1439-1441.

Jeffery, A. K., Blunn, G. W., Archer, C. W., & Bentley, G. (1991). Three-dimensional collagen architecture in bovine articular cartilage. *Journal of Bone and Joint Surgery Br, 73*(5), 795-801.

Jiao, S., Todorovic, M., Stoica, G., & Wang, L. V. (2005). Fiber-based polarization-sensitive Mueller matrix optical coherence tomography with continuous source polarization modulation. *Applied Optics, 44*(26), 5463-5467.

Jiao, S., & Wang, L. V. (2002a). Jones-matrix imaging of biological tissues with quadruple-channel optical coherence tomography. *Journal of Biomedical Optics, 7*(3), 350-358.

Jiao, S., & Wang, L. V. (2002b). Two-dimensional depth-resolved Mueller matrix of biological tissue measured with double-beam polarization-sensitive optical coherence tomography. *Optics Letters, 27*(2), 101-103.

Jiao, S., Yao, G., & Wang, L. V. (2000). Depth-resolved two-dimensional stokes vectors of backscattered light and mueller matrices of biological tissue measured with optical coherence tomography. *Applied Optics, 39*(34), 6318-6324.

Jiao, S., Yu, W., Stoica, G., & Wang, L. V. (2003a). Contrast mechanisms in polarization-sensitive Mueller-matrix optical coherence tomography and application in burn imaging. *Applied Optics, 42*(25), 5191-5197.

Jiao, S., Yu, W., Stoica, G., & Wang, L. V. (2003b). Optical-fiber-based Mueller optical coherence tomography. *Optics Letters, 28*(14), 1206-1208.

Jones, R. S., Darling, C. L., Featherstone, J. D., & Fried, D. (2006). Remineralization of in vitro dental caries assessed with polarization-sensitive optical coherence tomography. *Journal of Biomedical Optics, 11*(1), 014016.

Kaab, M. J., Gwynn, I. A., & Notzli, H. P. (1998). Collagen fibre arrangement in the tibial plateau articular cartilage of man and other mammalian species. *Journal of Anatomy, 193 (Pt 1)*, 23-34.

Kemp, N., Zaatari, H., Park, J., Rylander III, H. G., & Milner, T. (2005). Depth-resolved optic axis orientation in multiple layered anisotropic tissues measured with enhanced polarization-sensitive optical coherence tomography (EPS-OCT). *Optics Express, 13*(12), 4507-4518.

Kijowski, R., Blankenbaker, D., Stanton, P., Fine, J., & De Smet, A. (2006). Correlation between radiographic findings of osteoarthritis and arthroscopic findings of articular cartilage degeneration within the patellofemoral joint. *Skeletal Radiology, 35*(12), 895-902.

Kim, H. K. W., Babyn, P. S., Harasiewicz, K. A., Gahunia, H. K., Pritzker, F. P. H., & Foster, F. S. (1995). Imaging of immature articular cartilage using ultrasound backscatter microscopy at 50 MHz. *Journal of Orthopaedic Research, 13*(6), 963-970.

Kuo, W. C., Chou, N. K., Chou, C., Lai, C. M., Huang, H. J., Wang, S. S. (2007). Polarization-sensitive optical coherence tomography for imaging human atherosclerosis. *Applied Optics, 46*(13), 2520-2527.

Le Roy-Brehonnet, F., Le Jeune, B., Gerligand, P. Y., Cariou, J., & Lotrian, J. (1997). Analysis of depolarizing optical targets by Mueller matrix formalism. *Pure and Applied Optics, 6*(3), 385-404.

Leitgeb, R., Hitzenberger, C. K., & Fercher, A. F. (2003). Performance of fourier domain vs. time domain optical coherence tomography. *Optics Express, 11*(8), 889-894.

Leitgeb, R., Wojtkowski, M., Kowalczyk, A., Hitzenberger, C. K., Sticker, M., & Fercher, A. F. (2000). Spectral measurement of absorption by spectroscopic frequency-domain optical coherence tomography. *Optics Letters, 25*(11), 820-822.

Li, X. D., Martin, S., Pitris, C., Ghanta, R., Stamper, D. L., Harman, M. (2005). High-resolution optical coherence tomographic imaging of osteoarthritic cartilage during open knee surgery. *Arthritis Research and Therapy, 7*(2), R318-R323.

Liu, G., Zhang, J., Yu, L., Xie, T., & Chen, Z. (2009). Real-time polarization-sensitive optical coherence tomography data processing with parallel computing. *Applied Optics, 48*(32), 6365-6370.

Lu, S. Y., & Chipman, R. A. (1994). Homogeneous and Inhomogeneous Jones Matrices. *Journal of the Optical Society of America A, 11*(2), 766-773.

Lu, Z. H., Kasaragod, D. K., & Matcher, S. J. (2011). Optic axis determination by fibre-based polarization-sensitive swept-source optical coherence tomography. *Physics in Medicine and Biology, 56*(4), 1105-1122.

Mac, C. M. (1951). The movements of bones and joints; the mechanical structure of articulating cartilage. *Journal of Bone and Joint Surgery Br, 33B*(2), 251-257.

Matcher, S. J. (2009). A review of some recent developments in polarization-sensitive optical imaging techniques for the study of articular cartilage. *Journal of Applied Physics, 105*(10), 102041.

Meder, R., de Visser, S. K., Bowden, J. C., Bostrom, T., & Pope, J. M. (2006). Diffusion tensor imaging of articular cartilage as a measure of tissue microstructure. *Osteoarthritis Cartilage, 14*(9), 875-881.

Minns, R. J., & Steven, F. S. (1977). The collagen fibril organization in human articular cartilage. *Journal of Anatomy, 123*(Pt 2), 437-457.

Moger, C. J., Barrett, R., Bleuet, P., Bradley, D. A., Ellis, R. E., Green, E. M. (2007). Regional variations of collagen orientation in normal and diseased articular cartilage and subchondral bone determined using small angle X-ray scattering (SAXS). *Osteoarthritis Cartilage, 15*(6), 682-687.

Mollenhauer, J., Aurich, M., Muehleman, C., Khelashvilli, G., & Irving, T. C. (2003). X-ray diffraction of the molecular substructure of human articular cartilage. *Connective Tissue Research, 44*(5), 201-207.

Moneron, G., Boccara, A. C., & Dubois, A. (2007). Polarization-sensitive full-field optical coherence tomography. *Optics Letters, 32*(14), 2058-2060.

Muehleman, C., Majumdar, S., Issever, A. S., Arfelli, F., Menk, R. H., Rigon, L. (2004). X-ray detection of structural orientation in human articular cartilage. *Osteoarthritis and Cartilage, 12*(2), 97-105.

Nadkarni, S. K., Bouma, B. E., de Boer, J., & Tearney, G. J. (2009). Evaluation of collagen in atherosclerotic plaques: the use of two coherent laser-based imaging methods. *Lasers Med Sci, 24*(3), 439-445.

Nissi, M. J., Rieppo, J., Toyras, J., Laasanen, M. S., Kiviranta, I., Jurvelin, J. S. (2006). T(2) relaxation time mapping reveals age- and species-related diversity of collagen network architecture in articular cartilage. *Osteoarthritis and Cartilage, 14*(12), 1265-1271.

O'Malley, M. J., & Chu, C. R. (2011). Arthroscopic optical coherence tomography in diagnosis of early arthritis. [Review Article]. *Minimally Invasive Surgery, Hindawi Publishing Co., 2011*, 671308.

Oh, W. Y., Yun, S. H., Vakoc, B. J., Shishkov, M., Desjardins, A. E., Park, B. H. (2008). High-speed polarization sensitive optical frequency domain imaging with frequency multiplexing. *Optics Express, 16*(2), 1096-1103.

Pan, Y. T., Li, Z. G., Xie, T. Q., & Chu, C. R. (2003). Hand-held arthroscopic optical coherence tomography for in vivo high-resolution imaging of articular cartilage. *Journal of Biomedical Optics, 8*(4), 648-654.

Park, B., Pierce, M. C., Cense, B., Yun, S. H., Mujat, M., Tearney, G. (2005a). Real-time fiber-based multi-functional spectral-domain optical coherence tomography at 1.3 microns. *Optics Express, 13*(11), 3931-3944.

Park, B. H., Pierce, M. C., Cense, B., & de Boer, J. F. (2004). Jones matrix analysis for a polarization-sensitive optical coherence tomography system using fiber-optic components. *Optics Letters, 29*(21), 2512-2514.

Park, B. H., Pierce, M. C., Cense, B., & de Boer, J. F. (2005b). Optic axis determination accuracy for fiber-based polarization-sensitive optical coherence tomography. *Optics Letters, 30*(19), 2587-2589.

Park, B. H., Saxer, C., Srinivas, S. M., Nelson, J. S., & de Boer, J. F. (2001). In vivo burn depth determination by high-speed fiber-based polarization sensitive optical coherence tomography. *Journal of Biomedical Optics, 6*(4), 474-479.

Park, J., Kemp, N. J., Zaatari, H. N., Rylander, H. G., & Milner, T. E. (2006). Differential geometry of normalized Stokes vector trajectories in anisotropic media. *Journal of the Optical Society of America A, 23*(3), 679-690.

Pasquesi, J. J., Schlachter, S. C., Boppart, M. D., Chaney, E., Kaufman, S. J., & Boppart, S. A. (2006). In vivo detection of exercised-induced ultrastructural changes in genetically-altered murine skeletal muscle using polarization-sensitive optical coherence tomography. *Optics Express, 14*(4), 1547-1556.

Pierce, M., Shishkov, M., Park, B., Nassif, N., Bouma, B., Tearney, G. (2005). Effects of sample arm motion in endoscopic polarization-sensitive optical coherence tomography. *Optics Express, 13*(15), 5739-5749.

Pircher, M., Goetzinger, E., Leitgeb, R., & Hitzenberger, C. K. (2004a). Three dimensional polarization sensitive OCT of human skin in vivo. *Optics Express, 12*(14), 3236-3244.

Pircher, M., Goetzinger, E., Leitgeb, R., & Hitzenberger, C. K. (2004b). Transversal phase resolved polarization sensitive optical coherence tomography. *Physics in Medicine and Biology, 49*(7), 1257-1263.

Pircher, M., Gotzinger, E., Findl, O., Michels, S., Geitzenauer, W., Leydolt, C. (2006). Human macula investigated in vivo with polarization-sensitive optical coherence tomography. *Invest Ophthalmol Vis Sci, 47*(12), 5487-5494.

Pircher, M., Gotzinger, E., Leitgeb, R., Sattmann, H., Findl, O., & Hitzenberger, C. K. (2004c). Imaging of polarization properties of human retina in vivo with phase resolved transversal PS-OCT. *Optics Express, 12*(24), 5940-5951.

Richartz, M., & Hsu, H. Y. (1949). Analysis of Elliptical Polarization. *Journal of the Optical Society of America, 39*(2), 136-157.

Rieppo, J., Hyttinen, M. M., Halmesmaki, E., Ruotsalainen, H., Vasara, A., Kiviranta, I. (2009). Changes in spatial collagen content and collagen network architecture in porcine articular cartilage during growth and maturation. *Osteoarthritis Cartilage, 17*(4), 448-455.

Roth, J. E., Kozak, J. A., Yazdanfar, S., Rollins, A. M., & Izatt, J. A. (2001). Simplified method for polarization-sensitive optical coherence tomography. *Optics Letters, 26*(14), 1069-1071.

Rubenstein, J. D., Li, J. G., Majumdar, S., & Henkelman, R. M. (1997). Image resolution and signal-to-noise ratio requirements for MR imaging of degenerative cartilage. *American Journal of Roentgenology, 169*(4), 1089-1096.

Sanghvi, N. T., Snoddy, A. M., Myers, S. L., Brandt, K. D., Reilly, C. R., & Franklin, T. D. (1990). Characterization of Normal and Osteoarthritic Cartilage Using 25 Mhz Ultrasound. *IEEE 1990 Ultrasonics Symposium : Proceedings, Vols 1-3*, 1413-1416.

Sarunic, M., Choma, M. A., Yang, C., & Izatt, J. A. (2005). Instantaneous complex conjugate resolved spectral domain and swept-source OCT using 3x3 fiber couplers. *Optics Express, 13*(3), 957-967.

Saxer, C. E., de Boer, J. F., Park, B. H., Zhao, Y., Chen, Z., & Nelson, J. S. (2000). High-speed fiber-based polarization-sensitive optical coherence tomography of in vivo human skin. *Optics Letters, 25*(18), 1355.

Schmitt, J. M., Xiang, S. H., & Yung, K. M. (1998). Differential absorption imaging with optical coherence tomography. *Journal of the Optical Society of America A, 15*(9), 2288-2296.

Schmoll, T., Gotzinger, E., Pircher, M., Hitzenberger, C. K., & Leitgeb, R. A. (2010). Single-camera polarization-sensitive spectral-domain OCT by spatial frequency encoding. *Optics Letters, 35*(2), 241-243.

Schoenenberger, K., Colston, B. W., Maitland, D. J., Da Silva, L. B., & Everett, M. J. (1998). Mapping of birefringence and thermal damage in tissue by use of polarization-sensitive optical coherence tomography. *Applied Optics, 37*(25), 6026-6036.

Srinivas, S. M., de Boer, J. F., Park, H., Keikhanzadeh, K., Huang, H. E. L., Zhang, J. (2004). Determination of burn depth by polarization-sensitive optical coherence tomography. *Journal of Biomedical Optics, 9*(1), 207-212.

Todorovic, M., Jiao, S., Ai, J., Pereda-Cubian, D., Stoica, G., & Wang, L. V. (2008). In vivo burn imaging using Mueller optical coherence tomography. *Optics Express, 16*(14), 10279-10284.

Todorovic, M., Jiao, S., Wang, L. V., & Stoica, G. (2004). Determination of local polarization properties of biological samples in the presence of diattenuation by use of Mueller optical coherence tomography. *Optics Letters, 29*(20), 2402-2404.

Ugryumova, N., Attenburrow, D. P., Winlove, C. P., & Matcher, S. J. (2005). The collagen structure of equine articular cartilage, characterized using polarization-sensitive

optical coherence tomography. *Journal of Physics D-Applied Physics, 38*(15), 2612-2619.

Unterhuber, A., Povazay, B., Bizheva, K., Hermann, B., Sattmann, H., Stingl, A. (2004). Advances in broad bandwidth light sources for ultrahigh resolution optical coherence tomography. *Physics in Medicine and Biology, 49*(7), 1235-1246.

Wang, H., Al-Qaisi, M. K., & Akkin, T. (2010). Polarization-maintaining fiber based polarization-sensitive optical coherence tomography in spectral domain. *Optics Letters, 35*(2), 154-156.

Weiss, C., Rosenberg, L., & Helfet, A. J. (1968). An ultrastructural study of normal young adult human articular cartilage. *Journal of Bone & Joint Surgery Am, 50*(4), 663-674.

Whitney, C. (1971). Pauli-Algebraic Operators in Polarization Optics. *Journal of the Optical Society of America, 61*(9), 1207-&.

Wojtkowski, M., Kowalczyk, A., Leitgeb, R., & Fercher, A. F. (2002). Full range complex spectral optical coherence tomography technique in eye imaging. *Optics Letters, 27*(16), 1415-1417.

Xia, Y. (2008). Averaged and depth-dependent anisotropy of articular cartilage by microscopic imaging. *Semin Arthritis Rheum, 37*(5), 317-327.

Xia, Y., Moody, J. B., Alhadlaq, H., Burton-Wurster, N., & Lust, G. (2002). Characteristics of topographical heterogeneity of articular cartilage over the joint surface of a humeral head. *Osteoarthritis and Cartilage, 10*(5), 370-380.

Xia, Y., Moody, J. B., Burton-Wurster, N., & Lust, G. (2001). Quantitative in situ correlation between microscopic MRI and polarized light microscopy studies of articular cartilage. *Osteoarthritis Cartilage, 9*(5), 393-406.

Xia, Y., Ramakrishnan, N., & Bidthanapally, A. (2007). The depth-dependent anisotropy of articular cartilage by Fourier-transform infrared imaging (FTIRI). *Osteoarthritis Cartilage, 15*(7), 780-788.

Xie, T., Guo, S., Zhang, J., Chen, Z., & Peavy, G. M. (2006a). Determination of characteristics of degenerative joint disease using optical coherence tomography and polarization sensitive optical coherence tomography. *Lasers in Surgery and Medicine, 38*(9), 852-865.

Xie, T., Guo, S., Zhang, J., Chen, Z., & Peavy, G. M. (2006b). Use of polarization-sensitive optical coherence tomography to determine the directional polarization sensitivity of articular cartilage and meniscus. *Journal of Biomedical Optics, 11*(6), 064001-064008.

Xie, T., Xia, Y., Guo, S., Hoover, P., Chen, Z., & Peavy, G. M. (2008). Topographical variations in the polarization sensitivity of articular cartilage as determined by polarization-sensitive optical coherence tomography and polarized light microscopy. *Journal of Biomedical Optics, 13*(5), 054034.

Yamanari, M., Makita, S., Lim, Y., & Yasuno, Y. (2010). Full-range polarization-sensitive swept-source optical coherence tomography by simultaneous transversal and spectral modulation. *Optics Express, 18*(13), 13964-13980.

Yamanari, M., Makita, S., Madjarova, V. D., Yatagai, T., & Yasuno, Y. (2006). Fiber-based polarization-sensitive Fourier domain optical coherence tomography using B-scan-oriented polarization modulation method. *Optics Express, 14*(14), 6502-6515.

Yamanari, M., Makita, S., & Yasuno, Y. (2008). Polarization-sensitive swept-source optical coherence tomography with continuous source polarization modulation. *Optics Express, 16*(8), 5892-5906.

Yao, G., & Wang, L. V. (1999). Two-dimensional depth-resolved Mueller matrix characterization of biological tissue by optical coherence tomography. *Optics Letters, 24*(8), 537-539.

Yasuno, Y., Makita, S., Endo, T., Aoki, G., Itoh, M., & Yatagai, T. (2006). Simultaneous B-M-mode scanning method for real-time full-range Fourier domain optical coherence tomography. *Applied Optics, 45*(8), 1861-1865.

Yasuno, Y., Makita, S., Sutoh, Y., Itoh, M., & Yatagai, T. (2002). Birefringence imaging of human skin by polarization-sensitive spectral interferometric optical coherence tomography. *Optics Letters, 27*(20), 1803-1805.

Zhang, J., Guo, S., Jung, W., Nelson, J., & Chen, Z. (2003). Determination of birefringence and absolute optic axis orientation using polarization-sensitive optical coherence tomography with PM fibers. *Optics Express, 11*(24), 3262-3270.

Zhang, J., Jung, W., Nelson, J., & Chen, Z. (2004). Full range polarization-sensitive Fourier domain optical coherence tomography. *Optics Express, 12*(24), 6033-6039.

Zhao, M., & Izatt, J. A. (2009). Single-camera sequential-scan-based polarization-sensitive SDOCT for retinal imaging. *Optics Letters, 34*(2), 205-207.

Zheng, S., Xia, Y., & Badar, F. (2011). Further studies on the anisotropic distribution of collagen in articular cartilage by muMRI. *Magnetic Resonance Medicine, 65*(3), 656-663.

CHAPTER 2

PS-OCT of Articular Cartilage

2.1: Summary

This chapter discusses the main results obtained from the PS-OCT imaging over multiple angles of incidence from single layered anisotropic birefringent tissue (tendon) to multi-layered anisotropic articular cartilage sample. Two different schemes of PS-OCT systems are used for the study: One belonging to the first generation TD-PS-OCT system and the other state of the art Fourier version of PS-OCT involving continuous modulation of the polarization states of the incident light beam onto the sample. Extended Jones matrix calculus (EJMC) is used to analyze the PS-OCT data over oblique incidence angle and to interpret the retardance data obtained and also to successfully obtain the optic axis information in 3D over the depth of the tissue. The major objective of the study is to obtain a theoretical framework to interpret the PS-OCT data in order to extract the 3D structural orientation information from the layered birefringent tissue of articular cartilage.

The chapter is organized in the following order in subsequent sections in this chapter. Starting with a brief introduction of the problem investigated (Section 2.2), the theory behind PS-OCT data analysis of the two different PS-OCT systems used is given (Sections 2.3 & 2.4). Then, the extraction of optic axis information is discussed for the two systems (Sections 2.5 & 2.6) before proceeding onto a detailed description of theoretical details of angle-resolved PS-OCT measurements (Section 2.7) as well as EJMC and its implementation to extract the optic axis information of the complex 3D architecture of articular cartilage (Section 2.8). A noise model is chosen to be applied onto the simulation results, to better match experimentally obtained TD-PS-OCT data (Section 2.9). With the inclusion of a noise

model in the EJMC simulated retardance profiles, a manual fit based on visual comparison of profiles of the EJMC data and TD-PS-OCT data is carried out as an initial guiding point towards development of an optimized algorithm to extract the 3D optic axis information from the layered articular cartilage structure. Presented in that section are the fitting details of EJMC data to experimental data of single layered tendon structure and multi layered articular cartilage structure (Section 2.10). The idea of optimisation is discussed in detail in section based on two different choices of nonlinear optimisation algorithms-'fminsearch' and 'fmincon' (Section 2.11). A section discussing the analysis of CPM-SS-PS-OCT data and the noise model to be implemented along with a discussion of data sets obtained for articular cartilage using two different speeds of data acquisition cards and their implication in image processing of optic axis information extraction for an articular cartilage sample is discussed (Section 2.12). Conclusions and further scope of study is detailed thereupon (Sections 2.13 & 2.14).

2.2: Introduction

Collagen fibres form the main constituent of the fibrous tissues in extracellular matrix of connective tissues in animal body. Type I collagen fibres in tendon, ligaments, etc and type II collagen fibres in articular cartilage are the commonly found types of collagen fibres (Mow & Ratcliffe, 1997). Our main purpose behind this study is to extract information about the collagen fibre network in articular cartilage which forms the basis of the framework of the structure. Also, in certain diagnostic conditions like osteoarthritis are known to be onset with the disruption of this delicate network of collagen fibres (Clark & Simonian, 1997; Yamamoto *et al.*, 2005). Thus, developing a non-invasive technique to obtain collagen fibre orientation information in articular cartilage is a step closer to understanding the intricate relation between the onset of osteoarthritis and collagen fibre framework in articular cartilage. In order to carry out this work, the theoretical aspects from crystal optics involving light interaction in anisotropic media is introduced with respect to the biological tissues in which the collagen fibres are modelled as positive uniaxial crystals with different refractive indices along and across the length of the fibre. Low coherence interferometric based imaging technique called optical coherence tomography (OCT) provides the non-invasive technique to obtain backscattered light, that gives structural information analogous to that obtained from ultrasound technique. Anisotropic information of the light interaction in a birefringent biological sample could be obtained using polarised version of OCT as discussed in Chapter 1. This chapter presents in detail the polarimetric based study of anisotropic articular cartilage structure using two different schemes of PS-OCT and the extraction of 3D optic axis information of the collagen network using mathematical tools to study interaction of biological tissue to polarised light.

2.3: TD-PS-OCT:

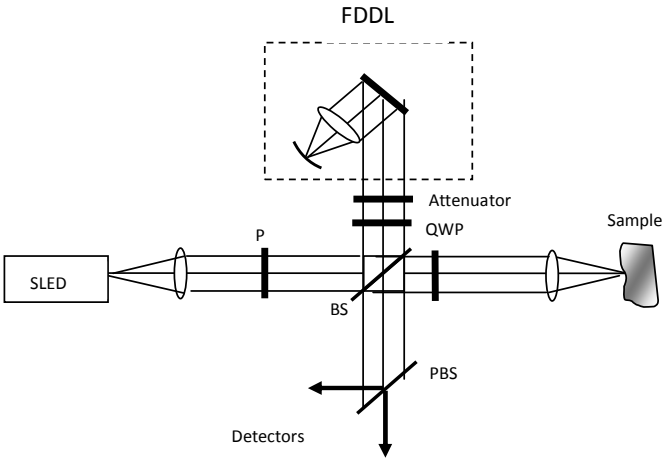

Figure.2.1: Schematic of the time domain PS-OCT system used to study depth dependent optic axis orientation information of articular cartilage; P-linear polariser, QWP-quarter wave plate, BS-beam splitter, PBS-polarising beam splitter, SLED-superluminescent diode, FDDL-Fourier domain optical delay line.

The PS-OCT system used for angle resolved-EJMC study is a bulk-optics based TD-PS-OCT system which belongs to the first generation of PS-OCT systems. The main disadvantage with a time-domain based set up is the slow mechanical optical delay line which increases the acquisition time required to obtain an image. The light source used is a custom built quantum dot super luminescent diode which has a central wavelength of 1300nm with a bandwidth of 85nm (Greenwood *et al.*, 2010). The light is input as horizontally polarized into the PS-OCT system by means of a linear polarizer. This linearly polarized light beam is then split using a non-polarising beam splitter into two arms of the interferometer (Figure 2.1). The light beam exiting from the reference arm has equal amplitude and phase along the vertical and horizontal component of the electric field component. This is achieved on double pass of light beam entering and exiting the QWP oriented at 22.5^{o} with respect to the horizontal.

$$E_{reference}(z) = \begin{pmatrix} \cos\pi/8 & -\sin\pi/8 \\ \sin\pi/8 & \cos\pi/8 \end{pmatrix} \begin{pmatrix} e^{i\pi/4} & 0 \\ 0 & e^{-i\pi/4} \end{pmatrix}^2 \begin{pmatrix} \cos\pi/8 & \sin\pi/8 \\ -\sin\pi/8 & \cos\pi/8 \end{pmatrix} \frac{E(z)}{\sqrt{2}} \begin{pmatrix} 0 \\ 1 \end{pmatrix} \quad (2.1)$$

$$E_{reference}(z) \propto \begin{pmatrix} 1 \\ 1 \end{pmatrix} \quad (2.2)$$

The light from the reference arm then passes through the delay line which gives the A-scans of OCT image. The optical power in the reference arm is attenuated upon return of the light beam through the delay line in order to optimise the dynamic range in shot noise limited detection scheme implemented in OCT (Tomlins & Wang, 2005).

In the sample arm, the QWP is oriented at 45^o to the horizontal. Thus linearly polarized light is converted to circularly polarized light. Thus circularly polarized light beam is incident onto the sample. The Fourier domain delay line allows for the depth scan in an A-scan with a scanning speed of 100Hz (Tearney *et al.*, 1997). This means that we could obtain an OCT image of 400 A-scans in 4s. Unbalanced detection scheme is used with this system (Podoleanu, 2000). Although this system is not state of art with respect to the speed of imaging, it serves our purpose of study to obtain a theoretical framework to analyse the PS-OCT data for articular cartilage. Moreover, from previous studies carried out in our group, the resolution, both axial and lateral and dynamic range of the system were found to be within the optimal range with respect to OCT systems available in the market (Jacobs, 2011) and valid for the type of study reported here. The polarization properties of the medium under study are analysed using Jones matrix and EJMC is being used to deal with off-axis multi-angle PS-OCT measurements for layered anisotropic sample such as articular cartilage. Depth dependent retardance is given by:

$$\delta(z) = \arctan\left(\sqrt{\frac{I_V(z)}{I_H(z)}}\right) \tag{2.3}$$

Or equivalently as

$$\delta(z) = \arctan\left(\frac{A_V(z)}{A_H(z)}\right) \tag{2.4}$$

where, $I_V(z)$ and $I_H(z)$ are the light intensities reflected from the sample and detected along the two orthogonally polarized detector channels. Also, Stokes parameters can be obtained from the demodulated amplitudes $A_V(z)$ and $A_H(z)$ as well as the phase obtained from these data obtained. To obtain the amplitude and phase from the recorded intensities in the two orthogonal detectors, Hilbert transform is used. This provides us the analytical signal given by:

$$\tilde{A}_{H,V} = I_{H,V} + i \times Hi(I_{H,V}) \tag{2.5}$$

$$= A_{H,V} \exp(i\Phi_{H,V}) \tag{2.6}$$

The algorithm used to obtain the depth dependent retardance values from this PS-OCT system takes into account only the modulus values of the demodulated amplitude, thereby restricting the obtained retardance profiles to the range $[0 \quad \pi/2]$.

2.4: CPM-SS-PS-OCT

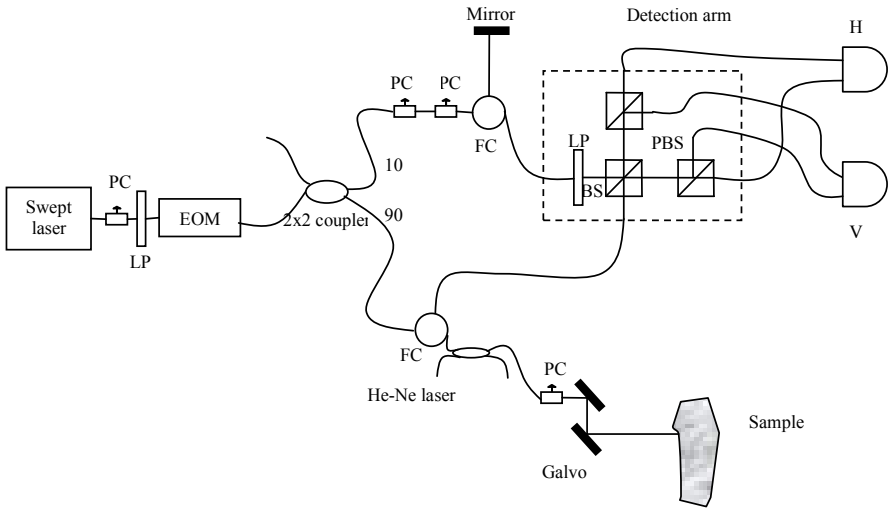

Figure 2.2: Schematic of the continuous polarisation modulation based swept source PS-OCT system used to study depth dependent optic axis orientation information of articular cartilage; PC-polarisation controller, FC – fibre optic circulator, LP-linear polariser, BS-beam splitter, PBS-polarising beam splitter, H&V- two orthogonally polarised detection channels.

The TD-PS-OCT system that has been described in the earlier section has the disadvantage of lower imaging speed and also the bulk optics based implementation in its design serious limiting its application to study *in-vivo* samples and for clinical applications. To overcome this, a swept source based PS-OCT system is implemented. The implementation follows the scheme developed by Yamanari *et al.* which is based on continuous polarization modulation of the incident light beam onto the sample (Yamanari *et al.*, 2008). This novel scheme of continuous polarisation modulation implementation was PS-OCT was first implemented by Jiao *et al.* in their time domain version of the set up in which the incident polarisation was modulated along an A-scan (Jiao *et al.*, 2005) based on technique developed in ellipsometry (Jasperson & Schnatterly, 1969). This scheme was later adopted by Yamanari *et al.* for a swept laser source (Yamanari*, et al.*, 2008). More details on the implementation scheme of

this PS-OCT are given in two of the journal papers from our group (Lu *et al.*, 2011a, 2011b). The schematic is shown in detail in Figure 2.2, which is adapted from Lu *et al.* and is described here. The light source used is HSL-2000-10-MDL from Santec, Japan centred at wavelength 1315nm, with a broadband spectrum over 157nm and full width half maximum of 128nm. The average output power is 10mW with a peak output of around 23mW with a wavelength sweep rate of 10kHz. The light source thus yields an axial resolution of 10microns in air. A linear polariser is introduced between the source and the polarisation modulator.

Although, the PS-OCT scheme is single mode fibre based, the detection involves a bulk-optics based implementation which allows for more sensitivity and reduced artefact in understanding the birefringence data obtained from the system. However, this does not restrict its usability in terms of applicability in clinical imaging or *in-vivo* imaging, as at the sample end, the light collection scheme is still based on fibre optics components. Also, the continuous modulation is carried on the linear polarized light exiting the swept laser source by using a broadband waveguide modulator as implemented by Yamanari *et al.* in later reported implementation based on SS-PS-OCT (Yamanari *et al.*, 2009). The main advantage this non-resonant modulator allows over a resonant modulator is the lower driving voltages. The EOM (electro optic modulator) in this PS-SS-OCT is PC-B3-00-SFAP-SFA-130 (EOspace) operating at 6.7MHz. This broadband modulator can be easily driven synchronously to remove the jitter between the swept source sweep and analog-to-digital converter (ADC) sampling clock during data acquisition (Lu*, et al.*, 2011a)), which is discussed in later half of this section. EOM is driven by an arbitrary function generator 33120A, Agilent Japan and BTM00250 Tomco Technologies RF amplifier module with a fixed optic axis orientation of 45^{o}. The driving signal is a sinusoidal signal with a frequency

one-third of the sampling rate of the digitizer in the data acquisition part, which is 6.67MHz. The amplitude of the driving signal is 2.405 radians; the reason behind this choice is discussed further on in this section. However, polarisation modulation scheme independent of the calibration of the driving amplitude of the driving sinusoidal wave is also been shown to be implemented in this scheme of CPM-PS-SS-OCT by Lu *et al.* in a recent publication (Lu *et al.*, 2012). Two single mode fibre based circulators, one in sample arm and one in reference arm are introduced to reduce the mismatch of optical dispersion in the arms of the interferometer. A 9:1 fibre coupler divides the power into sample and reference arm. A linear polariser at -45^{o} is used before the detection segment after light reflected from mirror in the reference arm to obtain equal powers in the two orthogonally polarised detection channels. Constant optical power in the reference arm along the modulation cycle of EOM is maintained by introduction of two polarisation controller in the reference arm as shown in the Figure 3.2. The sample arm has a 6215, Cambridge Technology, US two-axis galvanometer scanner with an OCT scanning lens LSM03 from Thorlabs which has a spot size of 25um in the focal plane (f =36mm). A He-Ne laser operating at 635nm is incorporated along the sample arm using a SMF coupler to visually locate the site of imaging in the sample mounted. The signal detection arm of PS-OCT consists of two balanced photoreceivers (1817-FC, New Focus, US) for the horizontally and vertically polarised optical channels obtained by using a beam splitter in the detection arm followed by two polarisation based beam splitters. A 14-bit digitizer (M2i.4022, Spectrum GmbH, Germany) at a speed of 20MS/s is used for data acquisition whilst the detected signals are low pass filtered using SXLP-8, Mini-Circuits, US from dc to 8MHz and amplified over a magnitudes ten times the original using amplifier ZFL-500, Mini-Circuits, US.

The use of polarisation modulator in PS-OCT system is implemented to provide for different (at least two) polarisation states incident onto the sample that allows the full Jones matrix calculation of the sample under study. EOM driven by step waveforms have also been reported that allows for birefringence measurements by analysis over successive A-scans (Pierce *et al.*, 2002). The sinusoidal modulation of EOM allows for the calculation of Jones matrix of the sample using a single A-scan measurement by the analysis of the non-modulated and modulated signals in the continuous polarisation modulation scheme. Sinusoidal modulation of EOM based PS-OCT system presents one more disadvantage compared to the conventional OCT system. As both zeroth and first order signals are required to calculate the Jones matrix of the sample, it potentially reduces the depth range in the Fourier transformed signal to one third the actual depth available to a conventional SS-OCT system. In this scheme of our implementation of CPM-SS-PS-OCT, a maximum depth of around 1100 microns is achieved in air, which in articular cartilage tissue is around 700 microns. This presents itself as a major obstacle in understanding the depth-dependent anisotropic information from articular cartilage, which is discussed in detail in Section 2.12. Depth penetration achieved with CPM-SS-PS-OCT has been extended by increasing the sampling frequency using an 8-bit digitiser card of higher sampling rate of 100MS/s (M2i.2031, Spectrum GmbH, Germany) and the polarisation modulation frequency. More on the PS-OCT images obtained for articular cartilage using CPM-SS-PS-OCT implementation with two different rates of data acquisition, 20MS/s and 100MS/s are given in Section 2.12.

Jones matrix formalism is implemented to obtain the birefringence information of the sample studied using this system. The phase modulation of the EOM is given by:

$$\Phi = A_0 \sin(\omega_m t) \tag{2.7}$$

Here A_0 is taken to be 2.405 radians, which is the amplitude of the sinusoidal driving wave of the modulator. The reason for this choice of value for A_0 is being discussed later in this section. The frequency ω_m of the EOM modulator is 6.67MHz, which is one-third of the frequency of the data acquisition card.

The Jones matrix of the polarization modulator with a fixed optic axis orientation of 45^o is given by

$$\begin{bmatrix} \cos\frac{\Phi}{2} & i\sin\frac{\Phi}{2} \\ i\sin\frac{\Phi}{2} & \cos\frac{\Phi}{2} \end{bmatrix} \tag{2.8}$$

Hence, the vertically polarized incident light beam incident onto the polarization modulation is transformed as:

$$\begin{bmatrix} E_H \\ E_V \end{bmatrix} = \begin{bmatrix} \cos\frac{\Phi}{2} & i\sin\frac{\Phi}{2} \\ i\sin\frac{\Phi}{2} & \cos\frac{\Phi}{2} \end{bmatrix} \begin{bmatrix} 1 \\ 0 \end{bmatrix} = \begin{bmatrix} \cos\frac{\Phi}{2} \\ i\sin\frac{\Phi}{2} \end{bmatrix} \tag{2.9}$$

Since the system is a fibre based system, the overall Jones matrix of the sample that also includes the birefringence information of the sample is given by

$$J_{measured} = J_{out} J_{sample} J_{in} = \begin{bmatrix} J_{11} & J_{12} \\ J_{21} & J_{22} \end{bmatrix} \tag{2.10}$$

where, J_{in} is the Jones matrix that characterizes the system from the modulator to the sample surface, J_{sample} gives the depth dependent double pass Jones matrix of the sample studied

which gives the birefringence information and J_{out} is the Jones matrix from the sample surface to the beam splitter at the detector end.

The Jones vector output from the sample arm is therefore given by

$$E_{sample} = J_{measured}\begin{bmatrix} E_H \\ E_V \end{bmatrix} = \begin{bmatrix} J_{11} & J_{12} \\ J_{21} & J_{22} \end{bmatrix}\begin{bmatrix} \cos\Phi/2 \\ i\sin\Phi/2 \end{bmatrix} = \begin{bmatrix} J_{12}\cos\Phi/2 + iJ_{11}\sin\Phi/2 \\ J_{22}\cos\Phi/2 + iJ_{21}\sin\Phi/2 \end{bmatrix} \tag{2.11}$$

The Jones vector output of the reference arm is then given by:

$$E_{ref} = \begin{bmatrix} E_{Href} \\ E_{Vref} \end{bmatrix} e^{i\Phi/2} \tag{2.12}$$

The detected intensities could be then given by:

$$I_{h,v} = I_{ho,vo} + \tilde{I}_{h,v} \tag{2.13}$$

$$I_h(t) = \left|E_{ref}\right|^2 + \left|E_{sam}\right|^2 + E_{ref}E_{sam}^* + E_{ref}^*E_{sam} \tag{2.14}$$

With the interferometric part as the

$$\tilde{I}_h(\omega) = \Im\left[E_{ref}E_{sam}^*\right] = \frac{E_r}{2}\left\{\Im\left[J_{12}^* - J_{11}^*\right] + \Im\left[J_{12}^* - J_{11}^*\right] + \Im\left[e^{-i\Phi}\right]\right\} \tag{2.15}$$

where,

The Bessel function expansion for the phase modulation terms is given as

$$\sin\left[A_0\sin(\omega_m t)\right] = \sum_{i=0}^{\infty} 2J_{2l+1}(A_0)\sin\left[(2l+1)\omega_m t\right] \tag{2.16}$$

$$\cos\left[A_0 \sin(\omega_m t)\right] = J_0(A_0) + \sum_{i=0}^{\infty} 2J_{2l}(A_0) cos\left[(2l)\omega_m t\right] \tag{2.17}$$

Which reduces the convolution term in the Fourier domain as

$$\Im\left[e^{-i\Phi}\right] = \sum_{l=0}^{\infty}\left[J_{2l}\left(A_0\right)\left\{\delta\left(k-2l\omega_m\right)+\delta\left(k+2l\omega_m\right)\right\} - J_{2l+1}\left(A_0\right)\left\{\delta\left(k-2(l+1)\omega_m\right)+\delta\left(k+2(l+1)\omega_m\right)\right\}\right] \tag{2.18}$$

where, J_0, J_{2l+1} and J_{2l} are the Bessel functions of the first kind of order $0, 2l+1$ and $2l$.

The choice of $A_0 = 2.405$ radians simplifies the equations of modulations giving $J_0(A_0) = 0$. However, it has been recently shown that the phase retardance values of the sample obtained from the system is independent of the choice of the amplitude of the EOM (Lu*, et al.*, 2012). Equation 2.18 implies that in k-space, the zeroth and the first order signals appear distinct and hence could be separated out to obtain the elements of the Jones matrix as described below:

$$\begin{aligned}\tilde{I}_{h0}(z) &= \frac{E_{hr}}{2}(J_{12}^{*} - J_{11}^{*}) \\ \tilde{I}_{v0}(z) &= \frac{E_{vr}}{2}(J_{22}^{*} - J_{21}^{*})\end{aligned} \tag{2.19}$$

and

$$\begin{aligned}\tilde{I}_{h1}(z) &= -\frac{J_1(A_0)E_{hr}}{2}(J_{12}^{*} + J_{11}^{*}) \\ \tilde{I}_{v1}(z) &= -\frac{J_1(A_0)E_{vr}}{2}(J_{22}^{*} + J_{21}^{*})\end{aligned} \tag{2.20}$$

where $\tilde{I}_{h0,v0}(z)$ and $\tilde{I}_{h1,v1}(z)$ are the zeroth- and first-order horizontally and vertically polarized OCT signals respectively.

The zeroth and first order signals detected along the two orthogonal channels can be rearranged to obtain the elements of the Jones matrix as follows:

$$E_{hr}J_{11}^{*} = -\left(\tilde{I}_{h0} + \frac{\tilde{I}_{h1}}{J_1(A_0)}\right) \tag{2.21a}$$

$$E_{hr}J_{12}^{*} = \tilde{I}_{h0} - \frac{\tilde{I}_{h1}}{J_1(A_0)} \tag{2.21b}$$

$$E_{vr}J_{21}^{*} = -\left(\tilde{I}_{v0} + \frac{\tilde{I}_{v1}}{J_1(A_0)}\right) \tag{2.21c}$$

$$E_{vr}J_{22}^{*} = \tilde{I}_{v0} - \frac{\tilde{I}_{v1}}{J_1(A_0)} \tag{2.21d}$$

In other words,

$$J_{measured} = \begin{bmatrix} J_{11} & J_{12} \\ J_{21} & J_{22} \end{bmatrix} = \begin{bmatrix} E_{hr}^{*} & 0 \\ 0 & E_{vr}^{*} \end{bmatrix} \begin{bmatrix} -\left(\tilde{I}_{h0}^{*} + \frac{\tilde{I}_{h1}^{*}}{J_1(A_0)}\right) & \left(\tilde{I}_{h0}^{*} - \frac{\tilde{I}_{h1}^{*}}{J_1(A_0)}\right) \\ -\left(\tilde{I}_{v0}^{*} + \frac{\tilde{I}_{v1}^{*}}{J_1(A_0)}\right) & \left(\tilde{I}_{v0}^{*} - \frac{\tilde{I}_{v1}^{*}}{J_1(A_0)}\right) \end{bmatrix} \tag{2.22}$$

But with the inclusion of polarisation controller and linear polariser in the reference arm of the interferometer, the amplitudes $\left|E_{hr}^{*}\right|$ and $\left|E_{vr}^{*}\right|$ are made equal with a constant phase offset term remaining in the equation given as

$$J_{measured} = \begin{bmatrix} 1 & 0 \\ 0 & e^{i\gamma} \end{bmatrix} \begin{bmatrix} -\left(\tilde{I}_{h0}^{*} + \frac{\tilde{I}_{h1}^{*}}{J_1(A_0)}\right) & \left(\tilde{I}_{h0}^{*} - \frac{\tilde{I}_{h1}^{*}}{J_1(A_0)}\right) \\ -\left(\tilde{I}_{v0}^{*} + \frac{\tilde{I}_{v1}^{*}}{J_1(A_0)}\right) & \left(\tilde{I}_{v0}^{*} - \frac{\tilde{I}_{v1}^{*}}{J_1(A_0)}\right) \end{bmatrix} = J_{offset}J_{all} \tag{2.23}$$

where, $\gamma = \arg(E_{hr}^{*}) - \arg(E_{vr}^{*})$ gives the term J_{offset}.

To compensate for the fibre induced birefringence and obtain the sample related properties including birefringence, diattenuation and optic axis information, surface Jones matrix is obtained which is taken as the reference matrix based on algorithm developed by Park *et al. (Park et al.,* 2004, 2005) in their fibre based PS-OCT scheme which was later on adopted by Yamanari *et al.* in their implementation of CPM-SS-PS-OCT (Yamanari*, et al.*, 2008). This is based on the assumption that light backscattering from the tissue does not affect the polarisation state of light incident onto the tissue.

The measured surface Jones matrix is given by:

$$J_{surf\_m} = J_{offset} J_{out} J_{in} \tag{2.24}$$

where, J_{out} and J_{in} are the Jones matrices describing the light propagation between EOM and the sample surface and that of sample surface and polarising beam splitter in the detection arm.

From surface calibration, we obtain

$$J_{measured} \cdot (J_{surf\_m})^{-1} = J_{all} \cdot (J_{surf\_m})^{-1} = J_{offset} J_{out} J_{sam} J_{in} J_{in}^{-1} J_{out}^{-1} J_{offset}^{-1} = J_{offset} J_{out} J_{sam} J_{out}^{-1} J_{offset}^{-1} \tag{2.25}$$

which upon matrix diagnolisation (Park*, et al.*, 2004) yields the sample properties as

$$J_U \begin{bmatrix} p_1 e^{i\frac{\eta}{2}} & 0 \\ 0 & p_2 e^{i\frac{\eta}{2}} \end{bmatrix} J_U^{-1} \tag{2.26}$$

where, p_1 and p_2 are the attenuation coefficients of the birefringent sample; and η, is the retardation and J_U is a general unitary matrix.

In order to reduce the effect of speckle noises on the surface Jones matrix, averaging across successive A-scans must be applied to the obtained Jones matrices of each A-scan. However, this PS-OCT system is phase-sensitive and the phase fluctations inherent in the system does not allow for direct averaging of the surface Jones matrix to obtain the sample Jones matrix. In this scheme of implementation, the two major sources of phase fluctuations introduced which result as artefacts seen in the obtained retardance images are described here. The first source of error is due to the asynchronous timing occuring between the light source sweep and the start of the A-scan data acquisition with the fluctuation in timing being describable by multiplication of a unitary Jones matrix during A-scan trigger, $J_{offset1}$. The second source of phase offset is between EOM modulation waveform and A-scan acquisition which is also describable using a Jones matrix, $J_{offset2}$ and they can overall be written as

$$J'_{measured} = J_{offset1} J_{measured} J_{offset2} = e^{i2\alpha z\varepsilon(n)} J_{out} J_{sample} J_{in} J_{offset2} \tag{2.27}$$

With the measured Jones matrix at the sample surface as:

$$J'_{surface} = e^{i2\alpha z\varepsilon(n)} J_{out} J_{in} J_{offset2} \tag{2.28}$$

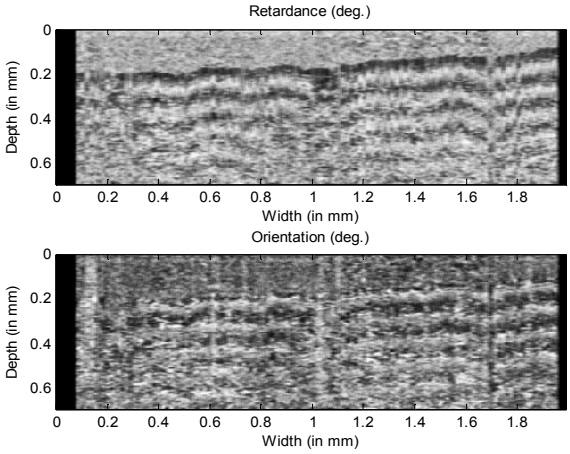

(a)

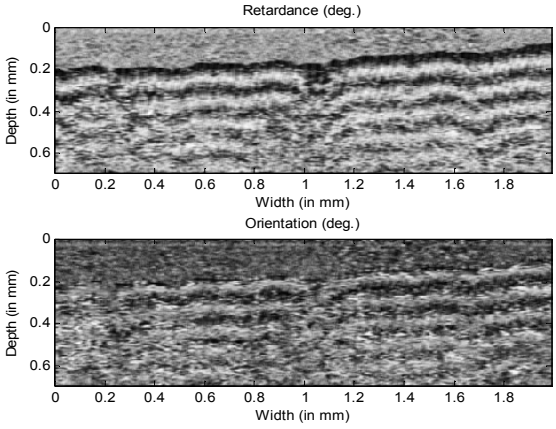

(b)

Figure 2.3: Phase retardance and optic axis orientation images (a) without and (b) with the global phase normalization implemented with the realisation of triggered burst mode to drive the EOM with A-scan trigger.

Previous study reported have tried to remove the phase fluctuation artefacts in retardance images obtained from PS-OCT system by including a static reflector (mirror) in the sample arm and then carrying on the phase calibration with respect to that optical component in the system (Vakoc *et al.*, 2005; Yamanari*, et al.*, 2009; Yamanari*, et al.*, 2008). As our implementation of CPM-PS-SS-OCT was based on a non-resonant EOM, the modulator

could be accurately synchronised to the A-scan trigger by the use of triggered tone-burst mode of the function generator that drives the EOM. This completely removes $J_{offset2}$. The global phases are removed from the surface Jones matrices by matrix normalisation followed by averaging over certain number of A-scans (Lu, *et al.,* 2011a). Figure 2.3 illustrates the removal of artefacts from retardance image with implementation of global phase normalisation with the realisation of triggered burst mode to drive the EOM with A-scan trigger.

2.5: Optic-axis measurements in TD-PS-OCT:

Measurement of the optic axis of the fibrous tissue based on PS-OCT data directly corresponds to the fibrillar orientation of the fibrous tissues based on the fact that the optic axis is directly related to the orientation of the fibre long axis. Hitzenberger *et al.* reported on a scheme of obtaining optic axis information based on single A-scan data analysis and phase sensitive detection in a standard time domain PS-OCT system (Hitzenberger *et al.*, 2001). Previously, various approaches have been made that require multiple polarization state as inputs (de Boer *et al.*, 1999; Roth *et al.*, 2001). Hitzenberger approach is based on the idea that phase difference measured between the two propagating modes in a birefringent medium encodes the orientation of optic axis (Everett *et al.*, 1998). However, this analysis based on the Jones calculus is applicable only for in-plane orientation of optic axis expressed using Jones matrix analysis of a linear retarder. The optic axis measured using Hitzenberger approach is given by:

$$\theta_{planar} = \frac{(\pi - \Delta\Phi)}{2} \tag{2.29}$$

A Soleil Babinet Compensator (SBC) (Thorlabs, SBC-IR; 1000-2000nm) was used to check the validity of the retardance and optic axis measurements carried out through our TD-PS-OCT system. SBC could be considered as a variable retarder with two wedges of birefringent material giving retardance over range $[0 \quad 2\pi]$ for a broad wavelength range. The SBC was calibrated for use at OCT wavelength of 1300nm and used in the OCT setup to validate the optic axis as well as retardance measurements. Arbitrary values of retardance and optic axis could be set using SBC. Two set of experiments were carried out. The first one was keeping the optic axis constant at values 0^o, 15^o …..90^o over constant step of 15^o, retardance values were measured for retardance of SBC varied from 0^o to 90^o in steps of 15^o. Measured versus set values of phase retardance is plotted in polar form in Figure 2.4, with the fixed fast axis values shown along the circumference of the plot. Deviations obtained between the measured and set retardance values could be attributed to the error in the calibration process carried out. Largest deviations are expected at $\delta = 0^o, 90^o$ because in these cases there is signal in one of the detection channel and the other channel is determined by the system noise level that leads to large errors in the experimentally obtained values.

In the second series of experiments, retardance values of SBC was kept fixed over 15^o, 30^o 45^o, 60^o and 75^o and the optic axis values were varied from 0^o to 180^o over a step of 15^o (Figure 2.5 in polar form and Figures 2.6 & 2.7 in scatter plot). However, accurate measurement of optic axis values could not be made when SBC retardance is set at 0^o as shown in Figure 2.7, where for $\delta = 0^o$, optic axis was varied over 0^o to 90^o at a step of 15^o and obtained optic axis readings were plotted. Similar values of inaccurate optic axis values would be obtained if retardance value is set at 90^o. This is mainly due to the absence of signal in one of the channel of the TD-PS-OCT detector scheme. The Hitzenberger approach has been based on the assumption that the sample for which optic axis measurements are carried

out is unilayered birefringent material with a constant optic axis orientation along the depth of the sample.

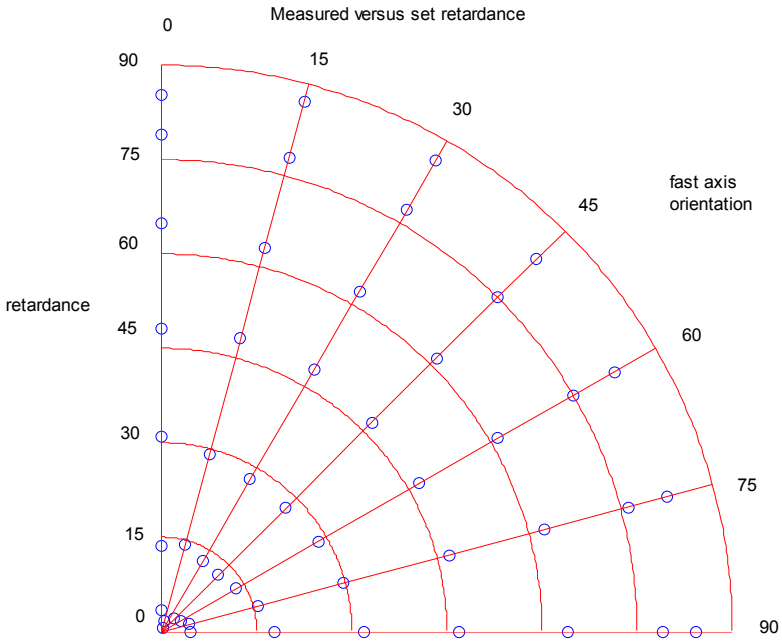

Figure 2.4: Polar plot of measured retardance versus set retardance for different fixed values of optic axis shown along the circumference of the plot. The blue circles represent the measured retardance values.

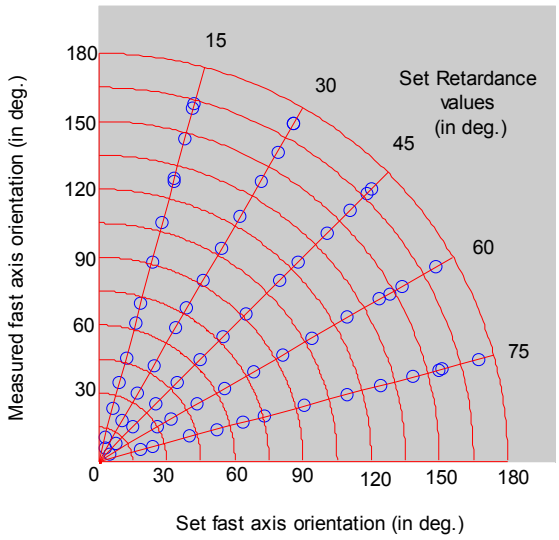

Figure 2.5: Polar plot of measured optic axis orientation versus set optic axis orientation for different fixed values of retardance for SBC, shown along the circumference of the plot. The blue circles represent the measured optic axis values.

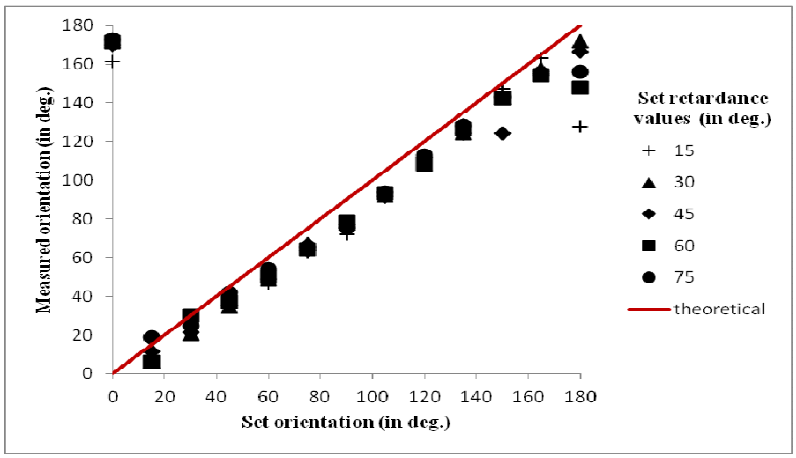

Figure 2.6: Plot of measured optic axis orientation versus set optic axis orientation for different fixed values of retardance set for SBC from 15^{o} to 75^{o}.

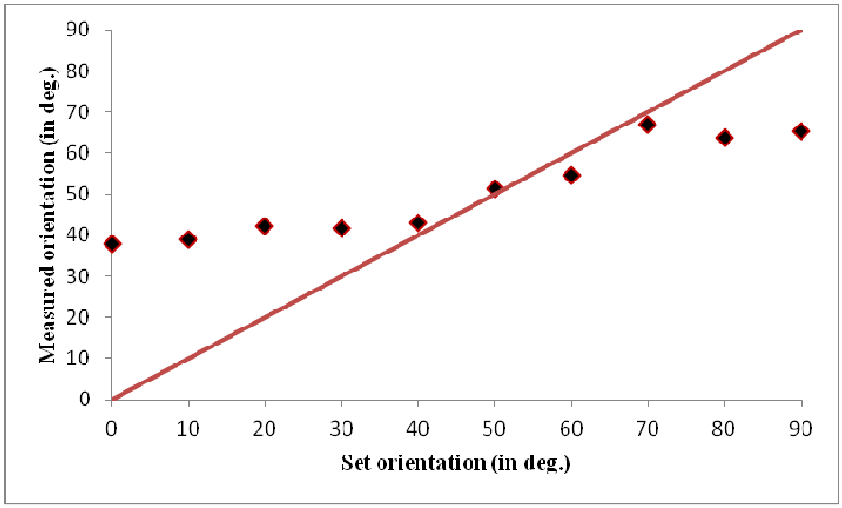

Figure 2.7: Plot of measured optic axis orientation versus set optic axis orientation for retardance value set at 0^o. Note the inaccuracy in the measurement of optic axis. The absence of signal in one of the detection channels of PS-OCT leads to the large errors obtained here as the obtained values are completely determined by the random system noise fluctuations.

2.6: Optic axis measurements in CPM-SS-PS-OCT:

Validation of the optic axis measurements using CPM-SS-PS-OCT system is carried out using a true zero order waveplate centred at 1310nm (WPF410, Crylight). The thickness of this three-quarter waveplate (TQWP) is 115μm. The optic axis orientation of TQWP was changed in steps of 10^o and the optic axis measurements were made according to the approach put forward by Jiao *et al.* (Jiao & Wang, 2004), which is based on the polarimetric ellipsometry which defines an apparent optic axis of an elliptic retarder as the orientation of the major axis of the eigenpolarisation ellipse (Jones, 1941). For a general elliptical retarder $J(\phi,\alpha,\delta)$ where ϕ gives the retardance, α and δ are the parameters that describe the eigenvectors of J. This means for a elliptic retarder, the major axis orientation, ψ is given by

$$\tan 2\psi = \tan 2\alpha \cos\delta = \frac{U}{Q} \tag{2.30}$$

where U and Q represents the Stokes parameters given as

$$\begin{bmatrix} Q \\ U \\ V \end{bmatrix} = \begin{bmatrix} \cos 2\chi \cos 2\psi \\ \cos 2\chi \sin 2\psi \\ \sin 2\chi \end{bmatrix} = \begin{bmatrix} \cos 2\alpha \\ \sin 2\alpha \cos\delta \\ \sin 2\alpha \sin\delta \end{bmatrix} \tag{2.31}$$

Here, ψ, χ specifies the orientation of the polarisation ellipse.

This implies that the optic axis orientation is defined with respect to the Stokes vector and is measured as angle between the projection of this vector onto the QU plane and the $Q-$axis. However, it is also shown by Lu *et al.* that the linearity relation between measured and set orientations of a quarter wave plate is not always maintained (Lu*, et al.*, 2011b). Park *et al.* described another method to measure the apparent optic axis orientation by calculating the angle subtended by the two Stokes vectors obtained for a sample at two different orientations, which bears a linear relationship with the apparent optic axis orientation (Park*, et al.*, 2005). However, a sign ambiguity occurs in this method that makes it difficult to deduce the sign (positive or negative) of relative change of the optic axis orientation.

The orientation of TQWP was rotated from 0^o to 180^o over increments of 10^o and optic axis measurements were carried out using Wang's method by averaging out 128 depth scans. Figure 2.8 gives the optic axis orientation obtained for TQWP. The average double-pass phase retardance was obtained as 173 ± 3 and is shown in Figure 2.9 for different values of set optic axis orientation.

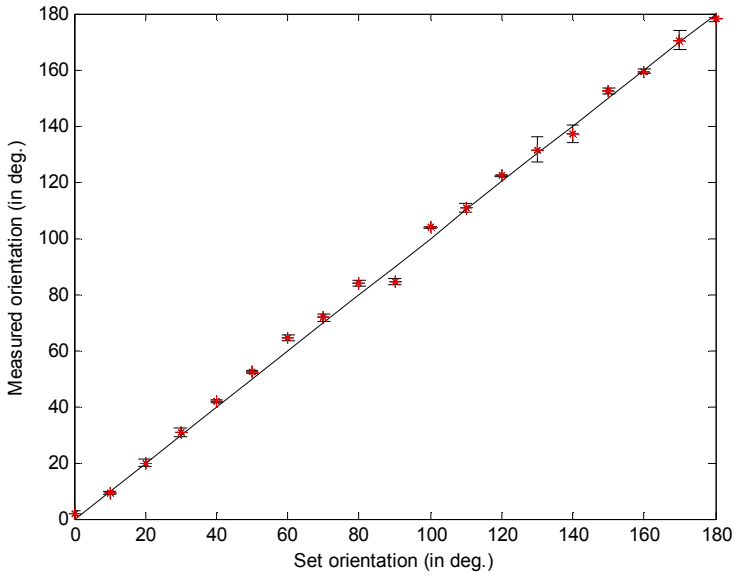

Figure2.8: Relative optic axis measurement of the TQWP using CPM-SS-PS-OCT system and the Wang's method.

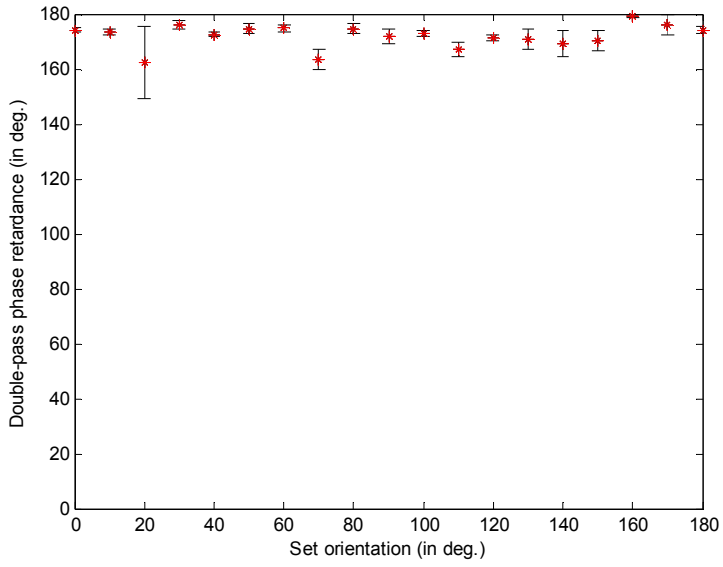

Figure.2.9: Double-pass phase retardance measured for TQWP

A biological sample was also used as test validation to optic axis measurements using CPM-SS-PS-OCT system. Equine tendon sample was used for this study which has a unilayer orientation of collagen fibres parallel to the tissue surface. The sample was mounted on the imaging plane normal to the incident light and was rotated in increments of 10^{o} over 180^{o} half circle rotation. The relative optic axis measurements were carried out using Wang's method (Jiao & Wang, 2004) over 50 A-scans averages. Averaging was carried out to reduce the variability arising due to the biological sample as well as the system noises. Figure 2.10 and 2.11 shows the relative optic axis measurements obtained using two different implementations of digitisers in CPM-SS-PS-OCT system.

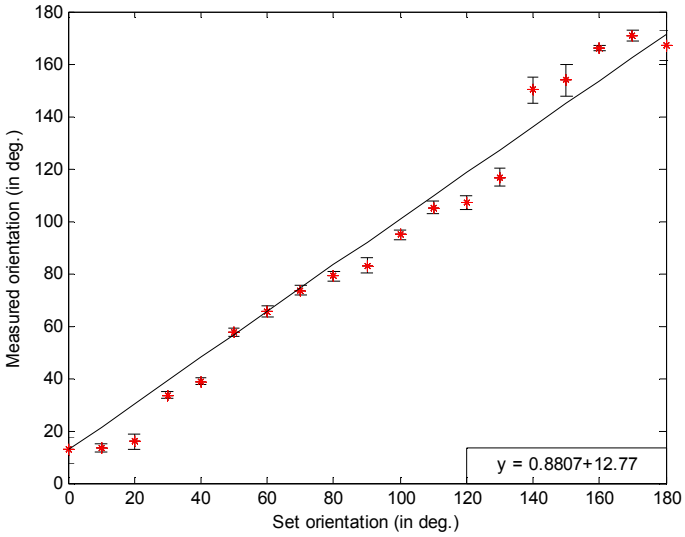

Figure 2.10: Measured optic axis orientation of equine tendon versus set orientation plot using 14 bit digitizer (M2i.4022, Spectrum GmbH, Germany) at 20MS/s

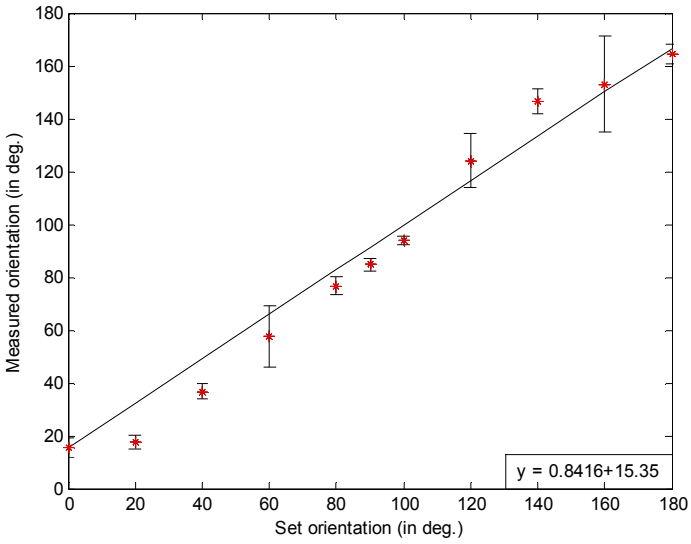

Figure 2.11: Measured optic axis orientation of equine tendon versus set orientation plot using 8 bit digitizer (M2i.2031, Spectrum GmbH, Germany) at 100MS/s. In this case, the set optic axis orientation was incremented over steps of 20^{o}.

2. 7: Multi-angle (angle-resolved) PS-OCT measurements:

The optic axis measurement schemes discussed in the earlier sections do not fully provide the 3D information about the fibre long axis orientation. The whole assumption in the previous section is based on modelling the tissue as a linear retarder to obtain the birefringent properties or the optic axis information over normal incidence of light beam and in-plane geometry of optic axis. However, to understand the orientation information of complicated architecture of collagen-based tissues like cornea or articular cartilage, a new modelling scheme has to be proposed that gives the full 3D information of the microstructure of the tissue. Variable angle technique was first put forward by Ugryumova *et al.* to extract the 3D information of the optic axis of the biological tissue like tendon, cartilage, etc (Ugryumova *et al.*, 2006). Recent experiments by Huang *et al.* have reported the effect of optical beam angle

on quantitative OCT signal in normal and mechanically degraded bovine articular cartilage (Huang *et al.*, 2011). Different quantitative OCT parameters were reported for their potential applications in distinguishing normal cartilage sample from the degraded sample based on small angle inclination of up to 10^{o}. In this thesis, multi-angle PS-OCT measurements are carried out in two orthogonal planes with respect to the surface normal of the tissue surface as depicted in Figure 2.12. The main motivation behind this idea is that the birefringence of the collagen fibre obtained is a parameter dependent on the direction of the light beam incident on the material as well as the angle it makes with the optic-axis of the material. Hence, the concept of true and apparent birefringence being different over different angles of light beam incidence (Section 1.4.3 & 1.4.4) is the main reason behind implementing this idea to extract the complete orientation information of the collagen fibres in complicated scenario as seen in articular cartilage (Jeffery *et al.*, 1991). The rationale behind this is the collagen fibres show high birefringence when viewed across the fibres in the tissue and a low birefringence when viewed along the fibre length of the tissue as discussed in Chapter 1. A detailed analysis of the apparent birefringence obtained from different angles of incidences uniformly distributed along the orthogonal planes with respect to the surface normal of the tissue then yields the full details of the optic axis orientation of the collagen fibre. The quantification of the non-planar orientation of the optic axis is carried out using EJMC modelling of articular cartilage as a layered birefringent structure with varying orientation of optic axis. More details of the theoretical aspects of the modelling are given in the section below (Section 2.8). Propagation of polarized light in layered anisotropic media could also be developed based on Monte Carlo algorithm taking into account the random simulation of photon path lengths along a layered medium characterised as a highly scattering medium using Mie scattering (Gangnus *et al.*, 2004; Wang & Wang, 2002). However, this simulation is tedious with huge computational

requirements. Thus, EJMC has been the choice of framework to develop layered model of articular cartilage in this thesis, which provides a more simple approach for the objective presented.

Multi-angle PS-OCT measurements were carried out in the biological samples (equine tendon sample and bovine articular cartilage sample) in two different orthogonal planes, $x-z$ and $y-z$ (Figure. 2.12). The x, y, z Cartesian coordinate system is defined such that the z-axis represents the axial depth direction. The $x-z$ and $y-z$ planes corresponds to the coronal and sagittal planes, defined as the plane in which the two connected bones are constrained to move in and the orthogonal plane, respectively. Hence in general, these planes are oriented at an unknown angle with respect to the azimuthal orientation of the superficial collagen fibres of articular cartilage. Whereas for tendon sample, because of the unidirectional orientation and visual realisation of the orientation of the collagen long axis, the $x-z$ plane was chosen to be fibre long axis direction and $y-z$ plane was chosen to be across the fibre long axis plane. It is a very simple choice of coordinate system with a uniform orientation of collagen fibres unlike that of articular cartilage. Figures 2.13 - 2.16 shows the multi-angle measurements obtained from PS-OCT systems for equine tendon sample and bovine articular cartilage samples, with retardance profiles averaged over 50A-scans shown alongside each phase retardance images. These data were then input into EJMC framework to establish the relation between obtained phase retardance data over oblique incidence and the built-in network of collagen fibres, as will be discussed later on in the following sections of this chapter.

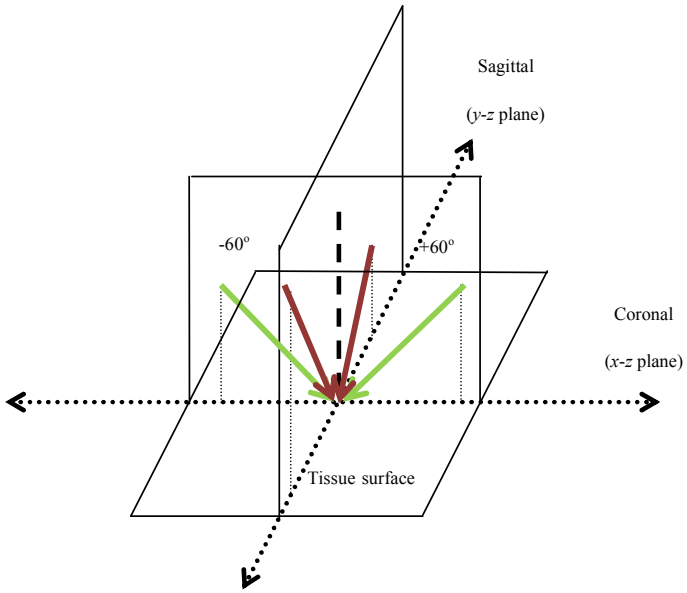

Figure2.12: Schematic of the multi-angle measurement set-up used for the study. The measurements are carried out in two orthogonal planes (sagittal and coronal) with oblique light incidence with respect to normal (here shown as $\pm 60^{o}$)

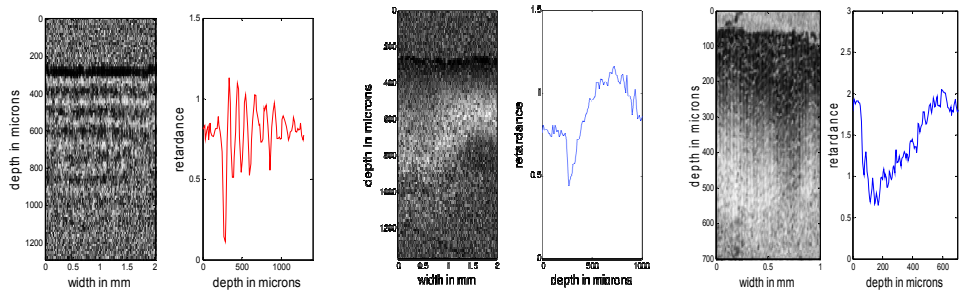

(a) (b) (c)

Figure 2.13: Phase retardance images and corresponding retardance profiles averaged over 50 A-scans obtained for normal incidence of light for (a) Equine tendon sample of 6year old horse using TD-PS-OCT system (b) Bovine articular cartilage sample using TD-PS-OCT system (c) Bovine articular cartilage sample using CPM-SS-PS-OCT system.

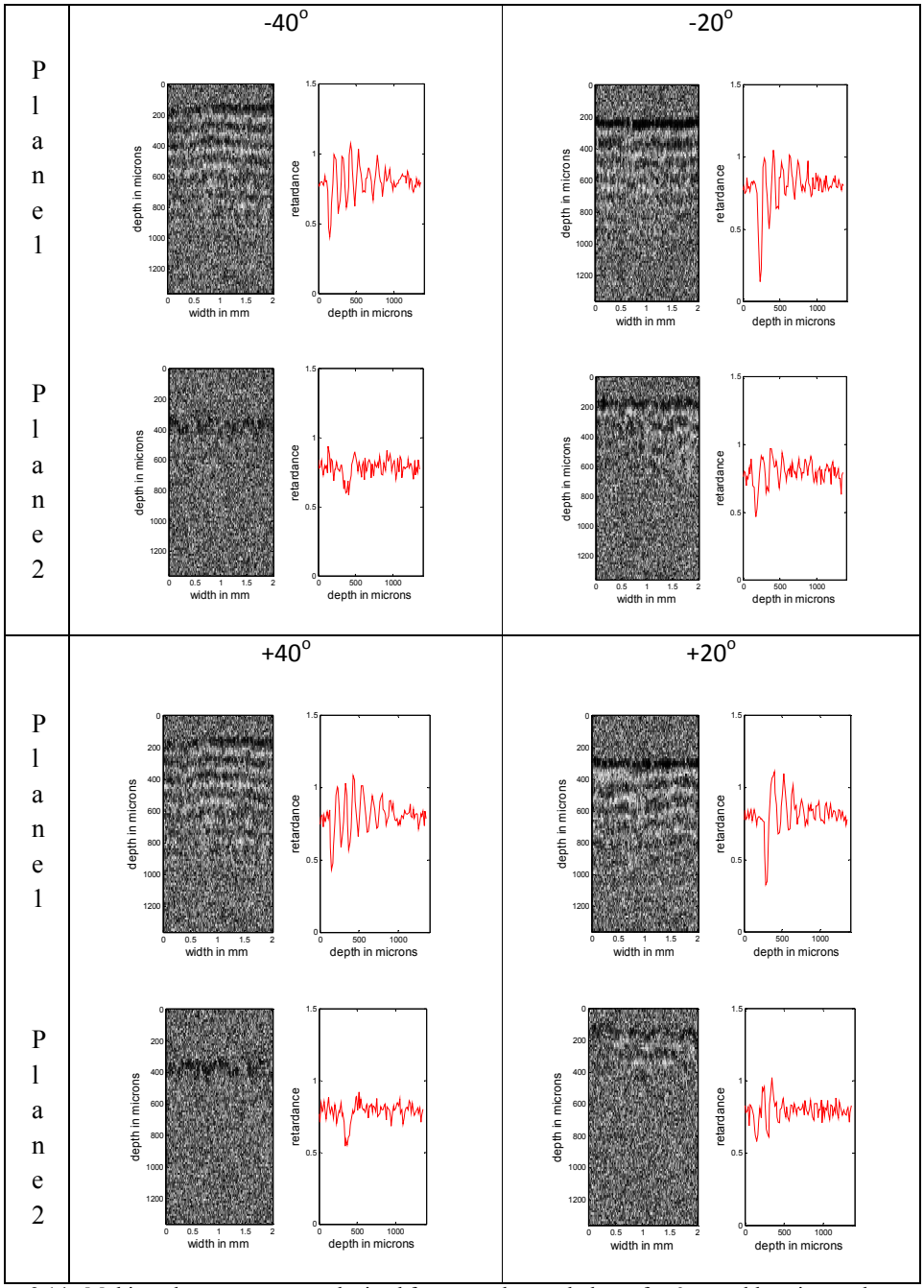

Figure 2.14: Multi-angle measurements obtained for two orthogonal planes for 6 year old equine tendon sample at oblique incidence angles, $\pm 40^{o}, \pm 20^{o}$ with respect to the surface normal, using TD-PS-OCT.

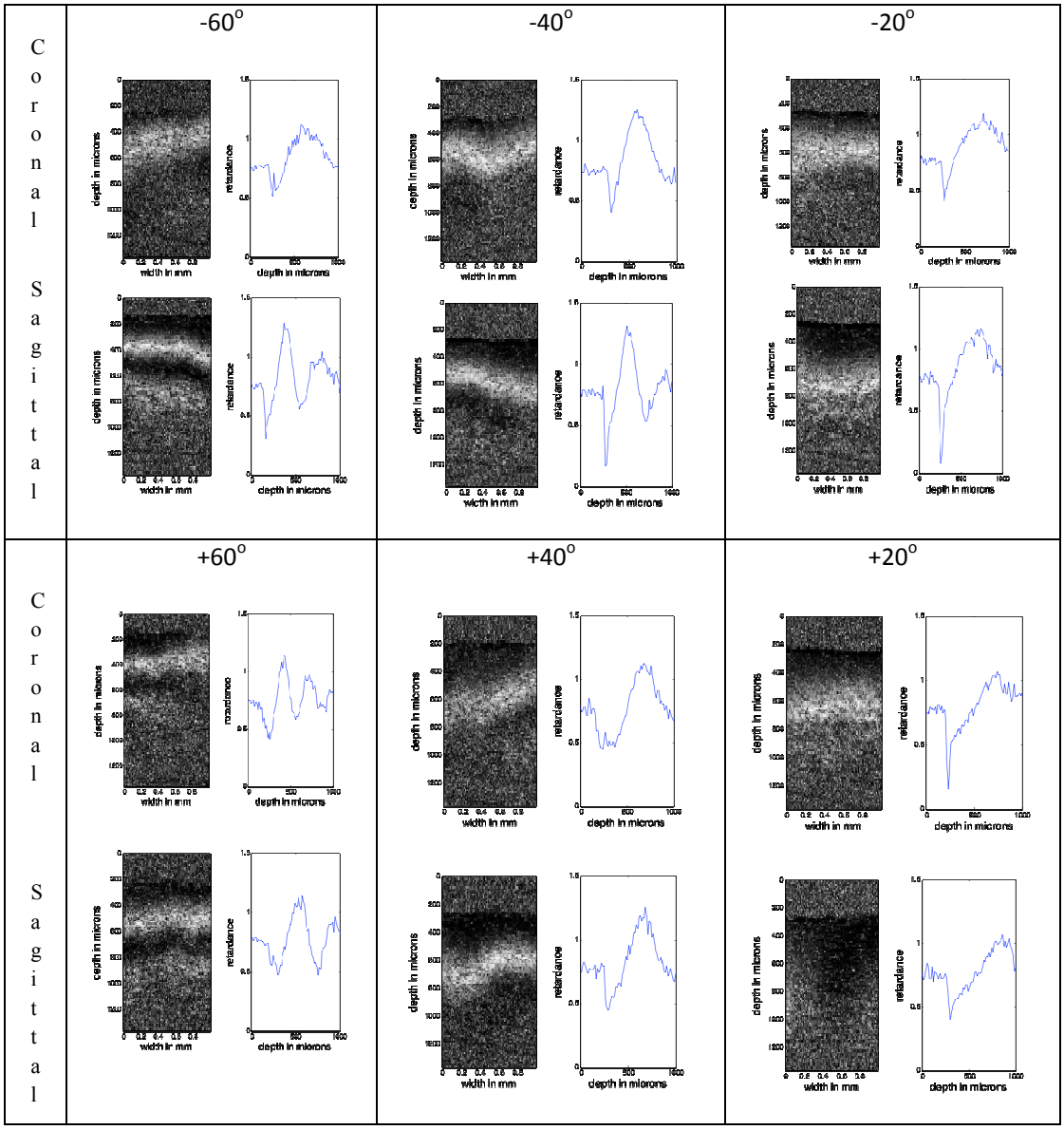

Figure 2.15: Multi-angle measurements obtained for two orthogonal planes (coronal and sagittal) for bovine articular cartilage sample at oblique incidence angles, $\pm 60^{o}, \pm 40^{o}, \pm 20^{o}$ with respect to the surface normal, using TD-PS-OCT.

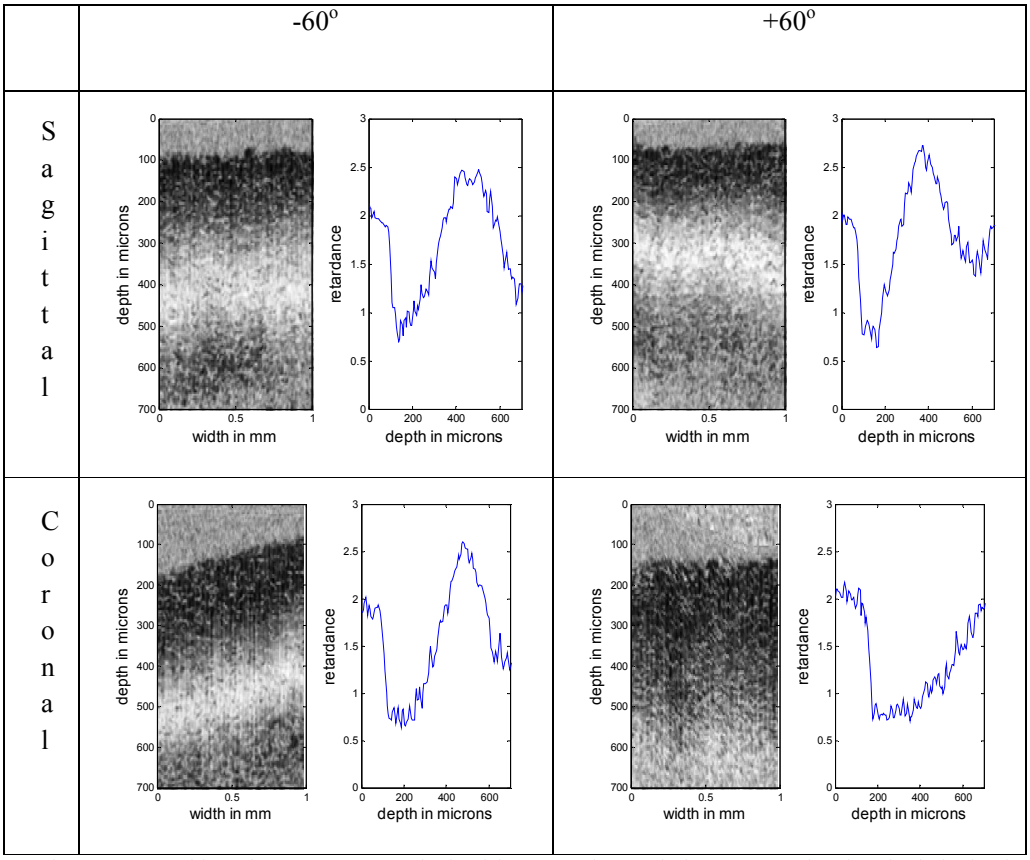

Figure 2.16: Multi-angle measurements obtained for two orthogonal planes (coronal and sagittal) for bovine articular cartilage sample at oblique incidence angles, $\pm 60^{o}$ with respect to the surface normal, using TD-PS-OCT.

2.8: Extended Jones matrix calculus (EJMC):

Extended Jones matrix calculus was described by Yeh in 1982 (Yeh, 1982) and subsequent paper by Gu and Yeh in 1993 (Gu & Yeh, 1993). This extends the Jones matrix calculus developed by Jones in 1941 to analysis of linear retarders of arbitrary state of optic axis (out of plane or in-plane) and also for off-axis light beam incident on the retarder. This was shown by Yeh for polarized light beam propagation in liquid crystal models. However, this could be easily extended to a biological sample (Fanjul-Vélez & Arce-Diego, 2010; Fanjul-Velez *et al.*, 2010; Gangnus, *et al.*, 2004). This model has been extended to study the optic axis

orientation of collagen fibres in articular cartilage. Articular cartilage is modelled as a series of linear retarder with different orientation of optic axis over depth of the tissue that gives the cumulative birefringent information as obtained using a PS-OCT system. EJMC has been applied to this articular cartilage model with the assumption of weak birefringence given by:

$$\Delta n = |n_e - n_o| << n_o, n_e \tag{2.32}$$

where, n_e and n_o are the refractive indices of the extraordinary and ordinary modes of light beam propagation. The values of true birefringence, Δn reported in the literature for articular cartilage sample from different animals of various age groups range from 0.45×10^{-3} to 3×10^{-3}. The values reported in the literature are $(0.45\pm0.12)\times10^{-3}$ for four month old porcine sample and $(1.48\pm0.55)\times10^{-3}$ for 21 month old porcine sample (Rieppo *et al.*, 2009). For bovine sample, the value reported was 3×10^{-3} by Jiao *et al.* (Jiao & Wang, 2002).

EJMC approach is also based on the assumption of negligible multiple reflections occurring at different layers of the multi-layered birefringent structures. The choice of coordinate system is such that z-axis corresponds to the depth of the articular cartilage. The two orthogonal planes $x-z$ and $y-z$ are the sagittal and coronal planes as per the animal anatomical plane sections. Then the orientation of the optic-axis is given as

$$\hat{c} = (\hat{x}\cos\phi_c + \hat{y}\sin\phi_c)\sin\theta_c + \hat{z}\cos\theta_c \tag{2.33}$$

Where ϕ_c and θ_c are the azimuth and polar angle of the fibre long axis represented by unit vector, $\hat{c}$. This $\hat{c}-$axis representation is from the notations used in crystal optics that describes that dielectric permittivity along three mutually perpendicular unit vectors as

$\hat{a},\hat{b},\hat{c}$ where $\hat{c}$ represents the long axis of a cylinder geometry of the collagen fibre (C_∞ rotational symmetry) (Ugryumova*, et al.*, 2006).

The EJMC calculus proceeds with the treatment of reflection and transmission along the multi-layered interfaces of transverse electromagnetic wave based on the propagation of the two transverse modes-TE waves (s-waves) and TM waves (p-waves). The transmission coefficients are obtained upon imposing the boundary conditions on the electric and magnetic fields in the equations of the electromagnetic beam propagation using Maxwell's equations. The crystal optics theory is such that the k-vector incident on the positive uniaxial crystal in this case cylindrical collagen fibre inclined at an angle θ_c to the c-axis of the optic axis, the refractive indices of the two modes of propagation that are mutually orthogonal to each other are given by

$$\frac{1}{n^2} = \frac{\sin^2\theta_c}{n_e^2} + \frac{\cos^2\theta_c}{n_o^2} \tag{2.34}$$

and

$$n = n_o \tag{2.35}$$

for extraordinary and ordinary modes, respectively.

Here, the collagen fibres are treated as positive uniaxial crystals, with $n_e > n_o$

We also obtain the normal mode of propagation for extraordinary wave given by:

$$\frac{k_{ea}^2 + k_{eb}^2}{n_e^2} + \frac{k_{ec}^2}{n_o^2} = \left(\frac{\omega}{c}\right)^2 \tag{2.36}$$

where, based on the $\hat{a},\hat{b},\hat{c}$ crystal optics coordinate system,

$$\begin{aligned} k_{ea} &= (\alpha\cos\phi_c + \beta\sin\phi_c)\cos\theta_c - k_{ez}\sin\theta_c \\ k_{eb} &= -\alpha\sin\phi_c + \beta\cos\phi_c \\ k_{ec} &= (\alpha\cos\phi_c + \beta\sin\phi_c)\sin\theta_c + k_{ez}\cos\theta_c \end{aligned} \tag{2.37}$$

Equation 2.36 is reduced it to a quadratic equation in the extraordinary component of the wavevector in z-direction.

$$uk_{ez}^2 - vk_{ez} + w = 0 \tag{2.38}$$

where,

$$u = \frac{\sin^2\theta_c}{n_e^2} + \frac{\cos^2\theta_c}{n_o^2} \tag{2.39}$$

$$v = k_d\sin(2\theta_c)\left(\frac{1}{n_e^2} - \frac{1}{n_o^2}\right) \tag{2.40}$$

$$w = \frac{k_d^2\cos^2\theta_c + k_{eb}^2}{n_e^2} + \frac{k_d^2\sin^2\theta_c}{n_o^2} - \left(\frac{\omega}{c}\right)^2 \tag{2.41}$$

with

$$k_d = \alpha\cos\phi_c + \beta\sin\phi_c \tag{2.42}$$

Thus the magnitude of the z-component of the extraordinary wave is obtained as the positive solution of the quadratic equation solving for k_{ez}.

$$k_{ez} = \frac{\left[v + \sqrt{v^2 - 4uw}\right]}{2u} \tag{2.43}$$

The z component of the ordinary wavevector which is independent of the orientation of the optic axis is given by:

$$k_{oz} = \left[\left(n_o \omega / c \right)^2 - \alpha^2 - \beta^2 \right]^{1/2} \tag{2.44}$$

where, α and β are the x-component and y-component of the k-vector. Thus, for a linear birefringent element, based on the ordinary and extraordinary components of the z-component of the k-vector, its Jones matrix is given as

$$L_{ret} = \begin{bmatrix} e^{-ik_{oz}d} & 0 \\ 0 & e^{-ik_{ez}d} \end{bmatrix} \tag{2.45}$$

For a complex 3D architecture of collagen network in articular cartilage as described in Section 1.8.1 of the previous chapter, a lamellar model put forward by Jeffery *et al.* with a leaf-like arrangement of the collagen fibres (Figure 2.17) (Jeffery*, et al.*, 1991).

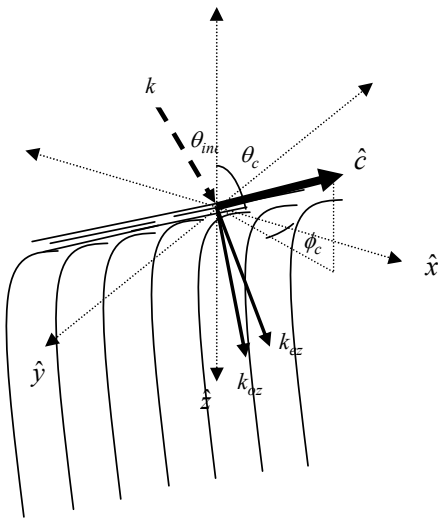

Figure 2.17: A schematic showing the EJMC approach to modelling the zonal layered structure of articular cartilage. Here ϕ_c and θ_c gives the azimuthal and polar angle of the collagen fibre direction i.e. the optic axis. The incident angle θ_{inc} is varied with respect to the surface normal of the tissue over two orthogonal planes to obtain the multi-angle PS-OCT data.

Based on the model assumed for articular cartilage, the layered geometry could be mathematically put as:

$$J_{sample} = T_o P^T P T_i \tag{2.46}$$

With

$$P = \prod_{i=m}^{1} R(-\psi_i) \begin{pmatrix} e^{-ik_{oz_i} d_i} & 0 \\ 0 & e^{-ik_{ez_i} d_i} \end{pmatrix} R(\psi_i) \tag{2.47}$$

Here, T_i and T_o gives the input and output Fresnel reflection coefficient at the air tissue interface.

$$T_i = \begin{pmatrix} t_s & 0 \\ 0 & t_p \end{pmatrix} \tag{2.48}$$

$$T_o = \begin{pmatrix} t'_s & 0 \\ 0 & t'_p \end{pmatrix} \tag{2.49}$$

The Fresnel transmission coefficients for s-wave and p-wave on entering the birefringent medium, t_s, t_p and upon leaving the medium, t'_s, t'_p given by the Equations 2.50 – 2.53 (Figure 2.18):

$$t_s = \frac{2n\cos\theta_{inc}}{n\cos\theta_{inc} + n_o\cos\theta_o} \tag{2.50}$$

$$t_p = \frac{2n\cos\theta_{inc}}{n\cos\theta_o + n_o\cos\theta_{inc}} \tag{2.51}$$

$$t'_s = \frac{2n_o\cos\theta_o}{n_o\cos\theta_o + n\cos\theta_{inc}} \tag{2.52}$$

$$t_p^{'} = \frac{2n_o \cos\theta_o}{n_o \cos\theta_{inc} + n\cos\theta_o} \tag{2.53}$$

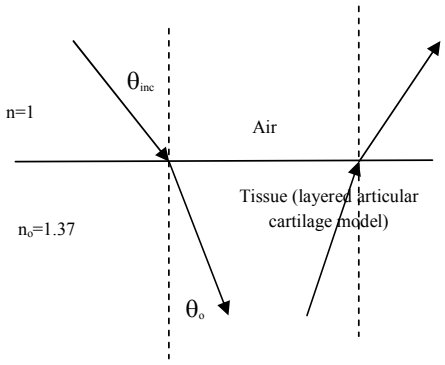

Figure 2.18: Schematic showing the light beam propagation along air-tissue interface in order to calculate the Fresnel transmission coefficients for the light beam propagation.

In this case, $n = 1$ for the air and the refractive index of the medium is $n_o = 1.37$.

For articular cartilage EJMC simulation over an oblique incidence angle of 60^o,

$t_s = 0.64, t_p = 0.68, t_s^{'} = 1.36, t_p^{'} = 1.45$

which gives, s-wave transmittance as 0.87 and p-wave transmittance = 0.99 .

The Fresnel transmission coefficients are calculated based on the small birefringence assumption which is given by:

$$\left|n_e - n_o\right| \ll n_o, n_e \tag{2.54}$$

This assumption implies that the angle of refraction of the ordinary and extraordinary component as almost equal to each other, i.e, $\theta_e \simeq \theta_o$ which leads to the approximate equations for the two polarization modes as:

$$\hat{o} \simeq \frac{\hat{c} \times k_o}{\left|\hat{c} \times k_o\right|} \tag{2.55}$$

$$\hat{e} \simeq \frac{k_o \times \hat{o}}{|k_o \times \hat{o}|} \tag{2.56}$$

The s-wave and p-wave retain their respective polarization states upon refraction at the interface. Here, $\hat{p}_o$ is the unit vector perpendicular to both $\hat{s}$ and k_o given as

$$\hat{p}_o = \frac{k_o \times \hat{s}}{|k_o \times \hat{s}|} \tag{2.57}$$

The set of coplanar orthogonal unit vectors $(\hat{s}, \hat{p}_o)$ and $(\hat{o}, \hat{e})$ are defined with respect to angle ψ as a rotation in the coordinate system from x, y, z based on s-wave and p-wave analysis to that defined by the unit vectors $\hat{e}$ and $\hat{o}$ of the extraordinary and ordinary modes as (Figure 2.19)

$$\begin{aligned} \hat{o} &= \hat{s}\cos\psi + \hat{p}_o \sin\psi \\ \hat{e} &= \hat{s}\sin\psi + \hat{p}_o \cos\psi \end{aligned} \tag{2.58}$$

Hence, $R(\psi_i)$ in Equation (2.47) of the individual layers of the multi-layered articular cartilage model gives the transformation matrix for the rotation of coordinate system based on the light beam propagation in the birefringent tissue.

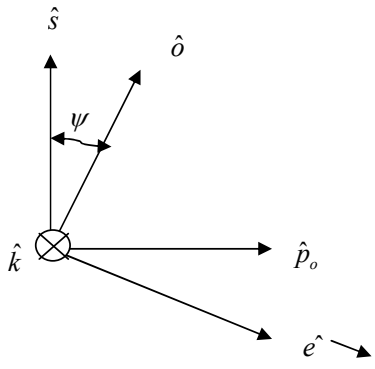

Figure 2.19: The rotation of the coordinate system with respect to extraordinary and ordinary modes of propagation and s- & p-wave analysis of electromagnetic wave

Thus,

$$R(\psi_i) = \begin{pmatrix} \cos\psi_i & -\sin\psi_i \\ \sin\psi_i & \cos\psi_i \end{pmatrix} \tag{2.59}$$

expresses the light beam propagation in terms of normal modes (o-wave and e-wave) of propagation in birefringent element, with

$$\cos\psi_i = \frac{\cos\theta_{oi}\sin\phi_c}{\sqrt{1-\sin^2\theta_{oi}\sin^2\phi_c}}$$
$$\sin\psi_i = \frac{-\cos\phi_c}{\sqrt{1-\sin^2\theta_{oi}\sin^2\phi_c}} \tag{2.60}$$

where, θ_{oi} is the angle of refraction as obtained from Snell's law over the air tissue interface.

Thus, Jones matrix for the layered cartilage sample is obtained by putting in the orientation information based on the azimuthal and polar angle orientation of the optic axis in different layers. However, the optic axis information for these layers is input based on the histological zones found in the articular cartilage.

We start implementing the comparative study based on EJMC and PS-OCT data trying to obtain a good fit for the depth-dependent retardance information obtained from TD-PS-OCT and the depth-dependent information obtained from the layered EJMC model. The depth dependent retardance profiles from EJMC data to simulate TD-PS-OCT is done by obtaining the orthogonal components of amplitudes of electric fields by tracing the light beam path of the circular polarized light onto sample and then back into the detectors. Referring to the schematic of TD-PS-OCT in Section 2.3 (Figure 2.1), the Jones calculus is given by:

$$\begin{pmatrix} A_H(z) \\ A_V(z) \end{pmatrix} = R(45^o).QWP.R(-45^o).J_{sample}.\frac{1}{\sqrt{2}}\begin{pmatrix} 1 \\ i \end{pmatrix} \tag{2.61}$$

Which gives the depth dependent retardance as

$$\delta_{EJMC}(z) = \tan^{-1}\left(\frac{A_V(z)}{A_H(z)}\right) \tag{2.62}$$

Here, J_{sample} is the Jones matrix obtained for multi-layered model as described in Equation (2.46-2.53).

The preliminary investigation of the implementation of the EJMC layered model to understand the optic axis properties of complex architecture of articular cartilage based on the obtained depth dependent retardance values of PS-OCT over multi-angle measurements was carried out by dividing the articular cartilage model into '$m = 22$'. The choice of 22 layers is mainly due to ease of simulation or convenient choice of thickness for a total articular cartilage thickness of 1mm (Figure 2.20).

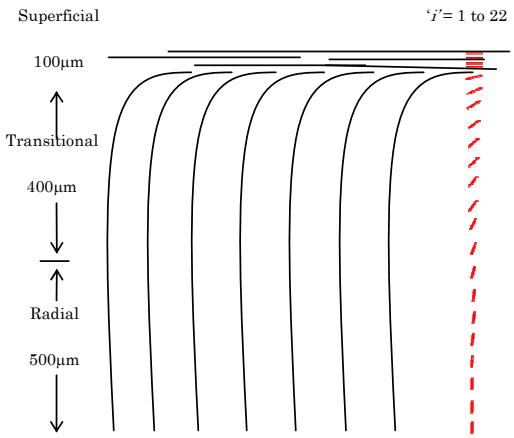

Figure. 2.20: A schematic of the cartilage zonal layered structure and the layer thickness used for the EJMC study. Also shown are the orientations of the polar angle of the collagen optic axis varying from 90^o in the superficial zone to gradually becoming 0^o in the radial zone.

Of the broader histological zones, superficial layer is assumed to be of thickness 100µm divided into 4 layers of uniform thickness. Transitional and radial zone consists of remaining

individual layers each of thickness 50μm, with transitional zone of thickness 400μm and radial zone, the rest of the thickness of the tissue. The optic axis orientation information input into the model is tabulated below (Table 2.1). A simple assumption of constant azimuth over depth of the tissue was assumed as well. Table 2.2 presents the optical path length changes calculated over the broader histological zones for the various oblique incidences of light beam to be incorporated in the EJMC model (Table 2.2).

Table 2.1: Tabulated values for the values of polar angle θ_c input into layered EJMC articular cartilage model based on histological zones in the tissue.

Histological zones	Individual layers	Polar angle
Superficial	1	90
	3	90
Transitional	5	90
	7	80
	9	70
	11	60
	13	50
Radial	15	1
	17	1
	19	1
	21	1

The simulation was carried out for an assumption of true birefringence value of $\Delta n = 2 \times 10^{-3}$, with a simple model of constant values of ordinary and extraordinary refractive indices along the depth of the tissue. Although this assumption may not be strictly true, the main aim of this

study was to obtain a model to study the anisotropic properties exhibited by articular cartilage. The value of true birefringence input in the model was chosen based on the available information in the literature on articular cartilage as discussed earlier in this section. The results are obtained for an assumption of azimuth angle of 0^o. Table 2.2 tabulated the optical path length that has to be accounted for with respect to the simulated model for different oblique incidence of light beam. Figure 2.21 shows the simulated EJMC phase retardance profile obtained for normal incidence. A steady line after a depth of 600μm represents the radial region when the normally incident beam of light is parallel to the long axis orientation of the collagen fibre, which gives rise to steady cumulative retardance profiles. A quick glance at Figure 2.15 and Figure 2.22 showing the angle resolved depth dependent retardance plots obtained from PS-OCT strikes a similarity between the nature of banding patterns obtained over different oblique incidence angles. However, the retardance values in experimental data wrap around at values well below the range $[0 \quad \pi/2]$ in case of TD-PS-OCT. This is owing to the system noise involved in the PS-OCT measurements. The inclusion of a noise model in the simulation of depth dependent retardance values as obtained from TD-PS-OCT system is discussed in more details in the next section (Section 2.9). With this initial study, fine tuning of the input parameters in the EJMC model of articular cartilage is carried out with inclusion of the noise model, to obtain a good curve fit of the multi-angle retardance profiles from PS-OCT measurements and that obtained from EJMC simulation.

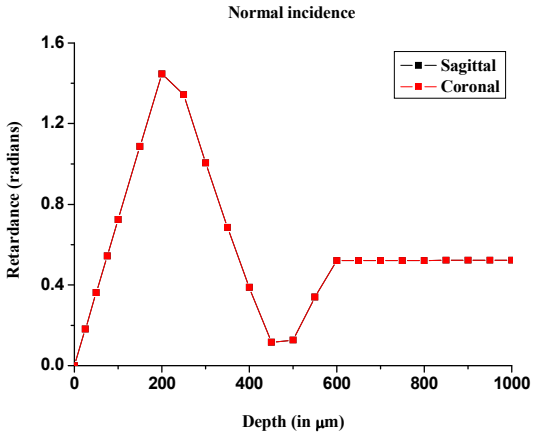

Figure 2.21: Phase retardance profile obtained for normal incidence over two orthogonal planes simulated using EJMC articular cartilage model.

Table 2.2: Optical path length calculated for the histological zones of articular cartilage for different angles of oblique incidence for a refractive index of articular cartilage assumed to be 1.38 (Wang *et al.*, 2008)

Angle of incidence with respect to surface normal	Angle of refraction inside the tissue surface	Optical path length in superficial zone (in microns)	Optical path length in transitional zone (in microns)	Optical path length in radial zone (in microns)	Total thickness of the cartilage model (in microns)
0	0	100	500	400	1000
20	14.14	103.2	516.10	412.8	1032.2
40	27.33	113.0	565.0	452.0	1130.1
60	38.2	128.4	642.2	513.7	1284.4

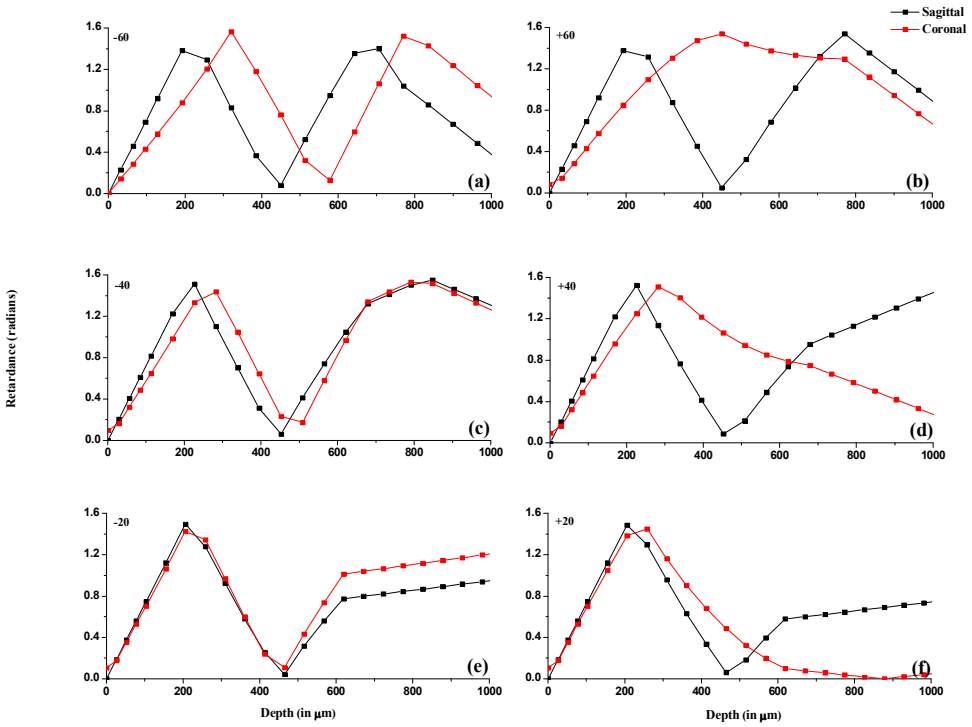

Figure 2.22: (a)-(f) Phase retardance profile obtained for normal incidence over two orthogonal planes simulated using EJMC articular cartilage model.

2. 9: Noise model in EJMC for TD-PS-OCT data

As per the single scattering model for OCT (Thrane *et al.*, 2000) and taking into account the Beer's law, OCT signal measured (round trip propagation) as field amplitude could be given as:

$$A(z) \propto \sqrt{\exp(-2\mu_t z)} \tag{2.63}$$

where, μ_t is the attenuation coefficient.

The major causes of the systematic error that arise in tissue birefringence measurements is attributed to the OCT signal being close to noise floor of the system or small values of birefringence in the tissue imaged. The backscattered light signal from an OCT system goes

on decreasing along the depth of the tissue finally reaching the noise floor. In TD-PS-OCT detection, at the start of the tissue interface, there is considerable signal in one of the detection channel and the other channel being dominated by system noise. This changes along the depth of the tissue at certain point when the two detection channels are dominated by system noise alone which results in the phase retardance value of $\frac{\pi}{4}$ after a certain depth of the tissue. Thus, systematic error occurring phase retardance measurements could be mainly attributed to the background noise in the OCT system that defines the minimum detectable signal in either of the detectors in the PS-OCT scheme (Schoenenberger *et al.*, 1998). Thus, the obtained depth dependent amplitudes in Equation 2.61 are modified with the inclusion of the signal attenuation equation and a noise bias term σ^2 as below:

$$A_V(z) = \sqrt{\sin^2\left(\frac{2\pi}{\lambda}\Delta nz\right)\exp(-2\mu_t z) + \sigma^2} \tag{2.64}$$

$$A_H(z) = \sqrt{\cos^2\left(\frac{2\pi}{\lambda}\Delta nz\right)\exp(-2\mu_t z) + \sigma^2} \tag{2.65}$$

This modifies the calculated retardance profiles (Equation 2.62) from the noise included EJMC simulation given as follows:

$$\delta_{EJMCnoise}(z) = \tan^{-1}\left(\frac{\sqrt{\left[\sin^2\left(\frac{2\pi}{\lambda}\Delta nz\right)\exp(-2\mu_t z) + \sigma^2\right]}}{\sqrt{\left[co\,s^2\left(\frac{2\pi}{\lambda}\Delta nz\right)\exp(-2\mu_t z) + \sigma^2\right]}}\right) \tag{2.66}$$

With the inclusion of the noise model in the EJMC articular cartilage model, a manual fit was attempted at trying to fit the depth dependent retardance profiles obtained from multi-angle

PS-OCT measurements of TD-PS-OCT. However, before proceeding onto the manual fit of multi-layered articular cartilage using EJMC, manual fit of multi-angle PS-OCT depth dependent retardance value is obtained for unilayered tendon tissue which is discussed in the following section in greater details.

2.10: Manual fit of EJMC and TD-PS-OCT data:

EJMC model has been applied to PS-OCT data obtained for single layered orientation of collagen as seen in tendon tissue which has a unidirectional orientation of collagen fibres. Also, the ordered nature of the collagen fibres (Type I) gives a simple method to calculate the true birefringence value of the tissue based on the band spacing obtained for normal incidence (uniform band spacing over depth). From single layered structure EJMC model has been applied to a complicated layered model of collagen fibre (Type II) in articular cartilage EJMC model of articular cartilage as described in Section 2.8.

2.10.1: Equine tendon

Multi-angle measurements obtained for an equine tendon sample as described in Section 2.7 of Chapter 2 (Figure 2.14) is input into an EJMC model of single layered birefringent tissue. The parameters upon which this simple unilayered model is based is the true birefringence value Δn, polar and azimuthal angle θ_c and ϕ_c which is constant over the depth of the tissue and the noise model that inputs the attenuation coefficient μ_t and the noise bias term σ^2. The true birefringence Δn of equine tendon sample is obtained from the band spacing calculated from the normal incidence depth dependent retardance profile. Band spacing obtained from normal incidence phase retardance profile (Figure 2.23(c)), as calculated from the Equation 1.18 in Section 1.4.4 in Chapter 1, is 96μm which gives $\Delta n = 6.8 \times 10^{-3}$, which is input as the

simulation parameter in EJMC model. The polar and azimuthal angles are respectively 90^o and 0^o for the entire depth of the tissue. The refractive index is assumed to be 1.4. With the inclusion of noise model given in Section 2.9., and an assumed values for attenuation factor $\mu_t = 0.002\mu m^{-1}$ as well as the noise bias term, $\sigma^2 = 0.05$, the manual fit for the simulated EJMC retardance profiles and the obtained PS-OCT data for equine tendon is shown in Figure 2.23(a)-(e) . As seen from Figure 2.14, the signal obtained from plane 2 ($y-z$ plane) is very close to the noise floor for oblique incidence of $\pm 40^o$. Therefore, EJMC model fit is carried out for 5 measurements which include the normal incidence data, Plane 1 $\pm 40^o$ and Plane 2 $\pm 20^o$. As could be seen from Figure 2.23(a)-(b), over oblique incidence in one of the plane of imaging, the obtained back-scattered signal from OCT tends to reach the noise floor very soon. This is attributed to the inherent nature of packing of the Type I collagen fibres and the longer diameter fibrils involved in the tissue. However, this type of behavior of reduced backscattered signal from one plane of imaging is not seen in articular cartilage which is mainly made of Type II collagen fibres of finer fibrils. This is discussed in much greater detail in Chapter 3 where a comparative study of the angle-resolved scattering profiles obtained from bovine tendon and articular cartilage is given. The obtained manual fit of EJMC simulated phase retardance profiles and PS-OCT multi-angle measurement details is quite straightforward with a simple unilayer model for tendon sample and the band spacing data of the experimental and simulated profiles tend to agree well based on the assumed values input to the parameters in EJMC model.

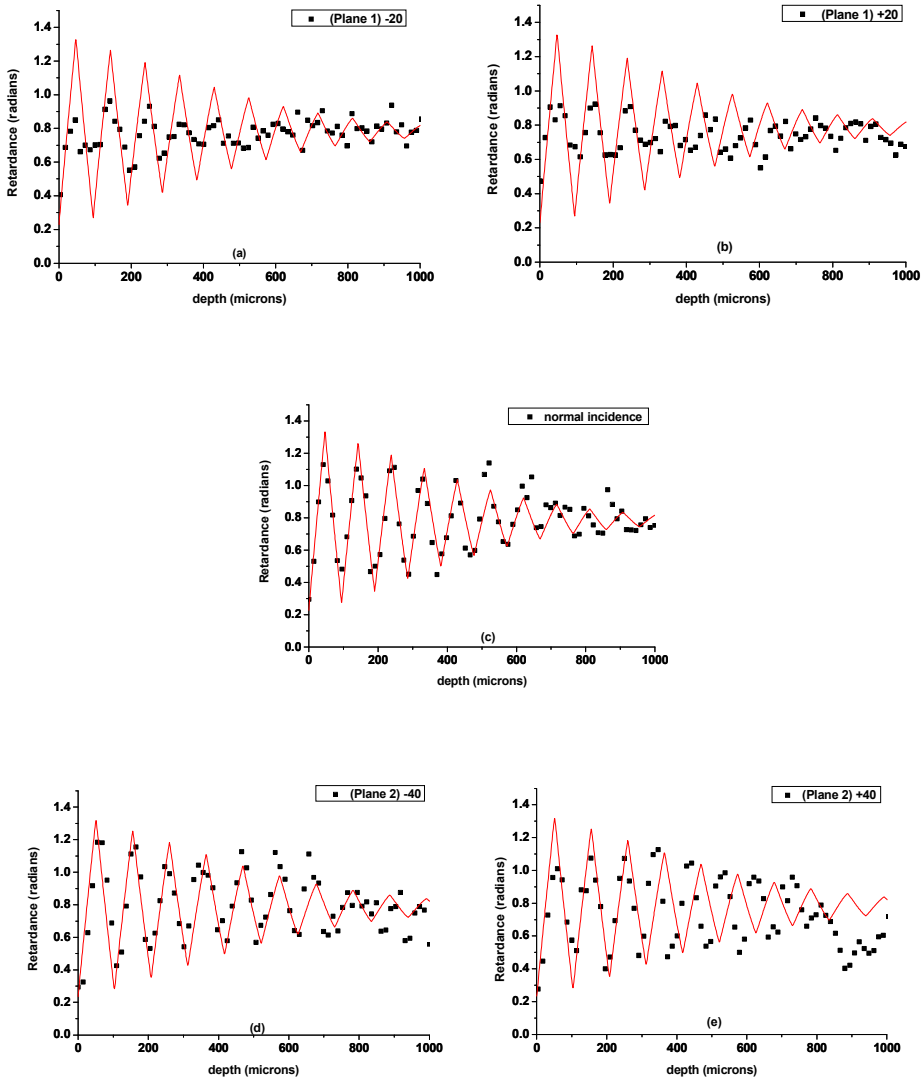

Figure 2.23 (a) - (e): Manual fit obtained between the phase retardance profiles obtained using EJMC and multi-angle measurements of PS-OCT data of $\pm 20^{o}$ in Plane 1 and $\pm 40^{o}$ in Plane 2 over two orthogonal planes, obtained by putting in the values of input parameters in unilayered EJMC model to obtain a visually good curve fit of data over 5 measurements simultaneously

2.10.2: Bovine articular cartilage

Figure 2.24 shows the bovine articular cartilage sample extracted from the fetlock joint of the hindlimb of the animal, with the red circle marking the site of imaging to carry out the comparative study of retardance data obtained from EJMC simulation and that obtained experimentally. As the knowledge of azimuth angle is unknown *a priori*, it is proceeded on with the assumption based on the results obtained from the split line experiments carried out previously which point out that the azimuthal orientation of the collagen fibres in superficial layer need not be parallel to the sagittal ridge but follow a typical trend that might have to do with the biomechanical function of the articular cartilage which varies based on the location (Below *et al.*, 2002; Bottcher *et al.*, 2009; Ugryumova*, et al.*, 2006). In Figure 2.24, the black line on the surface of the tissue represents a typical azimuthal orientation that is assumed to be the arrangement of collagen fibres along the surface at that site.

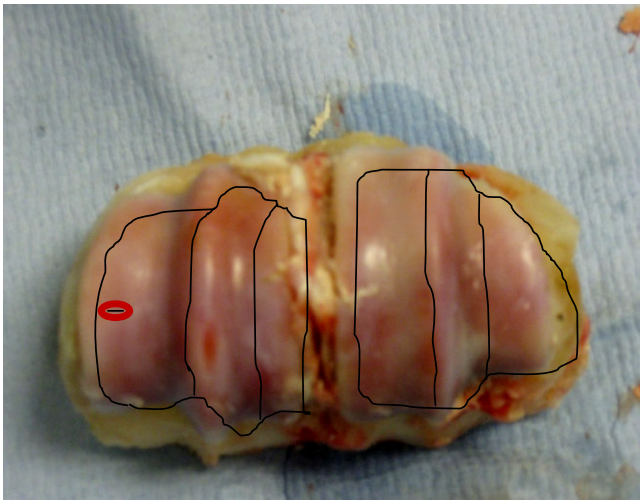

Figure 2.24: The bovine articular cartilage sample shown with the site imaged shown in red circle. The black line represent tentative azimuthal angle orientation of surface collagen fibre orientation.

As discussed in Section 2.8, the model is based on the following free parameters: thickness of the zonal layers of the articular cartilage that determines the polar angle orientation at

different depth of the tissue, polar and azimuthal orientation information of collagen fibres along the depth of the tissue, true birefringence value for an assumed ordinary refractive index of the tissue sample, the noise model which assumes a attenuation coefficient and noise bias factor. With this model, we proceeded on with obtaining retardance profiles for normal incidence and for oblique incidences of $\pm 60^{o}$ with respect to the normal. The manual fit was carried out by trying to visually curve fit all the 5 retardance profiles of the PS-OCT experimental data and the EJMC simulation data. The EJMC model details are as mentioned earlier (Section 2.8) with histological zone thickness assumed as follows: thickness of superficial zone, 100μm, transitional as 500μm and radial as 400μm for overall articular cartilage thickness assumed as 1mm. A value of true birefringence $\Delta n = 2.2 \times 10^{-3}$ seems to produce a closer fit of the data than other values. The azimuthal angle was chosen close to zero and the values of the polar angle, θ_c input along the depth of the model as tabulated in Table 2.3. The obtained manual fit for the multi-angle measurements for the bovine articular cartilage PS-OCT measurements at the chosen site of the tissue is shown in Figure 2.25(a)-(e). The main aim behind carrying out this study was to develop a non-invasive technique to extract the 3D optic axis information from articular cartilage with a potential towards use in clinical applications. With respect to the closeness of the manual fit obtained, an automated fitting procedure with nonlinear optimization algorithms were developed using customised optimisation functions available in optimtool toolbox of Matlab ™. Also, as seen from Figure 2.25(c), the manual fit obtained for normal incidence retardance profiles does seem to be not quite as good a fit for profiles at oblique incidence. Automating the optimisation process with respect to the free parameters that determine the nature of the banding of retardance profiles over 5 different measurements including the normal incidence and $\pm 60^{o}$ over two orthogonal

planes of imaging provides a complete 3D extraction of collagen fibre orientation. This is discussed in Section 2.11.

Table 2.3: Tabulated values for the values of polar angle θ_c input into layered EJMC articular cartilage model based on histological zones in the tissue used for manual fitting of PS-OCT data.

Histological zones	Individual layers	Polar angle
Superficial	1	90
	3	90
Transitional	5	85
	7	60
	9	45
	11	35
	13	28
	15	15
Radial	17	0
	19	0
	21	0

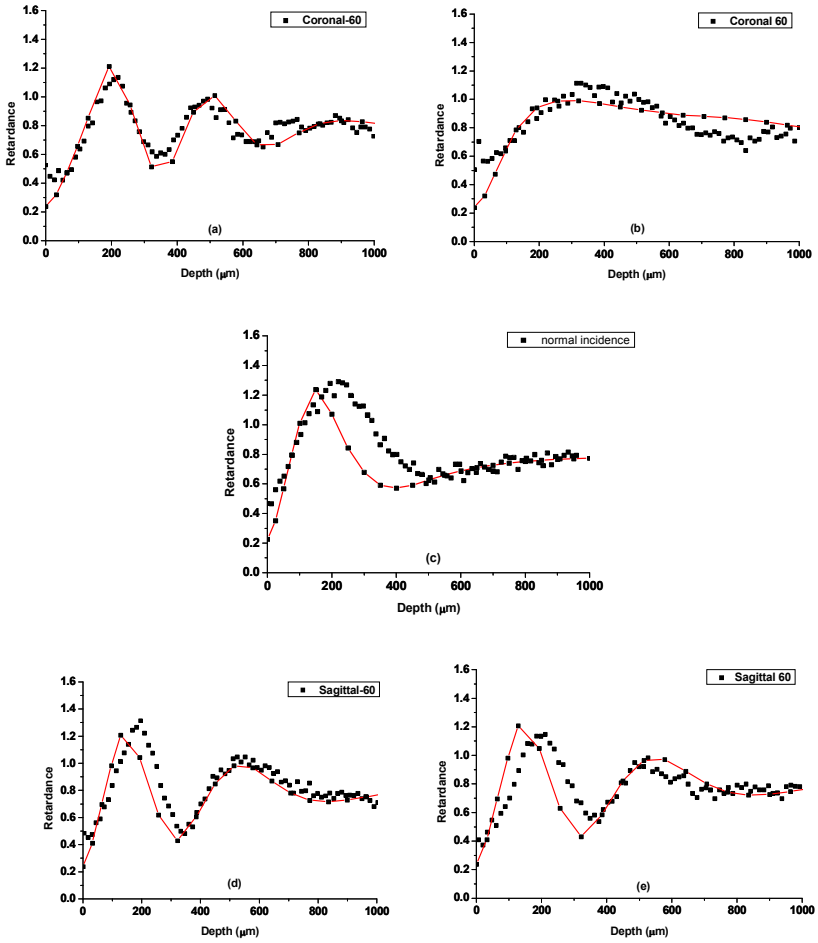

Figure 2.25 (a)-(e): Depth-dependent retardance profiles obtained from PS-OCT measurements (dots) compared with those obtained from EJMC simulation results (line + dots) over multiple angles of illumination in sagittal and coronal planes of the bovine cartilage sample.

2.11: Optimisation algorithms for fitting EJMC data

To extend the usefulness of EJMC model towards extraction of 3D optic axis information of articular cartilage along the depth of the tissue, an automated fitting procedure was implemented using optimization algorithms available in the optimtool toolbox of Matlab^{TM}. The model then formulated on the basis of following free parameters which are

a) thickness of the superficial zone, $t_{\sup}$

b) thickness of the transitional zone, t_{trans}

c) the polar angle orientation θ_c of the collagen fibres along the transitional zone as it arches from superficial zone to being radial into the radial zone. This is being modelled as a quadratic profile with coefficients $'a','b'\&'c'$ describing the nature of the arching away of the collagen fibres in the transitional zone

$$\theta_{c\_trans}(z) = a.z^2 + b.z + c \tag{2.67}$$

where, z represents the depth into the transitional zone

d) the azimuthal orientation, ϕ_c of the optic axis along the depth of the tissue

e) the true birefringence value, Δn assumed to be constant over depth of the tissue

f) the noise model that is defined by an attenuation coefficient, μ_t and noise bias term, σ.

Based on these parameters, curve fitting is obtained for the retardance profiles of experimental data and EJMC by trying to minimize the least square objective function given by:

$$\chi^2 = \sum_{j=1}^{5}\sum_{i=1}^{n}\left[\delta_{j,\text{measured}}(z_i) - \delta_{j,\text{modelled}}(z_i)\right]^2 \tag{2.68}$$

Where n denotes the number of axial measurement points, and i labels the incident k-vectors. The precision of the fitted parameters is further analyzed by carrying out 'Bootstrap Monte Carlo' procedure. Bootstrapping technique is widely used in statistics to estimate standard errors in sampling distribution procedure (Manly, 2001). Bootstrapping technique is used along with Monte Carlo method to generate an ensemble of 100 random data sets based on the mean experimental data and estimated standard deviations. The mean of the experimental

data is obtained for averages over 50 A-scans and standard deviations are obtained for randomly chosen subsets of data averaged over 10 A-scans from the original dataset. Using these dataset the statistics of the fitted parameters are obtained. Two different approaches of nonlinear optimization were used for this study, unconstrained optimizer based on direct search simplex Nelder Mead algorithm (Olsson & Nelson, 1975) and a constrained optimizer based on interior reflective Newton method (Thomas & Li, 1994) to further study how choice of optimisation algorithm affects the outcome of the study. The basic aim behind use of different optimisation algorithm is to see how well the EJMC modelling could be formulated and put into an optimiser to obtain global minima for the objective function that outputs the values of the parameters in the EJMC model. The type of mathematical function used in the optimiser, formulation of the problem to be optimised, the initial input conditions that drives the optimiser, etc are some of the factors that influence the output generated by the optimiser (Venkataraman, 2009). The results obtained with two different choices of optimiser functions are reported in Section 2.11.1 and Section 2.11.2, respectively.

2.11.1: 'fminsearch' algorithm

'fminsearch' in optimtool toolbox of Matlab^{TM} is based on a heuristic approach to minimising an objective function based on Nelder-Mead unconstrained optimisation approach (Lagarias *et al.*, 1998).

Table 2.4: List of all the parameters used in the 'fminsearch' optimizer for obtaining a good fit of the depth-dependent retardance profiles obtained from angle-resolved PS-OCT imaging and those obtained from EJMC simulation. This optimization would thus yield the depth-dependent 3D structural information data from the articular cartilage as shown in the Output column of the table. Also, given are the values of the two different input conditions given to the optimizer and the corresponding output parameters obtained.

Parameters	Input condition1	Output1 obtained	Input condition2	Output2 obtained
Thickness of superficial layer (in μm)	50	83 ± 27	100	139 ± 97
Thickness of transitional layer (in μm)	600	595 ± 360	400	382 ± 213
Azimuthal angle (ϕ_c in deg.)	-25	2.2 ± 8.2	-10	2.4 ± 19.1
Coefficient 'a'	140×10^{-6}	$(115 \pm 62) \times 10^{-6}$	140×10^{-6}	$(254 \pm 168) \times 10^{-6}$
Coefficient 'b'	-21.77×10^{-2}	$(-19.25 \pm 10.46) \times 10^{-2}$	-21.77×10^{-2}	$(-23.38 \pm 16.34) \times 10^{-2}$
True birefringence Δn	1.5×10^{-3}	$(2.18 \pm 0.067) \times 10^{-3}$	1.7×10^{-3}	$(2.09 \pm 0.079) \times 10^{-3}$
Attenuation coefficient, μ_t	4.0×10^{-3}	$(2.5 \pm 0.05) \times 10^{-3}$	4.0×10^{-3}	$(5.5 \pm 4) \times 10^{-3}$
Noise bias, σ	6.0×10^{-2}	$(8.3 \pm 4.1) \times 10^{-2}$	6.0×10^{-2}	$(4.06 \pm 4.03) \times 10^{-2}$

The algorithm approximates a local minimum of a problem, by minimising the objective function. In this study, two different input conditions were separately input the optimiser and the ouput was obtained by averaging the output obtained by running the optimizer through 100 random generated dataset derived from the averaged A-scan of PS-OCT using bootstrap Monte Carlo method (Table 2.4). However, in this study, coefficient *'c'* in the quadratic profile of θ_c is not a variable input into the optimizer, but is input as a constant of value 90 which describes θ_c at the onset of the transitional zone. A noticeable improvement in the fit is produced by the optimizer although significant differences still persist and indicate that the

model is still in need of further refinement (Figure 2.25(a)-(e) & Figure 2.26(a)-(e)). However, as can be seen from Figure 2.27(a)-(e), the choice of input parameters greatly determines the local minima found by the optimiser which affects the goodness of fit obtained.

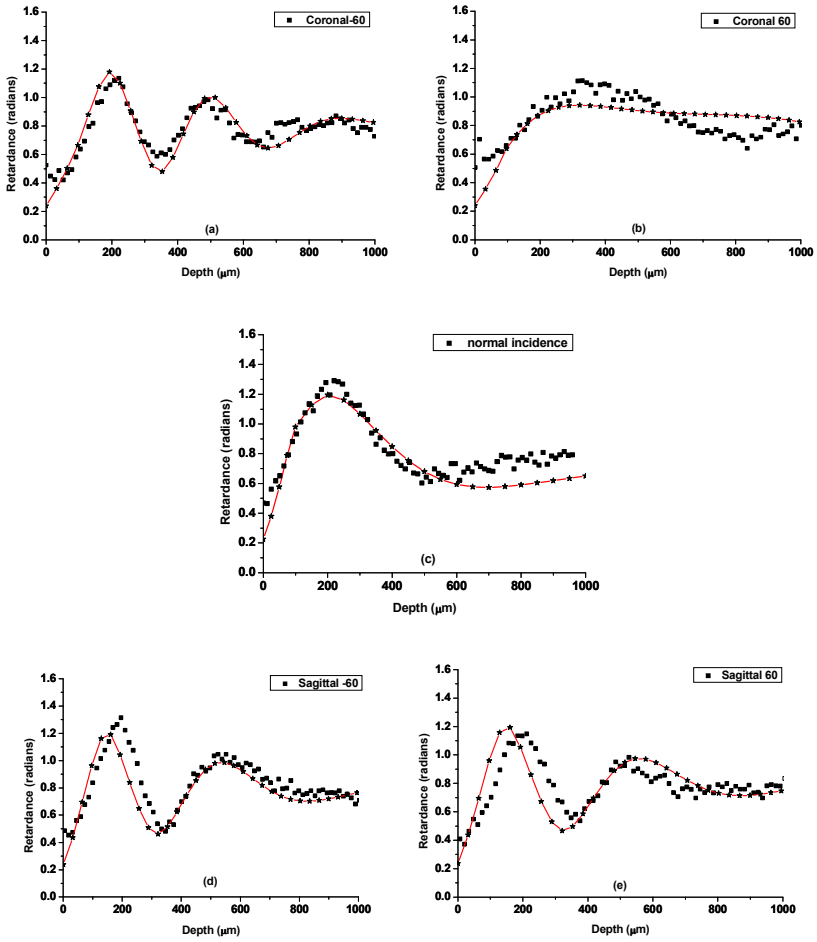

Figure 2.26 (a)-(e): Depth-dependent retardance profiles obtained from PS-OCT measurements (dots) compared with those obtained from EJMC simulation results (line + star) over multiple angles of illumination in sagittal and coronal planes of the bovine cartilage sample output parameters obtained from 'fminsearch' optimizer and bootstrap Monte Carlo method using input condition 1 as shown in Table 2.4 .

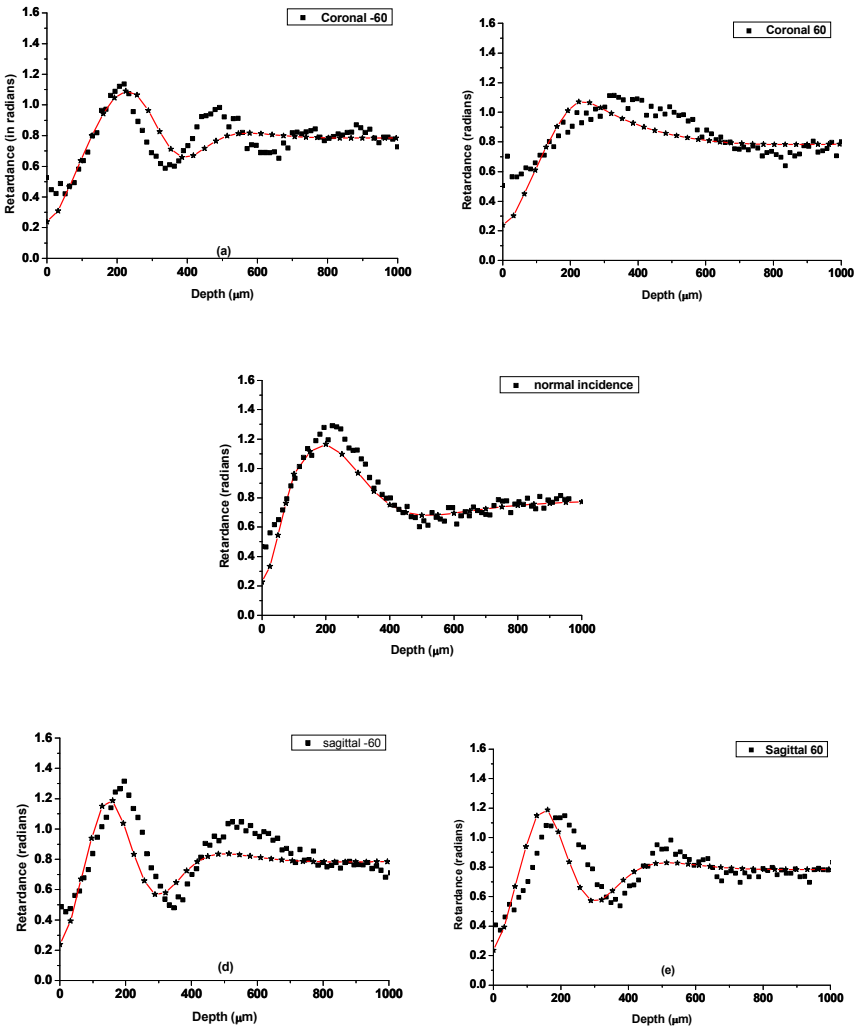

Figure 2.27(a)-(e): Depth-dependent retardance profiles obtained from PS-OCT measurements (dots) compared with those obtained from EJMC simulation results (line + star) over multiple angles of illumination in sagittal and coronal planes of the bovine cartilage sample based on output parameters obtained from 'fminsearch' optimizer and bootstrap Monte Carlo method using input condition 2 as shown in Table 2.4 .

2.11.2: 'fmincon' algorithm

'fmincon' function used is a constrained nonlinear optimisation algorithm based on interior point Newton method (Byrd *et al.*, 2000; Byrd *et al.*, 1999; Waltz *et al.*, 2006). Table 2.5

tabulates the input upper and lower bound given to the optimiser with the initial input conditions along with the output obtained from averaging the results of 100 random data-sets using bootstrap Monte Carlo method. Figure 2.28 (a)-(e) presents the curve fit obtained from EJMC simulated retardance profiles using the averaged output from the optimiser.

Table 2.5: List of all the parameters used in the 'fmincon' optimizer for obtaining a good fit of the depth-dependent retardance profiles obtained from angle-resolved PS-OCT imaging and those obtained from EJMC simulation. Given are the values of the input conditions and boundary conditions for the values of parameters as given to the optimizer and the corresponding output parameters obtained. Output is obtained by averaging the output obtained by running the optimizer through 100 random generated dataset derived from the averaged A-scan of PS-OCT using bootstrap Monte Carlo method

Parameters	Input condition	Lower bound	Upper bound	Output obtained
Thickness of superficial layer (in μm)	100	50	200	125 ± 0.3
Thickness of transitional layer (in μm)	300	100	800	450 ± 3.6
Azimuthal angle (ϕ_c in deg.)	45	-90	90	7 ± 7.3
Coefficient 'a'	130×10^{-6}	100×10^{-6}	180×10^{-6}	$(140 \pm 0.0000027) \times 10^{-6}$
Coefficient 'b'	-20.56×10^{-2}	-23.56×10^{-2}	-19.99×10^{-2}	$(-21.77 \pm 0.0032) \times 10^{-2}$
Coefficient 'c'	96	85	95	90 ± 0.024
True birefringence Δn	1.5×10^{-3}	0.5×10^{-3}	4×10^{-3}	$(2.06 \pm 0.097) \times 10^{-3}$
Attenuation coefficient, μ_t	4.0×10^{-3}	4.0×10^{-3}	7.0×10^{-3}	$(4.1 \pm 0.42) \times 10^{-3}$
Noise bias, σ	6.0×10^{-2}	4.0×10^{-2}	8.0×10^{-2}	$(4.6 \pm 0.59) \times 10^{-2}$

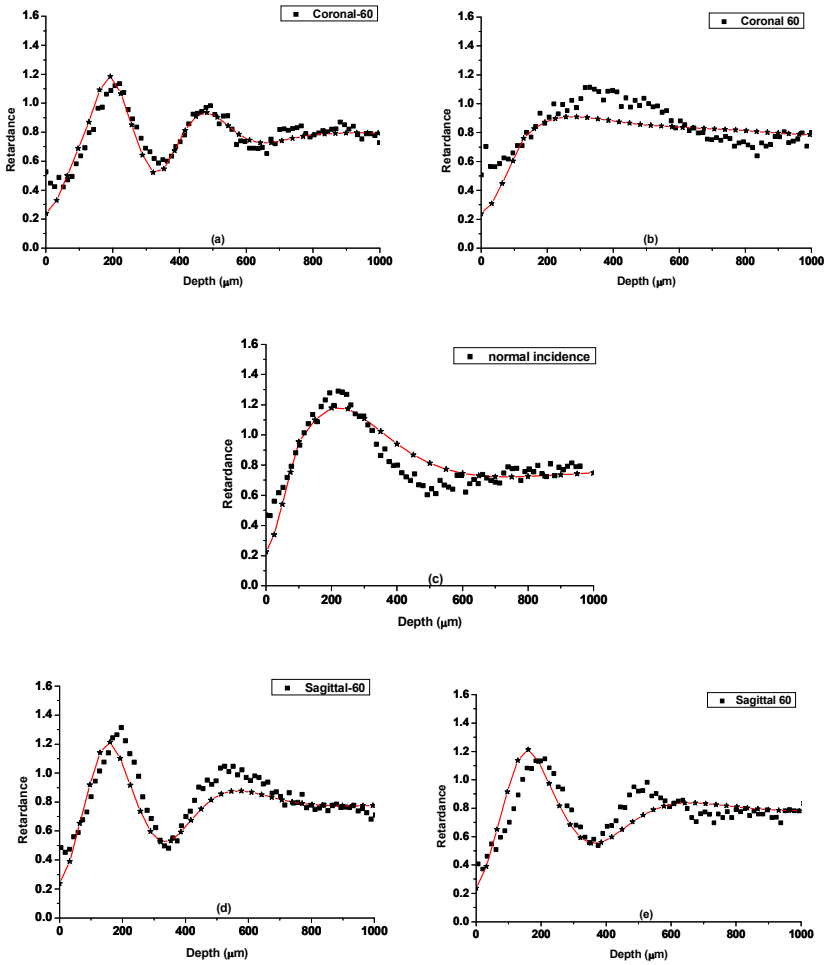

Figure2.28(a)-(e): Depth-dependent retardance profiles obtained from PS-OCT measurements (dots) compared with those obtained from EJMC simulation results (line + star) over multiple angles of illumination in sagittal and coronal planes of the bovine cartilage sample based on parameters obtained from 'fmincon' optimizer and bootstrap Monte Carlo method.

An interesting point to note here is that the optimiser always outputs the midpoint value of upper and lower bound values for some of the parameters in the model, which are : the coefficient 'a', 'b', 'c' of the polar angle profile in transitional zone and the thickness of superficial and the transitional layer, for any set of input parameter chosen. This requires further investigation into the problem formulation and how this affects the numerical stability

of the optimiser. The values of least square functions (discrepancy in the modelled data) as obtained from Equation 2.68 for the different fitting technique implemented so far in this thesis from Figure 2.25 - 2.28 are tabulated in Table 2.6.

Table 2.6: Goodness of fit measures obtained for the EJMC model from Figure 2.25 to Figure 2.28

Type of curve-fitting	Least-squares
Manual fit (Figure 2.25)	3.67
'fminsearch' optimiser input condition 1 (Figure 2.26)	2.68
'fminsearch' optimiser input condition 2 (Figure 2.27)	2.98
'fmincon' optimiser (Figure 2.28)	2.35

2.12: Fitting EJMC data to experimental CPM-SS-PS-OCT

The main aim behind the investigation of EJMC approach towards understanding the structural orientation information in PS-OCT images was to use a fibre based PS-OCT towards non-invasive study of *in-vivo* samples. Although, the study presented here using TD-PS-OCT and CPM-SS-PS-OCT were ex-*vivo,* the idea that useful structural orientation could be extracted from angle-resolved PS-OCT measurements could be further investigated using a fibre-based or endoscopy based PS-OCT system (Pierce *et al.*, 2005) for *in-vivo* studies. With the CPM-SS-PS-OCT used for this study developed by *Lu et al.* as described in Section 2.4, multi-angle PS-OCT measurements were carried out on another sample of bovine articular sample but along the similar site as imaged using TD-PS-OCT system (Lu*, et al.*, 2011b). The total depth achieved in the tissue is around 750μm, with the useful depth information of around 500μm from the tissue surface as shown for the mutli-angle measurements using the system in Figure 2.28(a)-(e).

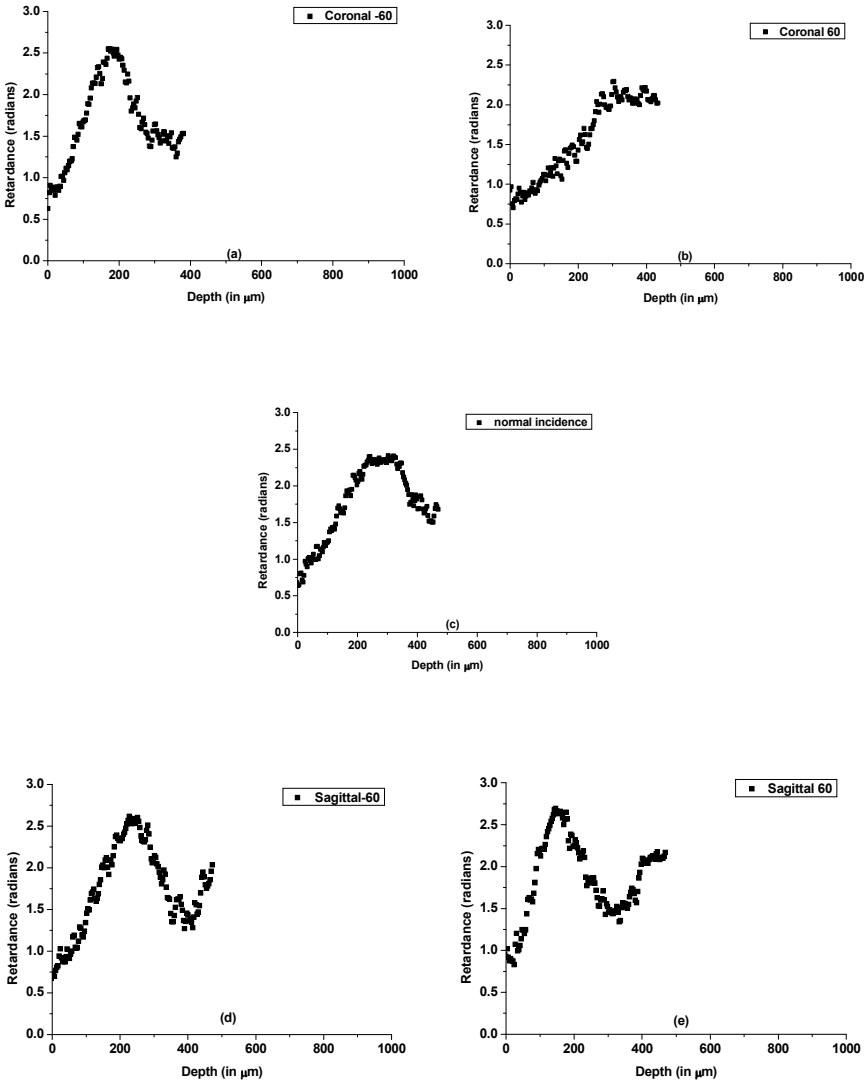

Figure 2.29(a)-(e): Depth-dependent retardance profiles obtained from PS-OCT measurements (dots) obtained from multi-angle measurements using CPM-SS-PS-OCT system using 20MS/s 14-bit digitizer that gives limited depth information over the tissue under study.

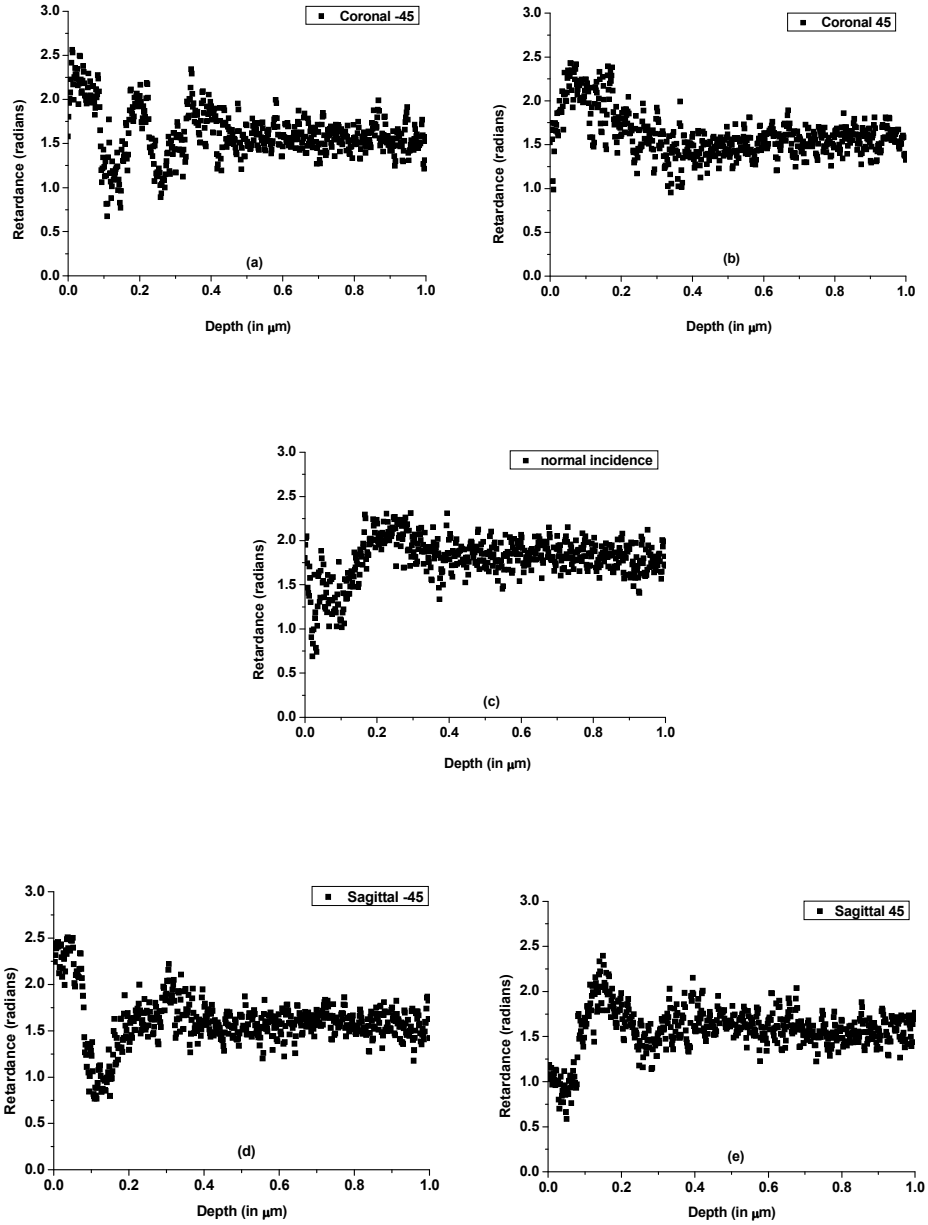

Figure 2.30(a)-(e): Depth-dependent retardance profiles obtained from PS-OCT measurements (dots) obtained from multi-angle measurements using CPM-SS-PS-OCT system using 100MS/s 8-bit digitizer that extends the depth penetration of light beam into the tissue but unfortunately boosts the noise.

The measurements were carried out using 20MS/s 14-bit digitiser (M2i.4022, Spectrum GmbH, Germany) at EOM modulation frequency of 6.67MHz, which is one-third the speed of data acquisition. As seen in Figure 2.29, the full 3D information over entire depth of the articular cartilage tissue till the radial zone is not obtained from this system. Therefore, putting these multi-angle measurement data into EJMC simulation optimiser would not yield the most appropriate fit parameters in order to obtain depth-dependent 3D optic-axis parameters. The banding patterns obtained are incomplete to provide a comprehensive picture of the optic axis correctly. Also, unlike the TD-PS-OCT theory, the retardance values are wrapped around the range $[0 \quad \pi]$. In order to carry out the similar EJMC fitting procedure using CPM-SS-PS-OCT as was carried out with multi-angle measurements using TD-PS-OCT, extending the scan depth using high speed digitiser was investigated. This was achieved using 100MS/s (M2i.2031, Spectrum GmbH, Germany) with a 8-bit digitiser. The multi-angle measurements obtained on bovine articular cartilage sample using this set up is shown in Figure 2.30 (a)-(e). Although banding patterns within the noisy data could be revealed, a proper understanding of the noise introduced in the system with the introduction of high speed digitiser in similar approach reported by Makita *et al.* has to be carried out in order to understand the information provided by phase retardance images (Makita *et al.*, 2010). This requires further investigation and detailed study.

2.13: Conclusions

In this chapter, the main stress has been on the application of PS-OCT imaging towards understanding the microstructure of articular cartilage. This has been carried out using two different PS-OCT systems: first generation based TD-PS-OCT and the recent version of Fourier domain based CPM-SS-PS-OCT. The investigation was started with optic axis

validation technique for the two systems using Soleil-Babinet Compensator for TD-PS-OCT and three-quarter waveplate and tendon sample for CPM-SS-PS-OCT based on burst trigger mode global phase normalisation phase calibration method employed in the latter to remove phase fluctuation artefacts. A detailed investigation was shown for a particular site of bovine articular cartilage using multi-angle measurements based on theoretical formulation using EJMC using TD-PS-OCT. This was carried out initially using a manual fit with the inclusion of a noise model dealing with the background noise effecting phase retardance measurements, followed by development of an articular cartilage model input to nonlinear optimisation algorithm that outputs the fitted parameters that allow us to obtain full 3D optic axis information of the collagen network in multi-layered anisotropic articular cartilage tissue. This study has investigated the applicability of EJMC approach towards understanding the anisotropic properties of biological tissues with weak birefringence. Although, this model has been based on certain assumption, without *a-priori* knowledge of the values of the parameters used, a detailed investigation with a validation tool would further substantiate this approach.

Furthermore, different nonlinear optimisation algorithms have been investigated: simplex based 'fminsearch' function and constrained nonlinear optimisation algorithm based on interior point Newton method. Although, no consensus has been made on the optimal choice of the optimisation algorithm in this study, the results obtained with these two choices have opened up further scope of study towards optimal formulation of EJMC curve fitting problem for mutli-angle PS-OCT measurements.

Although, formulations based on EJMC its applicability to study articular cartilage microstrucutre has been shown previously theoretically, this is for the first time to the best of

our knowledge, a comparative study based on experimental and theoretical data of articular cartilage microstructure has been investigated. However, the analysis using CPM-SS-PS-OCT has not been fully investigated and a detailed description of noise analysis in the high-speed digitiser implementation of CPM-SS-PS-OCT has to be carried out.

2.14: Further scope of study

In broader perspective this study could be extended as listed out below:

1. A detailed study of the noise affecting the phase measurements in a fibre based CPM-SS-PS-OCT could be carried out to be included in an EJMC model to precisely simulate the multi-angle depth dependent retardance data to study the 3D structural orientation of the articular cartilage. This accompanied with the advantages of a fibre based system over a time domain system could be used for *in-vivo* measurements on biological samples.

2. The results obtained from EJMC model has to be validated against a standard technique that would correlate the 3D structural orientation for the sample. The validation technique could be the gold standard polarized light microscopy or diffusion tensor MRI. However the unique capabilities of PS-OCT make it difficult to identify any one alternative technique against which it could be compared.

3. This model is flexible enough to incorporate a range of different birefringent biological samples ranging from a simpler structural organization in tendon to a very complex 3D structural architecture seen in articular cartilage. Therefore, the potential and robustness of this technique to study the topographical variations of the 3D orientation of the collagen fibre as well as the thickness of the histological zones involved could be verified with the implementation of an optimal optimisation algorithm.

4. The experiment carried out using EJMC and multi-angle PS-OCT measurements carried out on normal looking healthy bovine articular cartilage sample could be extended to study the applicability of the model to other species of animals and as well as the applicability of this model towards understanding the birefringence changes that could occur during different phases of osteoarthritis in articular cartilage.

These areas of further study could be of great interest to investigate further towards use of PS-OCT towards understanding the microstructure of articular cartilage non-invasively and with potential diagnostic applications.

2.15: References

Below, S., Arnoczky, S. P., Dodds, J., Kooima, C., & Walter, N. (2002). The split-line pattern of the distal femur: A consideration in the orientation of autologous cartilage grafts. *Arthroscopy, 18*(6), 613-617.

Bottcher, P., Zeissler, M., Maierl, J., Grevel, V., & Oechtering, G. (2009). Mapping of split-line pattern and cartilage thickness of selected donor and recipient sites for autologous osteochondral transplantation in the canine stifle joint. *Vet Surg, 38*(6), 696-704.

Byrd, R. H., Gilbert, J. C., & Nocedal, J. (2000). A trust region method based on interior point techniques for nonlinear programming. *Mathematical Programming, 89*(1), 149-185.

Byrd, R. H., Hribar, M. E., & Nocedal, J. (1999). An interior point algorithm for large-scale nonlinear programming. *Siam Journal on Optimization, 9*(4), 877-900.

Clark, J. M., & Simonian, P. T. (1997). Scanning electron microscopy of “fibrillated” and “malacic” human articular cartilage: technical considerations. *Microscopy Research and Technique, 37*(4), 299-313.

de Boer, J. F., Milner, T. E., & Nelson, J. S. (1999). Determination of the depth-resolved Stokes parameters of light backscattered from turbid media by use of polarization-sensitive optical coherence tomography. *Optics Letters, 24*(5), 300-302.

Everett, M. J., Schoenenberger, K., Colston, B. W., & Da Silva, L. B. (1998). Birefringence characterization of biological tissue by use of optical coherence tomography. *Optics Letters, 23*(3), 228-230.

Fanjul-Vélez, F., & Arce-Diego, J. L. (2010). Polarimetry of birefringent biological tissues with arbitrary fibril orientation and variable incidence angle. *Optics Letters, 35*(8), 1163-1165.

Fanjul-Velez, F., Pircher, M., Baumann, B., Gotzinger, E., Hitzenberger, C. K., & Arce-Diego, J. L. (2010). Polarimetric analysis of the human cornea measured by polarization-sensitive optical coherence tomography. *Journal of Biomedical Optics, 15*(5), 056004-056010.

Gangnus, S., Matcher, S. J., & Meglinsky, I. V. (2004). Monte Carlo modeling of polarized light propagation in a biological tissue. *Laser Physics, 14*(6), 886-891.

Greenwood, P. D. L., Childs, D. T. D., Kennedy, K., Groom, K. M., Hugues, M., Hopkinson, M. (2010). Quantum Dot Superluminescent Diodes for Optical Coherence Tomography: Device Engineering. *Ieee Journal of Selected Topics in Quantum Electronics, 16*(4), 1015-1022.

Gu, C., & Yeh, P. (1993). Extended Jones Matrix-Method .2. *Journal of the Optical Society of America A, 10*(5), 966-973.

Hitzenberger, C., Goetzinger, E., Sticker, M., Pircher, M., & Fercher, A. (2001). Measurement and imaging of birefringence and optic axis orientation by phase

resolved polarization sensitive optical coherence tomography. *Optics Express, 9*(13), 780-790.

Huang, Y.-P., Saarakkala, S., Toyras, J., Wang, L. K., Jurvelin, J. S., & Zheng, Y. P. (2011). Effects of optical beam angle on quantitative optical coherence tomography (OCT) in normal and surface degenerated bovine articular cartilage. *Physics in Medicine and Biology, 56*(2), 491.

Jacobs, J. (2011). *Polarisation sensitive optical coherence tomography; applications in tissue engineering.* Doctor of Philosophy, University of Sheffield, Sheffield.

Jasperson, S. N., & Schnatterly, S. E. (1969). An Improved Method for High Reflectivity Ellipsometry Based on a New Polarization Modulation Technique. *Review of Scientific Instruments, 40*(6), 761-767.

Jeffery, A., Blunn, G., Archer, C., & Bentley, G. (1991). Three-dimensional collagen architecture in bovine articular cartilage. *J Bone Joint Surg Br, 73-B*(5), 795-801.

Jiao, S., Todorovic, M., Stoica, G., & Wang, L. V. (2005). Fiber-based polarization-sensitive Mueller matrix optical coherence tomography with continuous source polarization modulation. *Appl Opt, 44*(26), 5463-5467.

Jiao, S., & Wang, L. V. (2002). Jones-matrix imaging of biological tissues with quadruple-channel optical coherence tomography. *J Biomed Opt, 7*(3), 350-358.

Jiao, S. L., & Wang, L. H. V. (2004). Comment on "optical-fiber-based Mueller optical coherence tomography" - Reply. *Optics Letters, 29*(24), 2875-2877.

Jones, R. C. (1941). A new calculus for the treatment of optical systems I. Description and discussion of the calculus. *Journal of the Optical Society of America, 31*(7), 488-493.

Lagarias, J. C., Reeds, J. A., Wright, M. H., & Wright, P. E. (1998). Convergence properties of the Nelder-Mead simplex method in low dimensions. *Siam Journal on Optimization, 9*(1), 112-147.

Lu, Z., Kasaragod, D. K., & Matcher, S. J. (2011a). Method to calibrate phase fluctuation in polarization-sensitive swept-source optical coherence tomography. *J Biomed Opt, 16*(7), 070502.

Lu, Z., Kasaragod, D. K., & Matcher, S. J. (2011b). Optic axis determination by fibre-based polarization-sensitive swept-source optical coherence tomography. *Phys Med Biol, 56*(4), 1105-1122.

Lu, Z., Kasaragod, D. K., & Matcher, S. J. (2012). Polarization-sensitive optical coherence tomography measurements with different phase modulation amplitude when using continuous polarization modulation. *Journal of Biomedical Optics, accepted for publication*.

Makita, S., Yamanari, M., & Yasuno, Y. (2010). Generalized Jones matrix optical coherence tomography: performance and local birefringence imaging. *Opt Express, 18*(2), 854-876.

Manly, B. (2001). *Randomization, bootstrap and Monte Carlo methods in biology* (Second ed.). Florida: Chapman & Hall/CRC.

Mow, V. C., & Ratcliffe, A. (1997). Structure and Function of Articular Cartilage and Meniscus. In V. C. Mow & W. C. Hayes (Eds.), *Basic Orthopaedic Biomechanics* (pp. 113-177): Lippincott-Raven New York.

Olsson, D. M., & Nelson, L. S. (1975). Nelder-Mead Simplex Procedure for Function Minimization. *Technometrics, 17*(1), 45-51.

Park, B. H., Pierce, M. C., Cense, B., & de Boer, J. F. (2004). Jones matrix analysis for a polarization-sensitive optical coherence tomography system using fiber-optic components. *Opt Lett, 29*(21), 2512-2514.

Park, B. H., Pierce, M. C., Cense, B., & de Boer, J. F. (2005). Optic axis determination accuracy for fiber-based polarization-sensitive optical coherence tomography. *Opt Lett, 30*(19), 2587-2589.

Pierce, M. C., Hyle Park, B., Cense, B., & de Boer, J. F. (2002). Simultaneous intensity, birefringence, and flow measurements with high-speed fiber-based optical coherence tomography. *Opt Lett, 27*(17), 1534-1536.

Pierce, M. C., Shishkov, M., Park, B. H., Nassif, N. A., Bouma, B. E., Tearney, G. J. (2005). Effects of sample arm motion in endoscopic polarization-sensitive optical coherence tomography. *Optics Express, 13*(15), 5739-5749.

Podoleanu, A. G. (2000). Unbalanced versus balanced operation in an optical coherence tomography system. *Appl Opt, 39*(1), 173-182.

Rieppo, J., Hyttinen, M. M., Halmesmaki, E., Ruotsalainen, H., Vasara, A., Kiviranta, I. (2009). Changes in spatial collagen content and collagen network architecture in porcine articular cartilage during growth and maturation. *Osteoarthritis Cartilage, 17*(4), 448-455.

Roth, J. E., Kozak, J. A., Yazdanfar, S., Rollins, A. M., & Izatt, J. A. (2001). Simplified method for polarization-sensitive optical coherence tomography. *Opt Lett, 26*(14), 1069-1071.

Schoenenberger, K., Colston, B. W., Maitland, D. J., Da Silva, L. B., & Everett, M. J. (1998). Mapping of birefringence and thermal damage in tissue by use of polarization-sensitive optical coherence tomography. *Applied Optics, 37*(25), 6026-6036.

Tearney, G. J., Bouma, B. E., & Fujimoto, J. G. (1997). High-speed phase- and group-delay scanning with a grating-based phase control delay line. *Opt Lett, 22*(23), 1811-1813.

Thomas, F. C., & Li, Y. Y. (1994). On the Convergence of Interior-Reflective Newton Methods for Nonlinear Minimization Subject to Bounds. *Mathematical Programming, 67*(2), 189-224.

Thrane, L., Yura, H. T., & Andersen, P. E. (2000). Analysis of optical coherence tomography systems based on the extended Huygens-Fresnel principle. *Journal of the Optical Society of America A, 17*(3), 484-490.

Tomlins, P. H., & Wang, R. K. (2005). Theory, developments and applications of optical coherence tomography. *Journal of Physics D: Applied Physics, 38*(15), 2519.

Ugryumova, N., Gangnus, S. V., & Matcher, S. J. (2006). Three-dimensional optic axis determination using variable-incidence-angle polarization-optical coherence tomography. *Opt. Lett., 31*(15), 2305-2307.

Vakoc, B., Yun, S., de Boer, J., Tearney, G., & Bouma, B. (2005). Phase-resolved optical frequency domain imaging. *Opt Express, 13*(14), 5483-5493.

Venkataraman, P. (2009). *Applied optimization with MATLAB programming* (Second ed.). New Jersey: John Wiley & Sons.

Waltz, R. A., Morales, J. L., Nocedal, J., & Orban, D. (2006). An interior algorithm for nonlinear optimization that combines line search and trust region steps. *Mathematical Programming, 107*(3), 391-408.

Wang, S. Z., Huang, Y. P., Wang, Q., & Zheng, Y. P. (2008). Assessment of depth and degeneration dependences of articular cartilage refractive index using optical coherence tomography in vitro. *Conf Proc IEEE Eng Med Biol Soc, 2008*, 4047-4050.

Wang, X., & Wang, L. V. (2002). Propagation of polarized light in birefringent turbid media: a Monte Carlo study. *J Biomed Opt, 7*(3), 279-290.

Yamamoto, K., Shishido, T., Masaoka, T., & Imakiire, A. (2005). Morphological studies on the ageing and osteoarthritis of the articular cartilage in C57 black mice. *J Orthop Surg (Hong Kong), 13*(1), 8-18.

Yamanari, M., Lim, Y., Makita, S., & Yasuno, Y. (2009). Visualization of phase retardation of deep posterior eye by polarization-sensitive swept-source optical coherence tomography with 1-microm probe. *Opt Express, 17*(15), 12385-12396.

Yamanari, M., Makita, S., & Yasuno, Y. (2008). Polarization-sensitive swept-source optical coherence tomography with continuous source polarization modulation. *Opt. Express, 16*(8), 5892-5906.

Yeh, P. (1982). Extended Jones Matrix-Method. *Journal of the Optical Society of America, 72*(4), 507-513.

CHAPTER 3

Angle-resolved Backscattering Studies on Bovine Cartilage and Tendon Samples

3.1. Summary:

An attempt has been made to understand the differences in the nature of the scatterers involved in the two different types of biological tissues involving collagen fibers of different kind; Tendon with Type I collagen fibers and articular cartilage with Type II collagen fibers, using optical coherence tomography based angle-resolved backscattering measurements. Multi-angle measurement technique in OCT as described in Section 2.7 of Chapter 2 has been implemented that gives the angle-resolved backscattering data for the two tissues. Light scattering is dependent on the size and distribution of the scatterers involved and consequently a greater angular anisotropy in the optical backscattering coefficient of bovine tendon is seen as compared to that in the articular cartilage. Simulation using the Rayleigh-Gans approximation, which is based on the first Born approximation, is carried out to understand the experimentally obtained data. In this chapter, Section 3.2 gives a brief introduction on the microstructure and composition of the two tissues, followed by a briefing on the motivation for carrying out this study. Section 3.3 describes the experimental and theoretical details of the scattering studies using OCT system. Rayleigh-Gans approximation is detailed in Section 3.4 with results and discussions in Section 3.5.

3.2. Introduction:

Connective tissues are the fibrous tissues that make up the support framework of tissues like tendon, cartilage, bone, blood, etc as well as organs. Tendons connect muscles to the bones and provide the necessary tensile strength with an ordered arrangement of collagen fibers. 80% of the weight is composed of collagen fibers and the rest being water and other macromolecules. Tendon is composed of Type I collagen fibers and also forms the most abundant collagen fiber found in the human body. A basic unit of collagen molecule is typical made of three chains of polypeptide wound into a right-handed helix structure. Tendon is dominantly made of Type I collagen fiber, which is composed of heterotrimer collagen molecules (tropocollagen) of two $\alpha 1(I)$ and one $\alpha 2(I)$ chains (Mow & Ratcliffe, 1997). Besides tendon, Type I collagen also forms a part of major composition in skins, ligaments, bones, etc. They also follow a hierarchical structure in organization of collagen molecule forming a tendon tissue (Kastelic *et al.*, 1978), with collagen aligned along the long axis of the tendon structure (Figure 3.1).

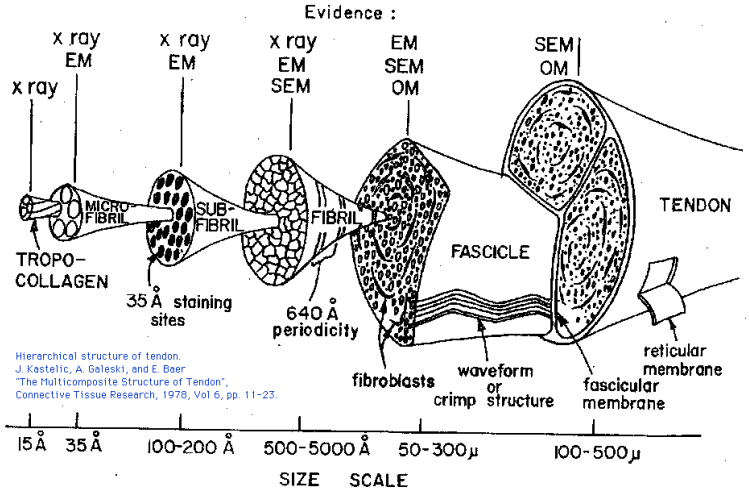

Figure 3.1: Hierarchical organization in tendon. Adapted from (Kastelic, *et al.,* 1978).

Each tropocollagen unit, which is 300nm long and 1.3nm wide aggregates into a semi-crystalline form, called fibrils, by an end-on arrangement with a periodicity of 67nm. These fibrils, which aggregate to a diameter of about 50-500nm, arrange themselves in a cylindrical array of planar crimped collagen fibrils, a substructure called fascicles, which are 50-300μm in diameter. Many such fascicles then assemble together into a tendon tissue structure (Fratzl, 2003; Kastelic, *et al.,* 1978). "Crimpiness" in the tendon fascicles has been demonstrated using polarized light microscopy and also confirmed by scanning electron microscopy (SEM) (Franchi *et al.*, 2007). This crimpiness is also seen in OCT images of tendon tissues and their periodicity of the waviness has also been measured. Research has also been carried out to see the changes in the crimp period as a function of applied tensile strain using OCT (Hansen *et al.*, 2002).

The second type of collagenous connective tissue of our interest is cartilage which has constituent cells called chondrocytes. There are basically three categories of cartilage: elastic cartilage, hyaline cartilage and fibrocartilage which differ from each other in general composition and hence their functional properties. Cartilage is mainly composed of collagen fibers (mostly Type II collagen fibers except fibrocartilage which is mostly made of Type I collagen fibers along with Type II fibers as well), proteoglycans and water. Majority of the percentage of the composition is water. Elastic cartilage is the most flexible of the three types with elastin fibers and is commonly found in the outer ear, epiglottis, Eustachian tubes, etc. Hyaline cartilage is the most abundant of the three found in the surface of articulating joints, trachea, larynx, bronchi, etc. Hyaline cartilage found on the surface of the articulating joints is referred to as articular cartilage. A healthy articular cartilage normally comprises of 15-

22% of wet weight by collagen, which is typically Type II collagen fibers. Type II collagen fiber is a homotrimer with three α1(II) polypeptide chain. The complicated 3D microstructure is embedded with proteoglycans (4-7%) and the rest being water which interplay together to provide for the biomechanical and functional properties shown by these tissues. The main functional aspect is to decrease stress on the joints by distributing loads and also to provide for smooth joint movement with less friction and tear (Mow & Ratcliffe, 1997). Unlike the unidirectional organization of collagen fibers in tendon, collagen has a complicated 3D morphology of collagen network along the depth of the articular cartilage (Benninghoff, 1925; Clarke, 1971; Jeffery *et al.*, 1991). This has being described in detail in the previous chapters (Chapter 1). Articular cartilage has a distinct zonal structure with different orientation of collagen fiber along the different zones as described in Figure 1.7 in Chapter 1. Also the size and density of chondrocytes vary along these morphological structures of cartilage.

Fibrocartilage is the most rigid type of cartilage among the three found in intrevertebral discs, meniscus, etc. It is mainly composed of Type I collagen fibers with little amount of Type II collagen fibers. Fibrocartilage also plays a major role in wound healing. It is reported in the literature that during articular cartilage therapy for osteoarthritis, fibrocartilage takes the place of hyaline cartilage hence demonstrating a lack of the biomechanical properties shown by the normal articular cartilage.

The biochemical and morphological changes occurring in the microstructural level of the osteoarthritic developmental phase has been investigated by different studies (Seibel *et al.*, 2006; Yamamoto *et al.*, 2005). The exact reason behind the development of osteoarthritis is not known so far. Dieppe *et al.,* has elaborated on all the relevant research related to solving

the enigma around osteoarthritis (Dieppe, 1984). It is believed that the changes in the load bearing and other functional properties of articular cartilage could be attributed to the reduction or loss of the Type IX interlinking to Type II collagen fibres. Also there is a reported increase in the diameter of the collagen fibres during the onset of osteoarthritis in cartilage (Xu *et al.,* 2003). These factors could eventually lead to a change in the backscattering property of the cartilage sample under normal and osteoarthritic phase. SEM studies have also pointed out towards change in the fibrillation and disruption of the surface collagen network (Clark & Simonian, 1997). Cartilage replacement surgeries like autologous chondrocyte implantation (ACI) have not been quite successful in achieving the similar mechanical and functional properties as normal tissue (Beris *et al.*, 2005). During cartilage re-growth, fibrocartilage takes the place of hyaline cartilage, which constitutes Type I cartilage as major component along with the presence of Type II cartilage. Fibrocartilage tends to lack the same mechanical properties of the hyaline cartilage found in normal cartilage tissue (Hunziker, 2002).

With the first paper by Huang *et al.* in 1991 (Huang *et al.*, 1991), optical coherence tomography (OCT) has stridden many milestones in the field of non-invasive medical imaging technique . More detailed aspect on theory as well as literature survey on OCT has been given in Chapter 1. The added advantage to this non-invasive technology would be the ability to understand the optical properties of the underlying tissues imaged based on the nature of the backscattered light obtained. Research have been carried out in this regard with two older aspects of scattering analysis of light scattering spectroscopy based on wavelength dependent analysis of scattering (Kartakoullis *et al.*, 2010; Mourant *et al.*, 1998) and polarization dependent study of scattering (Tuchin *et al.*, 2006). Based on light scattering

based spectroscopy, scattering based analysis on nuclear size changes in precancerous epithelial cells from the normal have been reported by Backman *et al.* (Backman *et al.,* 2001; Backman *et al.,* 2000). Recently, Wax *et al.* have reported on the implementation of inverse scattering problem using Mie scattering to determine the particle size (Wax *et al.*, 2002b). It implements a low coherence interferometry system and angle-resolved technique, which could be very well implemented using an OCT system (Wax *et al.*, 2002a). Using this technique, further work has been carried out by their group to detect the abnormal changes in nuclear size in cancerous cells (Wax *et al.,* 2003). Angle-resolved techniques have been previously reported with respect to OCT system. In PS-OCT, angle-resolved technique referred to as variable incidence angle technique has been reported by Ugryumova *et al.* to study the 3D structural orientation information of collagen fibers in single layered birefringent tissue (Ugryumova *et al.*, 2006). Fanjul-Velez *et al.* have also reported on similar technique for polarimetric studies of cartilage as well as cornea (Fanjul-Vélez & Arce-Diego, 2010; Fanjul-Velez *et al.,* 2010). Huang *et al.* have recently discussed the need for calibration of OCT parameters over non-perpendicular angles of incidence over angle up to 10^{o} (Huang *et al.*, 2011). In this study, OCT based angle-resolved backscattering analysis has been implemented on bovine tendon and cartilage. The main motivation behind this study is to understand the nature of scattering differences in these two different tissues, which could provide more insight into applying this technique to scattering-based analysis in osteoarthritis.

3.3. Theory and experimental details:

Fresh bovine tissues were obtained from the hindlimb of the cattle from a local abattoir. Articular cartilage samples were extracted from the fetlock joint of the animal. Tendon along this hindlimb section was also dissected out. For our experimental studies, cartilage sample

was sectioned on the anterior side of the apex while thin slices of tendon sample were obtained, with the sectioning done along the fiber length. The remaining samples were then frozen until required.

The OCT system used for this study is a continuous polarization modulation swept source based polarization sensitive optical coherence tomography (CPM-SS-PS-OCT) system custom built in our laboratory based on the implementation scheme developed by Yamanari *et al.* (Yamanari *et al.*, 2008). However, for this experiment the polarization sensitive aspect of the system is not taken into account, as only the reflectivity data obtained from this system is used. A detailed description of the implementation of this system is given in Chapter 2 (Section 2.4) and also in Lu *et al.* (Lu *et al.*, 2011). Balanced detection is adopted with the two photoreceivers (1817-FC, New Focus, US). These photoreceivers yield the two orthogonal components, horizontal $a_h(z)$ and vertical, $a_v(z)$ which represent the moduli of the complex A-scans obtained by fast Fourier transform of the interferogram in the two orthogonal channels of the PS-OCT system. For our angle-resolved studies, to obtain the depth dependent reflectivity profile as is obtained from a common OCT system; the two orthogonal components are combined to obtain the reflectivity in Decibels as:

$$R_{dB}(z) = 10\log_{10}(a_h(z)^2 + a_v(z)^2) \qquad 3.1$$

Such depth dependent reflectivity profiles are obtained for multiple angle of illumination of incident light beam direction in two orthogonal planes of imaging (Figure 3.2).

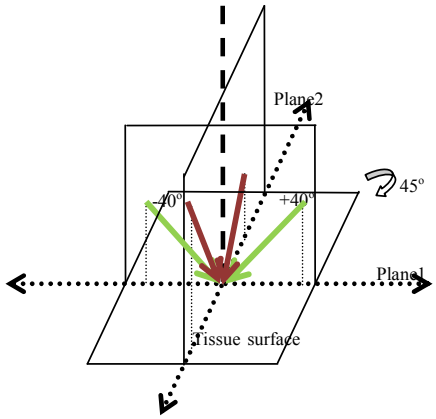

Figure 3.2: Schematic of the angle resolved technique used with the OCT system. For articular cartilage backscattering studies, the azimuthal plane is rotated by 45° as depicted.

The experimental procedure followed is called the variable incidence angle (VIA) technique which has been first put forward by Ugryumova *et al.* (Ugryumova*, et al.*, 2006) for single layer birefringent tissue like tendon which has got a very directional orientation of collagen fiber throughout the entirety of the tissue section. More details on this technique are described in Chapter 2. For this angle resolved scattering studies, the two orthogonal planes were defined differently for the two tissues under investigation. For the bovine tendon sample, the two orthogonal planes are $x-z$ and $y-z$ in the Cartesian coordinate system with z–axis along the axial depth and collagen fibers oriented in the x–direction. This particular choice of coordinate system is not applicable for articular cartilage, as it is not possible to visually locate the collagen fiber orientation of the superficial layer. Hence, a totally different system of defining the two orthogonal planes has been implemented here. The planes are defined with respect to the anatomical planes with respect to the plane in which the fetlock joint constrains the two connected bones to flex, which is the sagittal plane. Thus, $x-z$ is the

sagittal plane, which is the plane parallel to the sagittal ridge, and $y-z$ is the coronal plane.

The depth dependent plots of reflectivity profiles obtained using Equation 3.1 are averaged for 50 lateral A-scans. This profile is fitted to a least squares linear curve. Various theoretical models have been proposed to understand the optical properties of the biological tissues that scatter light in OCT based imaging. Earlier models were based on single scattering events while recently models with both multiple and single scattering regime has been put forward as well. One such theory is the implementation of extended Huygens-Fresnel principle first described for electromagnetic beam propagation with respect to atmospheric optics (Lutomirski & Yura, 1971) has been used to analyse and build up a scattering model that describes OCT system (Thrane *et al.*, 2000).

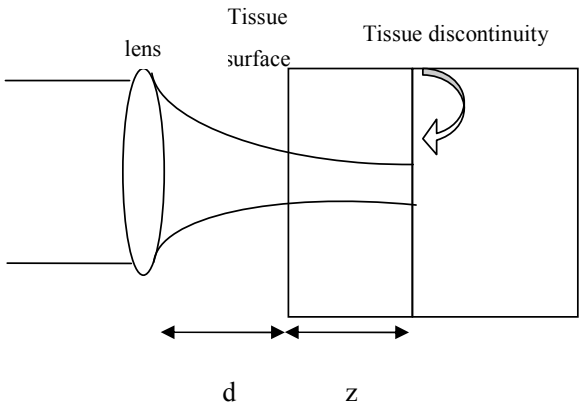

Figure 3.3: Schematic of light scatter geometry of a biological tissue in an OCT system

Based on the light scatter geometry of OCT system given in Figure 3.3, the mean square detected signal at the photoreceiver of OCT system is given by (Andersen *et al.,* 2004; Thrane, *et al.,* 2000):

$$\left\langle i^2(z)\right\rangle = \frac{\alpha^2 P_R P_S \sigma_b}{\pi w_H^2}\left[e^{-2\mu_s z} + \frac{4e^{-\mu_s z}(1-e^{-\mu_s z})}{1+\left(w_S^2 / w_H^2\right)} + (1-e^{-\mu_s z})^2 \frac{w_H^2}{w_S^2}\right] \quad 3.2$$

Or,

$$\left\langle i^2(z)\right\rangle \equiv \left\langle i^2\right\rangle_0 \Psi(z) \quad 3.3$$

where,

α is the conversion factor for optical power to electrical current

μ_s is the scattering coefficient which is also given by the reciprocal of the mean free path of photon propagation in the sample

σ_b is the back scattering coefficient

P_R, P_S are the optical powers from reference and sample arms

w_H^2, w_S^2 are the beam spot sizes in the backscattering plane of Figure 3.3 in the absence and presence of scattering, respectively.

In Equation 3.2, the first term represents the coherent scattering given by the single backscattering model; the second term is the cross-talk term of unscattered and multiple scattered light interactions whereas the third term accounts for the multiple backscattering events of incoherent scattering. The OCT signal obtained is given by

$\left[\left\langle i^2(z)\right\rangle\right]^{1/2}$. Previous research has shown the effect of multiple backscattering on OCT images include reduction in contrast and resolution of OCT image over imaging depth (Pan *et al.*,

1997), change in the slope of the intensity versus depth profile to a less steep value after certain depths of imaging (Thrane*, et al.*, 2000; Yadlowsky *et al.*, 1995). Hence, in this thesis, a single backscattering model (Schmitt *et al.*, 1993) has been adopted with the assumption that the coherent gated detection in low coherence interferometric measurement of OCT signals could be simplistically restricted to the first term in Equation 3.2. This is also based on the previous single model analysis presented for OCT systems (Schmitt*, et al.*, 1993). Thus, from Equation 3.2, the reflectivity profile represented in decibels follows this single backscattering model, which represents the following equations:

$$I_{OCT} = \sqrt{\frac{\alpha^2 P_R P_S \sigma_b}{\pi w_H^2}}.e^{-\mu_s z} \qquad 3.4$$

$$I_{OCT}(dB) = I_o - \mu_s z \qquad 3.5$$

From Equation 3.5, the y-intercept of the linear fit of the depth-dependent reflectivity profiles is directly proportional to the square root of optical back-scattering coefficient. In our angle resolved back scattering studies, y-intercept obtained upon linear fit of 50 A-scan averages over multiple angle of illuminations ranging from $+40^o$ to -40^o with respect to the surface normal in two orthogonal planes as defined for the two tissues are being plotted and compared.

Depth dependent reflectivity profiles are obtained for different angle of illumination ranging from $+40^o$ to -40^o with a step of 20^o for both the tissues in two orthogonal planes chosen. From the reflectivity versus depth linear fit, angle resolved y-intercept of 50 A-scan averages are obtained. A typical OCT images of the tendon and cartilage sample and the corresponding reflectivity versus depth profiles as well as the calculation of the y-intercept is shown in

Figures 3.4 & 3.5, respectively. The sudden drop in the reflectivity profiles at around a tendon sample depth calculated as 523±47 μm reveals a distinct morphological zone which has to be established by carrying out further studies like histology to correlate the OCT image with the actual morphology of the articular cartilage.

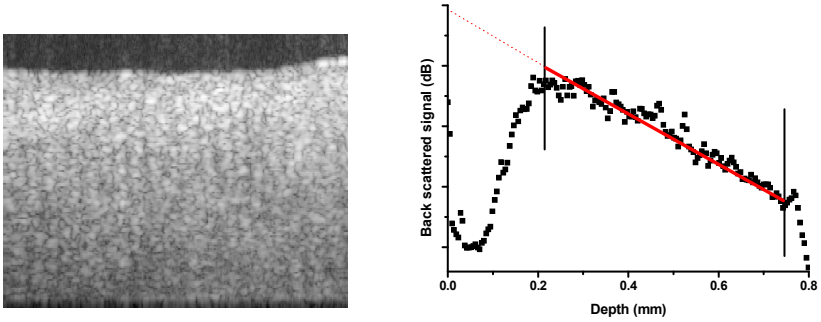

Figure 3.4: Typical OCT image of tendon sample and the corresponding reflectivity versus depth of scan profile for 50 A-scans averages. Solid red line gives the linear fit to calculate the y-intercept. The first vertical black stripe in the plot gives an indication of the approximation location of air tissue interface

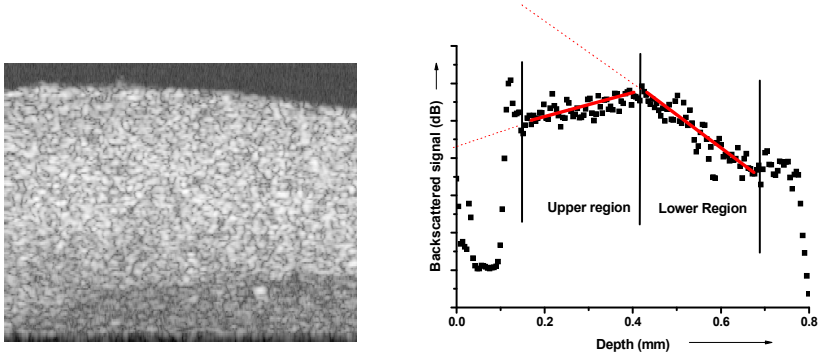

Figure 3.5: Typical OCT image of cartilage sample and the corresponding reflectivity versus depth of scan profile for 50 A-scans averages. Solid red line gives the linear fit to calculate the y-intercept. The first vertical black stripe in the plot gives an indication of the approximation location of air tissue interface

From Figure 3.5, it can be seen that the depth versus reflectivity profile of cartilage tissue

could be divided into two distinct regions. The upper region, in which case it is considered the single-backscattering model holds, has a positive slope. Similar results of positive slopes have been obtained in OCT profiles of dysplastic oral tissues as reported by Tomlins *et al.* (Tomlins *et al.,* 2010) This behavior reflects a depth dependent increase in backscattered signal that compensates the attenuation due to elastic scattering along the depth of the tissue. This behavior could be attributed to the change in cell or fiber density, size or alignment as well as refractive index variations along the tissue depth. Also, the upper and lower regions of the depth profile in cartilage are fitted to a linear regression curve separately and the angle-resolved y-intercept plots from the two regions are plotted separately as in Figures 3.6 & 3.7. This behavior requires further investigation to look into the reasons behind this. The reflectivity versus depth curve of tendon follows a normal attenuation profile and the single back-scattering model is fitted to it to obtain the angle-resolved y-intercept plot (Figure 3.8). Error bars are also shown with these plots taken over three data sets for tendon and cartilage.

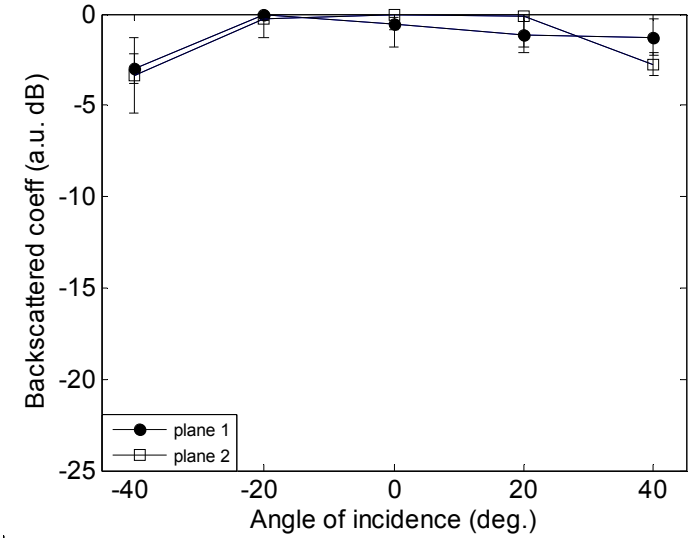

Figure 3.6: Angle-resolved plots of backscattering for cartilage (upper region)

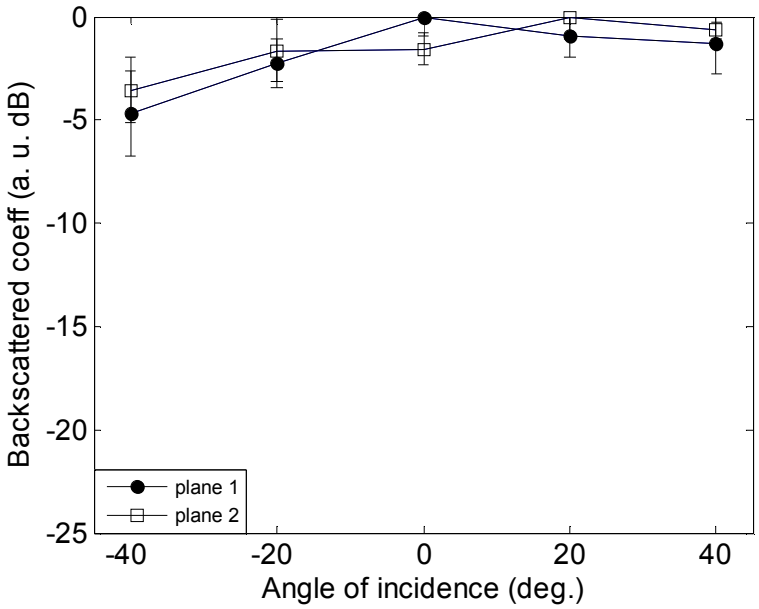

Figure 3.7: Angle-resolved plots of backscattering for cartilage (lower region)

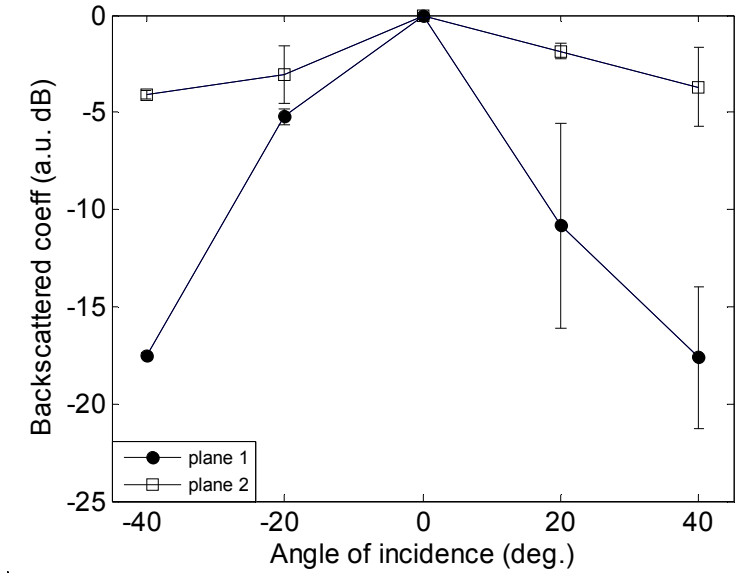

Figure 3.8: Angle-resolved plots of backscattering for tendon tissue sample.

Angle-resolved plots of the y-intercept of the linear fit of averaged A-scans for these tissues, henceforth, is an indicative parameter of the backscattering coefficient shown by these tissues. For cartilage with complicated 3D nature of the orientation of the collagen fibers, two sets of angle-resolved data are obtained. First set of data is obtained as explained previously, i.e.; with respect to the sagittal system in two orthogonal planes and the second one is obtained by rotating this plane of imaging over an azimuth of 45^{o}. Any large-scale difference occurring in the obtained angle-resolved plots due to the orientation of the superficial fibers with respect to incident beam would be evident over the differences in the outcome of the result over these data. However, the scattering profiles obtained in the both these set of experiments fall within the error plots shown in Figures 3.6 & 3.7. For tendon only one set of data is taken owing to its directional nature of collagen fiber arrangement.

Figures 3.6-3.8 reveal the differences in the angle-resolved backscattered optical signal plot obtained from tendon and cartilage. While for cartilage the drop in optical backscattered intensity is in the range 0.5-4dB in both the imaging planes, tendons show a much greater fall in backscattered profile ranging to almost 18dB in one of the orthogonal plane of imaging. The basic differences in the nature of scatterers involved in these two different tissues have been evident based on these angle-resolved backscattering profiles. Cartilage shows an isotropic scattering profile with a flat angle-resolved scattering plot obtained while tendon plot shows anisotropic nature in the scattering events from the scatterers involved. The reason behind this difference in the behavior of the backscattering profiles of bovine tendon and articular cartilage tissue is investigated upon using Rayleigh-Gans scattering approximation, which is discussed in detail in the next section (Section 3.4).

3.4. Rayleigh-Gans approximation

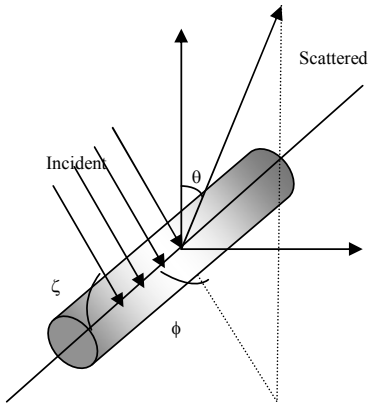

Figure 3.9: Schematic of the cylinder geometry used for Rayleigh-Gans approximation

Rayleigh-Gans theory is equivalent to the first order Born approximation scattering theory of quantum mechanics, where the intra-particle multiple scattering has been disregarded by assuming unperturbed light field interaction of small polarizability (Bohren & Huffman, 1983). Hence, Rayleigh Gans theory is very well applicable to the biological tissues consisting of scatterers of arbitrary shapes, which could be modelled as dipoles independent of each other, and also that satisfies the two conditions, which is discussed further in this section. In our studies, collagen fibril has been modelled as finite cylinder of length $2L$ and diameter $2a$ and the backscattered intensity of light have been simulated over a scattering volume V. This has been plotted as a function of angle of incident light illumination, which gives us the required curve of angle-resolved back scattering profiles.

From the geometry shown in Figure 3.9, using the cylindrical coordinate system, the incident and scattered beam directions are given by:

$$\hat{e}_i = \sin\xi\hat{e}_z - \cos\xi\hat{e}_x \qquad 3.6$$

$$\hat{e}_r = \sin\theta\cos\phi\hat{e}_x + \sin\theta\sin\phi\hat{e}_y + \cos\theta\hat{e}_z \qquad 3.7$$

respectively. For backscattering at 180^o as in OCT backscattering, the scattered beam direction has to satisfy the following relation $\hat{e}_r = -\hat{e}_i$. This is achieved for $\theta = \frac{\pi}{2} + \xi$, so that Equation 3.7 can be rewritten as: $\hat{e}_r = \cos\xi\cos\phi\hat{e}_x + \cos\xi\sin\phi\hat{e}_y - \sin\xi\hat{e}_z$

Substituting $\phi = 0^o$ reduces it to $\hat{e}_r = \cos\xi\hat{e}_x - \sin\xi\hat{e}_z = -\hat{e}_i$.

The two criteria to be satisfied by the scatterers for Rayleigh-Gans approximation are:

(i) The complex refractive index of the scatterer relative to its surrounding medium, m is close to 1, $|m-1| << 1$.

(ii) The phase shift δ of the incident light beam through the particle is very small, $\delta = 2ka|m-1| << 1$, where $2a$ is the particle diameter.

In our studies, these two criteria are met by both tendon and cartilage fibril cylinder. The cylinder diameters of tendon and cartilage fibrils are taken to be around 300nm and 30nm, respectively, which gives the value of δ very much less than 1 (0.1 for tendon and 0.006 for cartilage). For our simulation studies the refractive indices of tendon is taken to be 1.43 which gives m = 1.075 with respect to water (n = 1.33) (de Boer *et al.*, 1997). For cartilage with a refractive index of 1.38, the value of m is obtained as 1.038 (Wang *et al.*, 2008). Henceforth, both the criteria of Rayleigh Gans approximation holds true for both tendon and cartilage fibril cylinders.

The incident and scattered amplitudes when an electromagnetic field scatters a particle are

related to each other by the amplitude scattering matrix (Bohren & Huffman, 1983) given by:

$$\begin{pmatrix} E_{\|s} \\ E_{\perp s} \end{pmatrix} = \frac{e^{ik(r-z)}}{-ikr} \begin{pmatrix} S_2 & S_3 \\ S_4 & S_1 \end{pmatrix} \begin{pmatrix} E_{\|i} \\ E_{\perp i} \end{pmatrix} \tag{3.8}$$

where $E_{\|s}, E_{\perp s}, E_{\|i}, E_{\perp i}$ are the parallel and perpendicular components of the scattered and incident fields, respectively. The elements $S_j\,(j = 1,2,3,4)$ are dependent on the nature, type and orientation of the scatterers involved. Considering the symmetric conditions for the Rayleigh-Gans particles, Equation 3.8 is reduced to

$$\begin{pmatrix} E_{\|s} \\ E_{\perp s} \end{pmatrix} = \frac{e^{ik(r-z)}}{-ikr} \begin{pmatrix} S_2 & 0 \\ 0 & S_1 \end{pmatrix} \begin{pmatrix} E_{\|i} \\ E_{\perp i} \end{pmatrix} \tag{3.9}$$

with non-diagonal elements zero. Here,

$$S_1 = \frac{-ik^3}{2\pi}(m-1)v f(\theta,\phi) \tag{3.10}$$

$$S_2 = \frac{-ik^3}{2\pi}(m-1)v f(\theta,\phi)\cos\theta \tag{3.11}$$

where, θ, ϕ are the scattering polar and azimuthal angle with respect to the surface normal of the cylinder long axis.

The form factor $f(\theta,\phi)$ is

$$f = \frac{1}{\pi a^2 2L} \int_{-L}^{+L} e^{-kAx} dx \int_0^a \rho d\rho \int_0^{2\pi} e^{-ik\rho(B\cos\psi + C\sin\psi)} d\psi \tag{3.12}$$

Rayleigh-Gans approximation is fundamentally based on the theory of Rayleigh scattering

which is a form of elastic scattering. Referring back to Born approximation in terms of atomic physics, form factor is given as the Fourier transform of the potential function with respect to the momentum transfer. In this type of scattering, the energy is conserved and the scattering intensity is dependent on the momentum transfer function which is better understood from Figure 3.10.

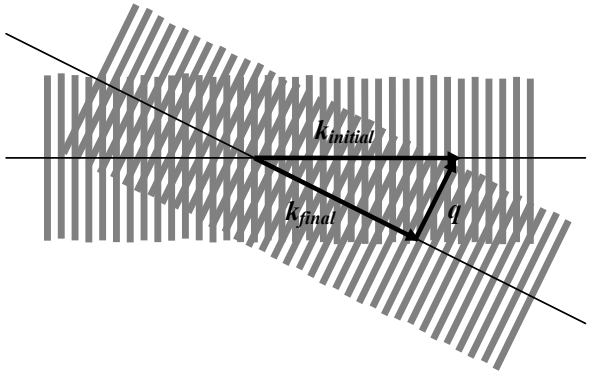

Figure 3.10: Schematic of the scattering geometry with respect to the incident and scattered wavevector to obtain the scattering vector, q .

The change in the direction of the momentum given by the scattering vector, $q = k_{final} - k_{initial}$ thus defines the scattering event. For biological tissues, which also include birefringent samples, this approximation of elastic scattering is a very simplifying model to describe the scattering events. For the tissue samples under investigation, form factor is given as the Fourier transform of the scatterer geometry and distribution function based on the treatment of the RG particle in tissue optics as a small fluctuating lump of dielectric quasi-continuum. This is a direct application of Wiener-Khintchine theorem and has been used in previous angular dependency second harmonic scattering studies carried out by Freund *et al.* (Freund *et al.*, 1986).

For a finite cylinder, form factor of the scattering event is given by:

$$f(\theta,\phi;\zeta)=\frac{2\sin(x\Gamma A)}{x\Gamma A}\frac{J_1(xM)}{xM} \qquad 3.13$$

where,

$x = k.a$

$\Gamma = \frac{L}{a}$ is the aspect ratio of the fibril cylinder

$A = \cos\zeta + \sin\theta\cos\phi$

$B = \sin\theta\sin\phi$

$C = \cos\theta - \sin\zeta$

$M = \sqrt{B^2 + C^2}$

k is the wave vector-modulus

ζ is the angle of incidence with respect to the cylinder axis

θ, ϕ gives the polar and azimuth angles of orientation of scattered beam with respect to the surface normal of cylinder long axis.

From this scattering matrix, the relation between incident and scattered Stokes parameters for a finite cylinder is obtained as

$$\begin{pmatrix} I_s \\ Q_s \\ U_s \\ V_s \end{pmatrix} = \frac{1}{k^2 r^2} \begin{pmatrix} S_{11} & S_{12} & 0 & 0 \\ S_{21} & S_{22} & 0 & 0 \\ 0 & 0 & S_{33} & S_{34} \\ 0 & 0 & S_{43} & S_{44} \end{pmatrix} \begin{pmatrix} I_i \\ Q_i \\ U_i \\ V_i \end{pmatrix} \quad 3.14$$

where,

$$S_{11} = S_{22} = \frac{1}{2}(|S_1|^2 + |S_2|^2) \quad 3.15$$

$$S_{12} = S_{21} = \frac{1}{2}(|S_2|^2 - |S_1|^2) \quad 3.16$$

$$S_{33} = S_{44} = \mathrm{Re}(S_1 S_2^*) \quad 3.17$$

$$S_{34} = \mathrm{Im}(S_2 S_1^*) \quad 3.18$$

$$S_{43} = \mathrm{Im}(S_1 S_2^*) \quad 3.19$$

For unpolarised light,

$$\begin{pmatrix} I_s \\ Q_s \\ U_s \\ V_s \end{pmatrix} \sim \begin{pmatrix} S_{11} \\ S_{12} \\ 0 \\ 0 \end{pmatrix} \quad 3.20$$

For unpolarised, S_{11} gives the total scattered intensity. Using Matlab™, the angle-resolved scattered light intensity S_{11} for different angles of incidents in two orthogonal planes for the two different tissues are obtained and a comparison study is done with the experimentally obtained results.

In this study the reason behind the experimentally obtained behavioral difference in the angle-resolved backscattering plots for the two different tissues is reasoned out by carrying out simulation studies based on Rayleigh-Gans approximation. For this, the scatterer involved in both the cartilage and the tendon is modelled as a finite cylinder of length L and radius a and obtain the angle-resolved backscattering profiles. The hypothesis is based on the difference in scatterer size and packing arrangement of the collagen fibrils involved in the two tissues could provide a suitable explanation to the differences in the behavior seen. Finer and smaller diameter collagen fibrils in cartilage show isotropic backscattering profile whereas larger diameter collagen fibril interpacked randomly with thinner fibrils in tendon, i.e.; a coarse packing nature with larger cylinder diameter interspaced with smaller diameter fibrils results in anisotropic behavior shown by tendon tissue. A reference to this kind of random size distribution seen in collagen fibers in tendon is mentioned in Freund *et al.* (Figure 3.11).

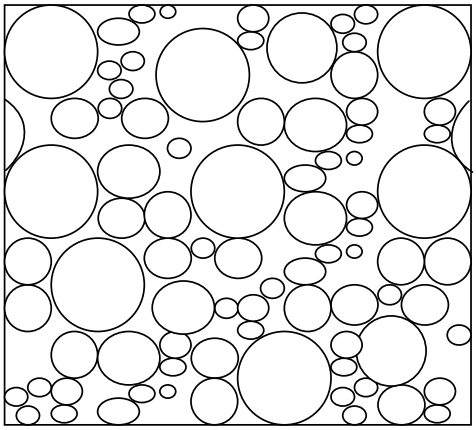

Figure 3.11: 2D arrangement of tendon fibrils as in (Freund, et al., 1986)

This is supported by the results obtained using RG theory by choosing scatterers of different

aspect ratio to reflect the difference of scatterers in tendon and cartilage. Figure 3.12 shows the obtained angle-resolved scattering plot for tendon fibril (cylinder of diameter 300nm) of aspect ratio 10 compared with that of the scattering plot obtained for a homogeneous scattering event by cartilage (cylinder fibril of diameter 30nm and aspect ratio 1). This preliminary simulation result provides an insight into the nature of differences that could be attributed to the difference obtained in the angle-resolved backscattering profiles obtained from the bovine tendon and cartilage. A simple model has been used here to explain the results using a single fibrillar structure. A more rigorous analysis would involve taking into account the close packing density of the collagen fibrils to obtain 3D distribution of scatterers in OCT imaging. This model could potentially reproduce the observed features of the angle-resolved backscattering, while suppressing the periodic oscillations in backscattering profiles as seen in the plots of tendon tissue in Figure 3.12.

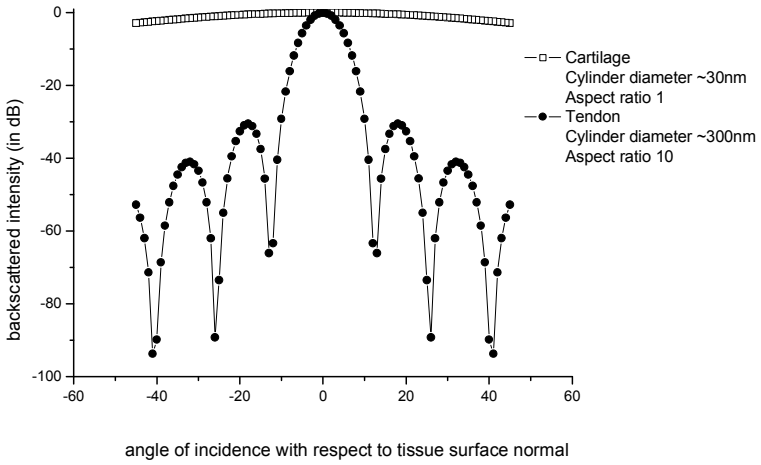

Figure 3.12: Angle-resolved backscattering profiles obtained for tendon and cartilage fibril cylinders using RG approximation. The simulation was run over incidence angles from $+45^o$ to -45^o with 1^o increments over each measurement.

3.5. Conclusions:

In this study, the difference in the backscattering profiles of the bovine tendon and cartilage sample has been brought into picture. An hypothesis to explain this difference seen by attributing it to the difference in the nature and type of the scatterer involved in the two tissues: coarsely packed, randomly distributed thicker Type I collagen fibers in tendon sample whereas finer and homogeneous Type II collagen fibers in cartilage is also discussed. Reflectivity data from PS-OCT has been used to obtain the angle-resolved backscattering data. RG approximation has been applied in order to study the scattering event from the microstructures of cartilage as well as tendon. Using RG theory, a very simple single fibrillar model is being implemented to explain the experimental behavior of the backscattering signal obtained from OCT data of tendon and cartilage.

3.6. Further scope of study:

Using RG approximation, a more rigorous model could be developed that could fully account for the differences seen in the angle-resolved backscattering profiles of cartilage and tendon. This could be carried out by taking into account the packing density of the collagen fibrils in the tissue as well as a 3D arrangement of scatterers in the two tissues with respect to the focal volume of the OCT system. Implementation of a more rigorous model taking into account the system parameters of our PS-OCT system, the lateral and axial resolution provided by the system could also be considered. Experimental studies could be extended to find out if there exist any considerable difference in angle resolved backscattering plots of normal and diseased cartilage as well as if this backscattering profile could be calibrated over different phases of osteoarthritis for non-invasive therapy and diagnostic applications.

3.7. References:

Andersen, P. E., Thrane, L., Yura, H. T., Tycho, A., Jorgensen, T. M., & Frosz, M. H. (2004). Advanced modelling of optical coherence tomography systems. *Phys Med Biol, 49*(7), 1307-1327.

Backman, V., Gopal, V., Kalashnikov, M., Badizadegan, K., Gurjar, R., Wax, A. (2001). Measuring cellular structure at submicrometer scale with light scattering spectroscopy. *IEEE Journal of Selected Topics in Quantum Electronics, 7*(6), 887-893.

Backman, V., Wallace, M. B., Perelman, L. T., Arendt, J. T., Gurjar, R., Muller, M. G. (2000). Detection of preinvasive cancer cells. *Nature, 406*(6791), 35-36.

Benninghoff, A. (1925). Form und Bau der Gelenkknorpel in ihren Beziehungen zur Funktion. *Cell and Tissue Research, 2*(5), 783-862.

Beris, A. E., Lykissas, M. G., Papageorgiou, C. D., & Georgoulis, A. D. (2005). Advances in articular cartilage repair. *Injury, 36 Suppl 4*, S14-23.

Bohren, C. F., & Huffman, D. R. (1983). Rayleigh-Gans Theory *Absorption and scattering of light by small particles* (pp. 158-165.). New York: Wiley.

Clark, J. M., & Simonian, P. T. (1997). Scanning electron microscopy of "fibrillated" and "malacic" human articular cartilage: technical considerations. *Microscopy Research and Technique, 37*(4), 299-313.

Clarke, I. C. (1971). Articular Cartilage: a review and scanning electron microscope study: 1. The Interterritorial Fibrillar Architecture. *J Bone Joint Surg Br, 53-B*(4), 732-750.

de Boer, J. F., Milner, T. E., van Gemert, M. J. C., & Nelson, J. S. (1997). Two-dimensional birefringence imaging in biological tissue by polarization-sensitive optical coherence tomography. *Opt. Lett., 22*(12), 934-936.

Dieppe, P. (1984). Osteoarthritis: are we asking the wrong questions? *Br J Rheumatol, 23*(3), 161-163.

Fanjul-Vélez, F., & Arce-Diego, J. L. (2010). Polarimetry of birefringent biological tissues with arbitrary fibril orientation and variable incidence angle. *Opt. Lett., 35*(8), 1163-1165.

Fanjul-Velez, F., Pircher, M., Baumann, B., Gotzinger, E., Hitzenberger, C. K., & Arce-Diego, J. L. (2010). Polarimetric analysis of the human cornea measured by polarization-sensitive optical coherence tomography. *Journal of Biomedical Optics, 15*(5), 056004-056010.

Franchi, M., Fini, M., Quaranta, M., De Pasquale, V., Raspanti, M., Giavaresi, G. (2007). Crimp morphology in relaxed and stretched rat Achilles tendon. *J Anat, 210*(1), 1-7.

Fratzl, P. (2003). Cellulose and collagen: from fibres to tissues. [doi: 10.1016/S1359-0294(03)00011-6]. *Current Opinion in Colloid & Interface Science, 8*(1), 32-39.

Freund, I., Deutsch, M., & Sprecher, A. (1986). Connective tissue polarity. Optical second-harmonic microscopy, crossed-beam summation, and small-angle scattering in rat-tail tendon. *Biophys J, 50*(4), 693-712.

Hansen, K. A., Weiss, J. A., & Barton, J. K. (2002). Recruitment of tendon crimp with applied tensile strain. *J Biomech Eng, 124*(1), 72-77.

Huang, D., Swanson, E. A., Lin, C. P., Schuman, J. S., Stinson, W. G., Chang, W. (1991). Optical coherence tomography. *Science, 254*(5035), 1178-1181.

Huang, Y.-P., Saarakkala, S., Toyras, J., Wang, L. K., Jurvelin, J. S., & Zheng, Y. P. (2011). Effects of optical beam angle on quantitative optical coherence tomography (OCT) in normal and surface degenerated bovine articular cartilage. *Physics in Medicine and Biology, 56*(2), 491.

Hunziker, E. B. (2002). Articular cartilage repair: basic science and clinical progress. A review of the current status and prospects. *Osteoarthritis Cartilage, 10*(6), 432-463.

Jeffery, A., Blunn, G., Archer, C., & Bentley, G. (1991). Three-dimensional collagen architecture in bovine articular cartilage. *J Bone Joint Surg Br, 73-B*(5), 795-801.

Kartakoullis, A., Bousi, E., & Pitris, C. (2010). Scatterer size-based analysis of optical coherence tomography images using spectral estimation techniques. *Opt Express, 18*(9), 9181-9191.

Kastelic, J., Galeski, A., & Baer, E. (1978). The multicomposite structure of tendon. *Connect Tissue Res, 6*(1), 11-23.

Lu, Z., Kasaragod, D. K., & Matcher, S. J. (2011). Optic axis determination by fibre-based polarization-sensitive swept-source optical coherence tomography. *Phys Med Biol, 56*(4), 1105-1122.

Lutomirski, R. F., & Yura, H. T. (1971). Propagation of a Finite Optical Beam in an Inhomogeneous Medium. *Appl. Opt., 10*(7), 1652-1658.

Mourant, J. R., Freyer, J. P., Hielscher, A. H., Eick, A. A., Shen, D., & Johnson, T. M. (1998). Mechanisms of light scattering from biological cells relevant to noninvasive optical-tissue diagnostics. *Appl Opt, 37*(16), 3586-3593.

Mow, V. C., & Ratcliffe, A. (1997). Structure and Function of Articular Cartilage and Meniscus. In V. C. Mow & W. C. Hayes (Eds.), *Basic Orthopaedic Biomechanics* (pp. 113-177): Lippincott-Raven New York.

Pan, Y., Birngruber, R., & Engelhardt, R. (1997). Contrast limits of coherence-gated imaging in scattering media. *Appl. Opt., 36*(13), 2979-2983.

Schmitt, J. M., Knuttel, A., & Bonner, R. F. (1993). Measurement of optical properties of biological tissues by low-coherence reflectometry. *Appl Opt, 32*(30), 6032-6042.

Seibel, M. J., Robins, S. P., & Bilezikian, J. P. (2006). *Dynamics of bone and cartilage metabolism* (2nd ed.). San Diego: Academic Press.

Thrane, L., Yura, H. T., & Andersen, P. E. (2000). Analysis of optical coherence tomography systems based on the extended Huygens-Fresnel principle. *J Opt Soc Am A, 17*(3), 484-490.

Tomlins, P. H., Adegun, O., Hagi-Pavli, E., Piper, K., Bader, D., & Fortune, F. (2010). Scattering attenuation microscopy of oral epithelial dysplasia. *J Biomed Opt, 15*(6), 066003.

Tuchin, V. V., Wang, L. V., & Zimnyakov, D. A. (2006). *Optical Polarization in Biomedical Optics*. Berlin Heidelberg: Springer-Verlag, .

Ugryumova, N., Gangnus, S. V., & Matcher, S. J. (2006). Three-dimensional optic axis determination using variable-incidence-angle polarization-optical coherence tomography. *Opt. Lett., 31*(15), 2305-2307.

Wang, S. Z., Huang, Y. P., Wang, Q., & Zheng, Y. P. (2008). Assessment of depth and degeneration dependences of articular cartilage refractive index using optical coherence tomography in vitro. *Conf Proc IEEE Eng Med Biol Soc, 2008*, 4047-4050.

Wax, A., Yang, C., Muller, M. G., Nines, R., Boone, C. W., Steele, V. E. (2003). In situ detection of neoplastic transformation and chemopreventive effects in rat esophagus epithelium using angle-resolved low-coherence interferometry. *Cancer Res, 63*(13), 3556-3559.

Wax, A., Yang, C. H., Backman, V., Badizadegan, K., Boone, C. W., Dasari, R. R. (2002a). Cellular organization and substructure measured using angle-resolved low-coherence interferometry. *Biophysical Journal, 82*(4), 2256-2264.

Wax, A., Yang, C. H., Backman, V., Kalashnikov, M., Dasari, R. R., & Feld, M. S. (2002b).

Determination of particle size by using the angular distribution of backscattered light as measured with low-coherence interferometry. *J Opt Soc Am A, 19*(4), 737-744.

Xu, L., Flahiff, C. M., Waldman, B. A., Wu, D., Olsen, B. R., Setton, L. A. (2003). Osteoarthritis-like changes and decreased mechanical function of articular cartilage in the joints of mice with the chondrodysplasia gene (cho). *Arthritis & Rheumatism, 48*(9), 2509-2518.

Yadlowsky, M. J., Schmitt, J. M., & Bonner, R. F. (1995). Multiple scattering in optical coherence microscopy. *Appl Opt, 34*(25), 5699-5707.

Yamamoto, K., Shishido, T., Masaoka, T., & Imakiire, A. (2005). Morphological studies on the ageing and osteoarthritis of the articular cartilage in C57 black mice. *J Orthop Surg (Hong Kong), 13*(1), 8-18.

Yamanari, M., Makita, S., & Yasuno, Y. (2008). Polarization-sensitive swept-source optical coherence tomography with continuous source polarization modulation. *Opt. Express, 16*(8), 5892-5906.

CHAPTER 4

Speckle Texture Analysis of OCT Images

4.1. Summary

In this chapter, work carried out towards automated classification of different types of melanoma invasion in tissue engineered skin is reported. Starting out with statistical feature detection of intensity values of OCT images based on speckle texture analysis, a control experiment was first carried out to classify different concentrations of agar-Intralipid concentrations using the algorithm. Later on, this algorithm was implemented to attempt to classify different types of melanoma cell lines invasion on tissue engineered skin which was monitored over weeks of growth culture using a swept source OCT system.

4.2. Introduction

OCT has established itself as powerful imaging modality with established clinical diagnostic ability in ophthalmic applications and further fields of application currently under research. The full utilization of the potential of OCT in clinical diagnosis demands implementation of automated data classification schemes using computational methods (Bazant-Hegemark & Stone, 2009). The ability of OCT to offer resolution of 10-15μm and even ultrahigh resolution (Drexler *et al.*, 2001; Drexler *et al.*, 1999), along with the technological advances leading to real time OCT applications, as well as the *in-vivo* imaging capability makes OCT a potential candidate towards use in clinical applications. This is also supported by additional properties available including the use of contrast agents as well as the specialized modalities available including Doppler OCT, PS-OCT, and spectroscopic OCT which provides functional properties of the tissues along with the structural information given by conventional OCT imaging. The solution of automated classification or computer-aided diagnosis is problem specific. Various research groups have carried out different methods to preprocess the OCT data, to extract relevant features from the OCT image, and to put the features into a classification algorithm. Bazant-Hegemark *et al.* reports a broader perspective of the current situation regarding to data automation in OCT in all types of tissues (Bazant-Hegemark & Stone, 2009). DeBuc *et al.* provides a detailed review of the automated segmentation studies carried out in retinal OCT images (DeBuc, 2011).

An attempt at computer aided classification of different types of melanoma cell-lines invasion in the tissue engineered skin is reported here. A swept source based OCT system was used to monitor the growth of a tissue-engineered normal skin as well as one with the different types of melanoma invasion. Statistical features were extracted from speckle patterns obtained from the OCT images. Prior to carrying out the speckle texture analysis on

the tissue engineered skin, a control experiment was carried out to classify different concentration of agar-Intralipid (agar-IL) using this algorithm. Mahalanobis classification scheme is applied and a 3-feature scatter plot is plotted to show the ability of the algorithm to classify the different concentrations of agar-IL based on OCT contrast obtained. This has also been supported with receiver operating characteristics (ROC) curves. However, the main conclusion is that this scheme does not show satisfactory results to classify melanoma types from normal skin, or to classify different types of melanoma from one another in the tissue engineered skin model.

4.3. Speckles and origin of speckles in OCT:

Speckles are the random granular patterns often observed when a coherent beam of light is reflected off from a diffuse surface. The study related to speckle gained momentum during 1960s with the advent of lasers and a detailed statistical study is available (Dainty, 1984). The temporal and spatial coherence of these laser sources became excellent source of speckle pattern formation, in which the secondary wavefronts produced from the scattered light beam of a rough surface interfered over length scales less than the coherence length of the sources. However this classical explanation of the speckle formation does not completely explain the origin of speckles in OCT which is basically a low coherence interferometric based imaging. Schmitt *et al.* has presented a very detailed study on the origin of speckle in OCT by attributing it to two major factors:

(a) the classical approach of interference from random scatterers

(b) bandpass detection mode of imaging employed in heterodyne detection of OCT (Schmitt *et al.*, 1999).

The contrast seen in the OCT images is attributed to the spatial variations in the refractive index of the biological tissues which is mathematically modeled similar to the Kolmogorov model of atmospheric turbulences (Schmitt & Kumar, 1996). These spatial variations of refractive index gives rise to the back-scattering phenomena that give rise to OCT contrast seen in the biological tissues in OCT imaging which includes both coherent and incoherent nature of scattering. As per the classical approach, multiple backscattering of incident light beam and random delays between the forward-propagating and return beams in multiple forward scattering modifies the wavefront detected by OCT. The missing frequency problem (Schmitt*, et al.*, 1999) due to the narrowband response function of the OCT system also affects the speckle pattern from biological tissues, as was described by a theoretical study of OCT in turbid media by Pan *et al.* (Pan *et al.*, 1995). Schmitt *et al.* refers to the speckle originating by these processes as speckle which is made up of information carrying as well as information degrading signals, hard to distinguish one from the other. A general description of the statistical properties of speckle in OCT is available in several reviews (Fercher *et al.*, 2003; Schmitt*, et al.*, 1999). The speckle generated in OCT imaging are dependent on the size and temporal coherence of the source, detector aperture, multiple scatterings occurring in the focal volume (Hillman *et al.*, 2010), the optical properties of the tissue imaged, etc (Schmitt*, et al.*, 1999). Hillman *et al.,* have also reported on the dependence of the OCT contrast ratio on the optical properties and scattering density of the media under study (Hillman *et al.*, 2006).

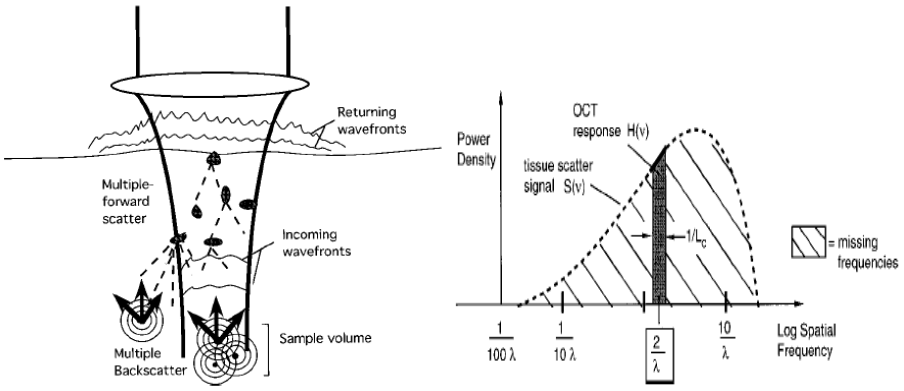

Figure 4.1: Origin of speckle (a) Classical randon interference from scatterers approach (b) Missing frequency problem related to OCT narrowband detection (Schmitt, *et al.*, 1999).

Although this granular intensity patterns of speckle is considered to be a bane in imaging be it, ultrasound, radar or OCT, several groups have tried to extract valuable information hidden in the speckle data (Fankhauser & Kwasniewska, 2003), involving both static and dynamic speckles in various different fields involved for example, stellar speckle interferometry in astronomy (Dainty, 1984) , speckle flowmetry in medicine (Barton & Stromski, 2005; Briers, 2001; Duncan & Kirkpatrick, 2008; Mariampillai *et al.*, 2008; Strong *et al.*, 2006), using statistical methods involving speckle texture analysis of ultrasound images (Kim *et al.*, 1998; Thijssen, 2003) , synthetic-aperture radar (SAR) images (Soh & Tsatsoulis, 1999; Touzi *et al.*, 1988; Ulaby *et al.*, 1986) as well as OCT images (Gossage *et al.*, 2006; Gossage *et al.*, 2003; Lingley-Papadopoulos *et al.*, 2008; Manyak *et al.*, 2007)

4.4. Automation of data analysis in OCT images:

The utility of an imaging modality to clinical methods requires improving the decision making skills of the physician of a certain diagnosis based on the automated data processing. Various groups working in X-ray mammography, CT scan, MRI imaging has shown that the specificity and sensitivity of the diagnostics improves with use of computer aided diagnosis.

With technological advances seen in OCT imaging with respect to ultra-high resolution imaging, real time data processing and endoscopic OCT, the implementation of different problem specific computer aided diagnostic schemes could aid in use of OCT imaging for clinical applications. First step in this bid requires use of computational methods to extract optical parameters like scattering coefficient, refractive indices, etc. The whole implementation process is tissue specific as well as dependent on the feature of interest and varies from one diagnostic problem to other.

4.5. OCT in tissue engineering:

Although OCT came to forefront as an imaging tool for transparent tissues, its utility had been extended for non-transparent, soft and hard tissues (Drexler & Fujimoto, 2008). OCT provides added advantage over the limited imaging depth and need for exogeneous fluorescent probe in optical imaging modality of confocal microscopy, traditionally used for monitoring tissue engineered constructs. Even though, application of OCT in tissue engineering is relatively recent, a few studies have been reported with conventional as well as functional modality of OCT. Dunkers *et al.* has reported on a dual mode technique of using optical coherence microscopy with fluorescence microscopy to image osteoblasts cultured in polymeric tissue engineered medical products (Dunkers *et al.*, 2003). Monitoring cytochrome oxidase redox changes gives an indication of the viability of the tissue. Yang *et al.* have shown qualitative shifts in the oxidation states in rat bone periosteal cells in explanted culture using OCT (Xu *et al.*, 2003). The potential application of OCT in imaging tissue engineered constructs in bioreactors *in-situ* as well as 3D constructs is reported in several references (Mason *et al.*, 2004b; Tan *et al.*, 2006; Tan *et al.*, 2004; Xi *et al.*, 2004; Yang *et al.*, 2006). OCT as well as PS-OCT has been used for studying the collagen matrix organization in tissue engineered cartilage and tendon constructs (Bagnaninchi *et al.*, 2007).

Doppler OCT has been used to monitor laminar flow in blood vessel constructs in a bioreactor (Mason *et al.*, 2004a). Smith *et al.* have used a swept source based OCT system to monitor the formation of neo-epidermis on tissue engineered constructs (Smith *et al.*, 2010a; Smith *et al.*, 2010c).

4.6. Speckle texture analysis:

Texture based feature recognition and automation in image classification have been carried out in the image classification of satellite images, ultrasound images, SAR images for a long time. Texture is a inherent property of any surface or object or image. For any image such a satellite image, ultrasound image, photograph, microscope images as well as medical images have variations in their tone or intensity that represent the surface variations due to spatial deviations. Haralick *et al.* implemented textural statistics for image classification of satellite based land images as well as aerial photographs (Haralick *et al.*, 1973). Thijssen *et al.* have used texture analysis on ultrasound images of intraocular melanoma classification (Thijssen *et al.*, 1991). Basset *et al.* have used this technique to differentiate normal and cancerous prostate cells (Basset *et al.*, 1993). Kim *et al.* have used wavelet transform as well as second order texture analysis studies to characterize intramuscular fat content of beef cattle (Kim*, et al.*, 1998). Different types of texture anaylsis technique have been tried out on ultrasound data to classification and detection of ulcer (Li & Meng, 2009), breast tumors (Chang *et al.*, 2005; Liu *et al.*, 2010), atherosclerotic carotid plaques (Kyriacou *et al.*, 2009), etc. Texture based studies also have been carried out to differentiate tissue types in fluorescence (Atlamazoglou *et al.*, 2001) as well as light microscopic images (Yogesan *et al.*, 1996). Gossage *et al.* extended this approach of texture analysis to OCT based image classification (Gossage*, et al.*, 2003) for the first time. Their texture analysis was based on the variations in local OCT image intensity due to speckle patterns. Although different approaches are

available for statistical analysis of texture, they used second order statistics based on spatial gray-level dependency matrices (SGLDMs) (Conners & Harlow, 1980). Approach of Gossage *et al.* have yielded binary classification rates of 98.5% for mouse skin and 97.3% for testicular fat tissue images with some structural differences seen in OCT images of the two tissues by unaided eye. Whereas the classification rate was lower for abnormal lung tissue of mouse and normal tissue (64% and 88%), in which the OCT images revealed little structural differences between the two tissue types. They had also extended this approach towards classification of different concentrations of microsphere/gelatin tissue phantoms and collagen/bovine aortic endothelial cells tissue phantoms (Gossage*, et al.*, 2006).

In this study, the approach of the speckle texture analysis of the OCT images based on the statistics derived from SGLDMs to classify different concentrations of agar-IL solutions has been applied. Further on, the results obtained on extending this approach towards classification of melanoma cell lines in tissue engineered skin are also presented.

4.7. Spatial grey-level dependency matrices (SGLDMs):

For texture analysis of OCT images, the statistics derived from SGLDMs or co-occurrence matrices have been used. SGLDM quantifies the distribution of greyscale values of a image for a pixel with respect to its neighbouring pixels. Second order joint conditional probability, $s_\theta(i, j \mid d, \theta)$ yields the probability of finding a pixel with grey-scale value i at a distance d from pixel with grey-scale value j in the direction θ. Thus for any image used for texture analysis with 'L'grey-scale levels in the image, for a specified distance d and direction θ, a $L \times L$ dimension matrix can be created. Haralick *et al.* had proposed 14 measures from the textural statistics derived from SGLDM, from which 28 features could be extracted (Haralick*, et al.*, 1973). For this study, the textural analysis using SGLDMs as carried out by Gossage *et*

al. (Gossage*, et al.*, 2006; Gossage*, et al.*, 2003) has been followed in which the following SGLDM features for distance $d = 1$ pixel in directions $\theta = 0^o, 45^o, 90^o \,\&\, 135^o$ were calculated:

$$Energy = \sum_{i=0}^{L-1}\sum_{j=0}^{L-1}\left[s_\theta(i,j \mid d)\right]^2 \quad 4.1$$

$$Entropy = \sum_{i=0}^{L-1}\sum_{j=0}^{L-1}\left[s_\theta(i,j \mid d)\log(s_\theta(i,j \mid d))\right] \quad 4.2$$

$$Correlation = \frac{\sum_{i=0}^{L-1}\sum_{j=0}^{L-1}(i-\mu_x)(j-\mu_y)s_\theta(i,j \mid d)}{\sigma_x\sigma_y} \quad 4.3$$

$$Local-Homogeneity = \sum_{i=0}^{L-1}\sum_{j=0}^{L-1}\frac{1}{1+(i-j)^2}s_\theta(i,j \mid d) \quad 4.4$$

$$Inertia\,/\,Contrast = \sum_{i=0}^{L-1}\sum_{j=0}^{L-1}(i-j)^2 s_\theta(i,j \mid d) \quad 4.5$$

where $s_\theta(i,j \mid d)$ is the (i,j) the element of SGLDM, and

$$\mu_x = \sum_{i=0}^{L-1} i \sum_{j=0}^{L-1} s_\theta(i,j \mid d) \quad 4.6$$

$$\mu_y = \sum_{j=0}^{L-1} j \sum_{i=0}^{L-1} s_\theta(i,j \mid d) \quad 4.7$$

$$\sigma_x = \sum_{i=0}^{L-1}(i-\mu_x)^2 \sum_{j=0}^{L-1} s_\theta(i,j \mid d) \quad 4.8$$

$$\sigma_y = \sum_{j=0}^{L-1}(j-\mu_y)^2 \sum_{i=0}^{L-1} s_\theta(i,j \mid d) \quad 4.9$$

The five features obtained from SGLDM matrix quantify the grey-scale intensity distribution in any image. Lamouche *et al.* has reported on the dependence of speckle size on the tissue microstructure or the effective number of scatterers in the tissue sample focal volume being imaged (Lamouche *et al.*, 2008). Hence the textural variations occurring due to the speckle size variations could be quantified based on the five textural statistical measures based on the SGLDMs used in this thesis. Homogeneous images have high values of energy whereas the log term in entropy leads to high value of entropy for inhomogeneous images. Local homogeneity gives more emphasis to low local contrast among neighbouring pixels while inertia or contrast gives high values for higher contrast of grey-level values among the neighbouring pixels. Correlation defines the degree of grey-level dependency or correlation among the pixel pairs. A total of 5 SGLDM features in 4 directions at unit pixel distance give a total of 20 features for a particular region of interest. These were calculated using the customized functions in Image processing toolbox of matlab™, which calculates the features using normalized SGLDM matrix so that sum of its elements equal to unity. These features were applied to a classification algorithm based on Mahalanobis distance. Mahalanobis distance d_M is a metric that is used to define the proximity an unknown sample set has got with the known classes. It is calculated from the covariance matrix, Σ as:

$$d_M = \sqrt{(x-\mu)^T \Sigma^{-1} (x-\mu)} \qquad 4.10$$

where, x is the feature vector and μ is the mean feature vector of the known class with respect to which the Mahalanobis distance is calculated for the feature set x. The covariance matrix, Σ is calculated as $\Sigma_{ij} = E[(x_i - \mu_i)(x_j - \mu_j)]$, where E denotes the expected value. Mahalanobis distance calculation is carried out by function 'mahal' in Matlab. Receiver operating characteristics (ROC) curves are then plotted to quantify how good the

classification has been with respect to these speckle texture features chosen (Cardillo, 2008). ROC curves are the most widely used predictive analysis tool in medical tests to assess the accuracy of the outcomes of the predictive models (Bewick *et al.*, 2004). Two parameters upon which ROC curve is based are sensitivity and specificity. In a binary classification, ROC curve determines how good a classification is. In a binary classifier, the possible outcomes fall into two class: True (T) and False (F), which has four possible outcomes during classification. True positive (TP) when actual value is T and predicted outcome falls into T. False positive (FP) when actual value is F and predicted outcome falls into T. False negative (FN) when actual value is T and predicted outcome falls into N. True negative (TN) when actual value as well as predicted outcome is N. This is formulated into a matrix called confusion matrix given as follows:

		Actual Value	
		T	**F**
Predicted Outcome	**T**	True Positive	False Positive
	F	False Negative	True Negative

Figure 4.2: The outcomes in binary classification that defines the confusion matrix

To draw a ROC curve, the true positive rate (TPR) and false positive rate (FPR) is given by:

$$TPR = \frac{TP}{TP + FN} \tag{4.11}$$

$$FPR = \frac{FP}{FP + TN} \tag{4.12}$$

Sensitivity of the binary classification is equivalent to TPR and specificity is given by 1-FPR. A ROC curve is TPR versus FPR curve or sensitivity versus 1-specificity curve. A 45^{o} line along the space is a line of no discrimination which represents a total random guess in a classification. The ROC space above this point represents a good classification. ROC curve gives the plot of how good a binary classification is with respect to a threshold that defines the line of division of the two classes. The point $(0,1)$ in the ROC space corresponds to perfect classification (Figure 4.3).

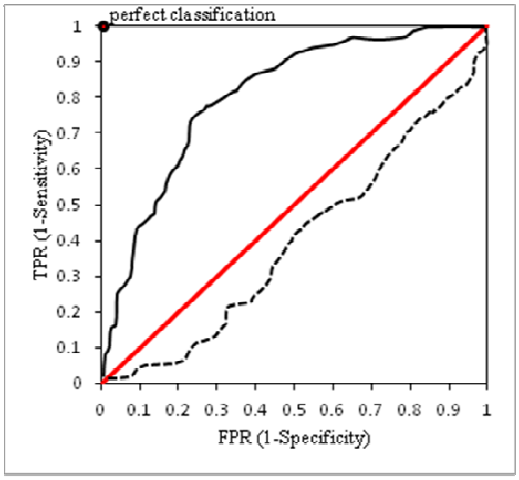

Figure 4.3: Some typical ROC curves. Top right corner represents perfect classification. The red line is line of no discrimination which implies the classification obtained is totally random. A curve (solid black line) in the space above the red line represents a good classification. Further the distance of the curve in the upper half of the space better the classification. A curve below the line of no discrimination (dash) represents a classification scheme with negative predictive power. Its predition power has to be reversed in order to obtain a mirror image curve above the line of no discrimination to obtain a good classification.

4.8. Experimental details and results:

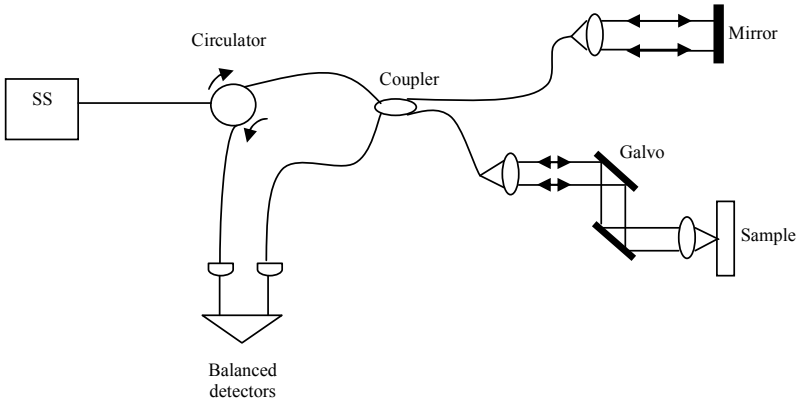

Figure 4.4: Schematic of the swept source based OCT experimental set-up used for the speckle texture analysis study of OCT images.

The OCT system used for this study is a swept source based system custom built in our lab from the commercial products obtained from Michelson Diagnostics Ltd. (Kent), UK (Figure 4.4). The system incorporates a swept laser source (HSL 2000-10-MDL, Santec, Japan) centred at a wavelength of 1315nm with full width of half maximum (FWHM) of 128nm. With a wavelength sweep rate of 10kHz, duty cycle of 60%, average output power 10mW and peak power around 23mW, the system has an axial resolution of 10μm in air. The signals are acquired at 20Ms/s and 14 bit resolution with the M2i.4022, Spectrum GmbH, Germany. The lateral resolution of the system is defined by Thorlabs LSM03-5X OCT scan lens of focal length f = 36mm giving a mean spotsize of 25μm defined as $1/e^2$ beam diameter in the field of focus.

Tissue phantoms that mimic the optical properties of biological tissues were used to initially test the algorithms and to provide as initial reference study for our speckle texture analysis. Intralipid is the most popular liquid phantom used in laboratories and has been well characterized for optical imaging studies (Flock *et al.*, 1992; van Staveren *et al.*, 1991). Also, previous studies have found that 2% Intralipid would prove to be a suitable skin phantom at

wavelengths below 1900nm (Troy & Thennadil, 2001). For this study, agar, a solid phantom commonly used for tissue-phantom calibration related experiments, with different concentrations of Intralipid, which is shown to be a homogeneous phantom for optical imaging studies (Cubeddu *et al.*, 1997) was used. Intralipid 10% stock solutions were diluted to 1%, 2%, 4% and 5% of weight by volume concentrations of Intralipid in agar solution (1ml). OCT images obtained for various concentrations of agar-IL solutions are as shown in Figure 4.5 and their corresponding reflectivity profiles in dB are plotted in Figure 4.6.

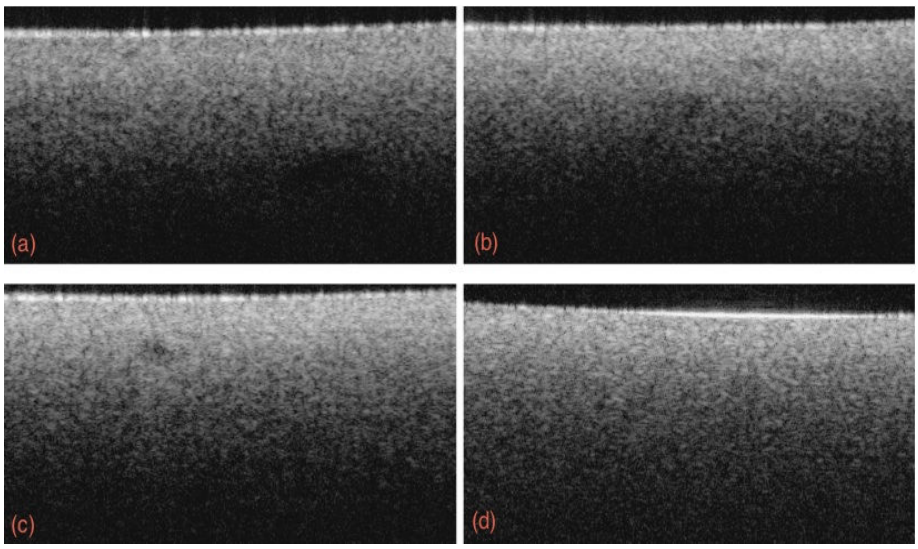

Figure 4.4: OCT images obtained for Intralipid 10% stock solution diluted to (a) 1% (b) 2% (c) 4% and (d) 5% of weight by volume concentrations in agar solution.

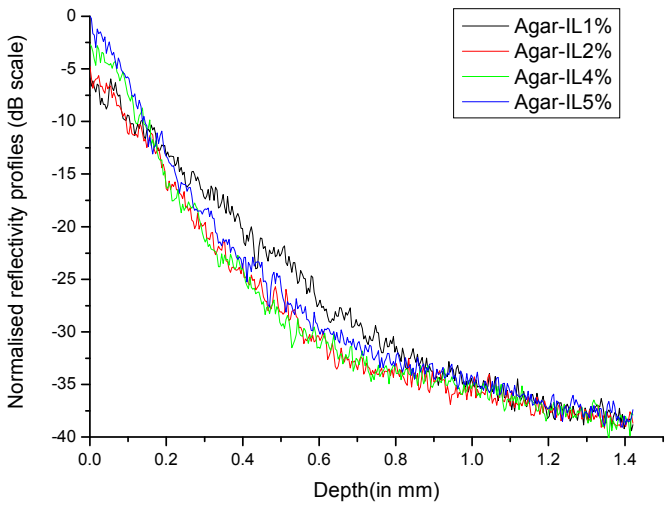

Figure 4.6: Corresponding reflectivity profiles expressed in dB obtained from OCT images for different concentrations of agar-IL solutions.

Tissue-engineered skin used in this study was produced using de-epithelialized dermis (DED). The 3D reconstructed skin models are used to study the melanoma invasion and the interactions occurring between the skin cells and the tumor cells which includes the invasion of tumor cells into the dermal region. Smith *et al.* described the detailed procedure used for harvesting keratinocytes and dermal fibroblasts for the production of reconstructed skin (Smith*, et al.*, 2010a). Three different types of human metastatic melanoma cell-lines have been used for textural studies. (a) HBL (b) A375-SM and (c) C8161. Eves *et al.* gives the detailed procedures and description of human melanoma cell cultures and their invasion into reconstructed skin (Eves *et al.*, 2003). Eves *et al.,* have also reported on the differences in the nature of the tumor invasion of these three cell lines based on 3D reconstructed human skin model. OCT has been shown to be a useful tool to monitor the differentiation process of the tissue-engineered skin (Schmitt *et al.*, 2010; Smith*, et al.*, 2010a; Smith *et al.*, 2010b). For

our speckle textural studies, OCT imaging was carried out on the first day of the cell culture as well as after three weeks of cell culture (Day 22).

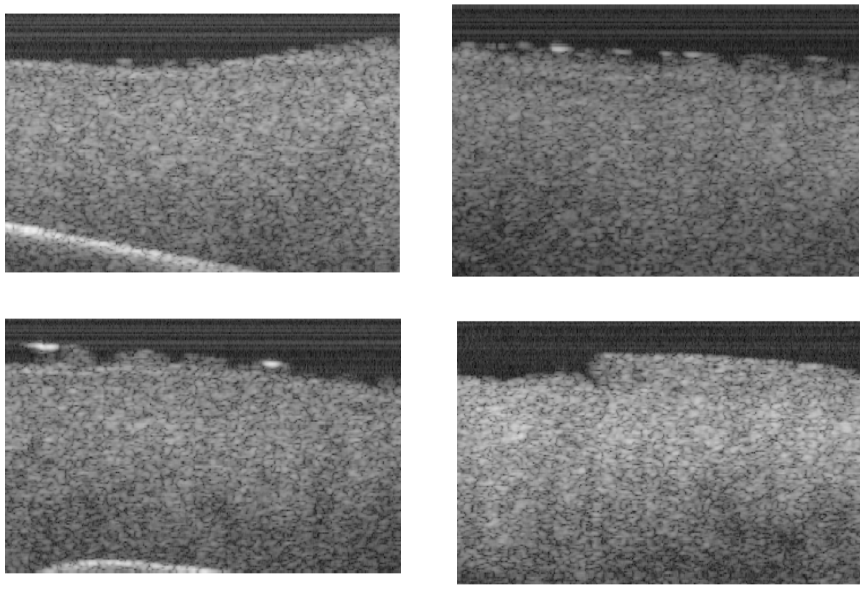

Figure 4.7: OCT images of the tissue engineered skin cultured with different melanoma cell lines. (a) A375-SM (b) C8161 (c) HBL (d) normal reconstructured skin, imaged on Day1 of the cell culture.

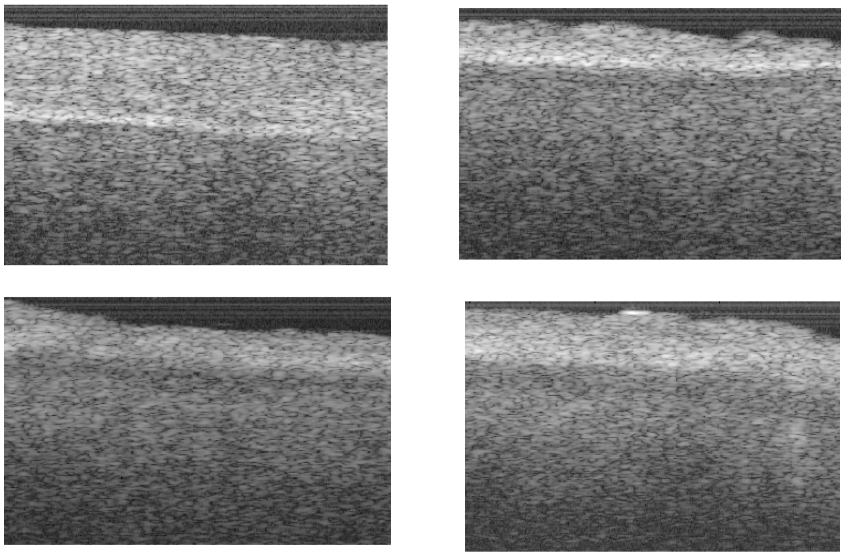

Figure 4.8: OCT images of the tissue engineered skin cultured with different melanoma cell lines. (a) A375-SM (b) C8161 (c) HBL (d) normal reconstructured skin, imaged on Day 22 of the cell culture.

Corresponding OCT images are shown in Figure 4.7 & Figure 4.8, respectively. Comparing the histological sections with the obtained OCT images of tissue-engineered skin growth after a period of 3 weeks, Smith *et al.* has proposed the light and dark region as seen in Figure 4.8 as the dermal-epidermal junction (Smith, *et al.*, 2010a). Although distinctive layers of epidermis could not be established in tissue-engineered skin based on OCT images, the growth of the epidermis as revealed by a layer of tissue with different optical properties than the underlying layer in the cultured skin samples are substantiated by the histology images in Figure 4.9.

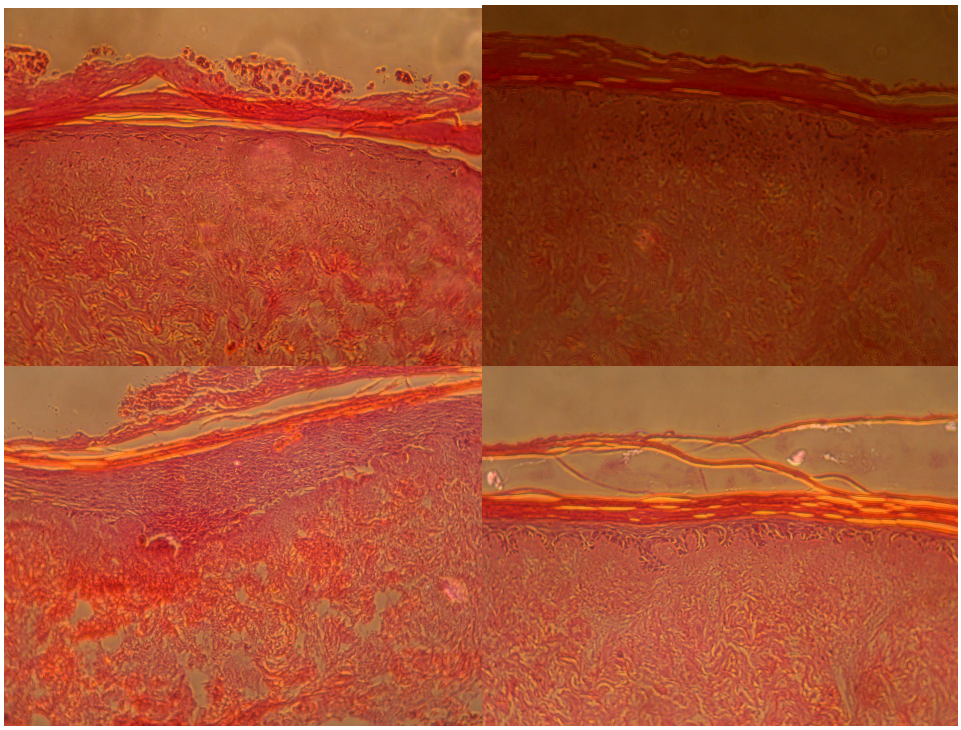

Figure 4.9: H&E stained histology images of melanoma invaded reconstructed skin (a) A375-SM (b) C8161 (c) HBL (d) normal reconstru ctured skin, imaged on Day 22 of the cell culture. (Photo courtesy Dr. Louise Smith)

While carrying out the OCT imaging of these samples, due care was taken to image the sample at the same depth in the focal plane and system parameters so as to have uniform imaging conditions throughout the images obtained for speckle texture analysis. However, this requirement could not be strictly followed during imaging of the growth of the melanoma invasion in the tissue engineered skin which was monitored after a gap of three weeks. The OCT images obtained using the swept source OCT system were 512×1250 pixel dimensions over optical depth of 2mm and lateral scan width of 5mm which gives the pixel size of 4μm by 4μm. Thus, the pixel resolution available was well below the system resolution of the OCT system. Also the OCT lateral scans were averaged over 5 A-scans as well as an averaging filter (default 3×3 averaging filter in Matlab^{TM}) been applied to reduce the random noise. Intensity valued were expressed in dB and scaled by normalizing the values over grayscale of 0-255, which represent the 8-bit grayscale image level scale. The texture analysis equations used for this study has been detailed in Section 4.6. Region of interests (ROI) were manually selected from the OCT images, which was a thin strip of image falling in the region of focal depth, 64 pixels wide. For the texture analysis of skin data, ROIs were separately chosen from dermal and epidermal region of the skin images because of the difference in the optical properties shown by these regions along the depth of the tissue (Figures 4.7 & 4.8). This is illustrated in Figure 4.10.

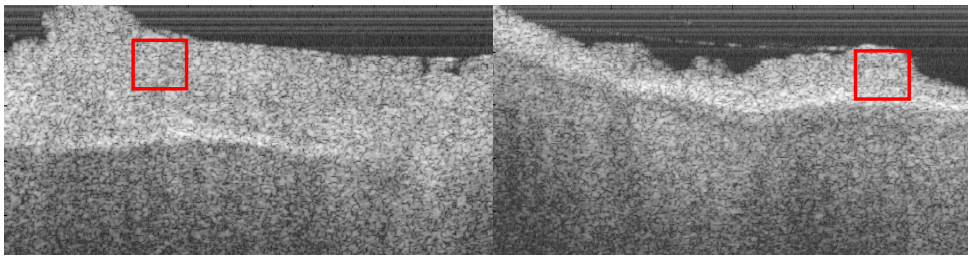

Figure 4.10: A representation of a typical 64×64 pixels region chosen in the ROI chosen in the epidermis region. Note the variations in the thickness of the epidermal growth layer in the two images.

From these chosen ROIs, 10 overlapping regions of dimension 64×64 pixels were chosen to carry out the texture related feature calculations as outlined in Section 4.6. 20 different features were obtained from SGLDMs obtained from the ROI which include features like entropy, energy, correlation, local homogeneity and inertia over 4 different directions of pixel specified by $\theta = 0^o, 45^o, 90^o$ and 135^o for a distance of $d = 1$ pixel. ROIs were manually selected and the analysis was carried out using Matlab^{TM}. This scheme follows the speckle texture analysis used by Gossage *et al.* to obtain statistically significant classification for binary classification of different types of tissues (Gossage*, et al.*, 2003) and also for various endothelial cell concentration and different sizes and concentrations of microspheres (Gossage*, et al.*, 2006).

The specificity and sensitivity of the binary classification scheme is understood by plotting the ROC curves by varying Mahalanobis distance as the discrimination threshold. For the speckle texture analysis study carried out here, the ROC curves are plotted to obtain a correct classification for separating sample of a particular concentration from the whole sample set. In order to reduce the number of features for classification, features with low coefficient of correlation were chosen (Lingley-Papadopoulos*, et al.*, 2008) which reduces the 20 feature set down to 10 giving a possible 120 combinations for 3-feature based classification. Homogeneity and contrast were the most common features that topped in the classification schemes used. Figure 4.11 and 4.12 show the 3-feature set clustering obtained for agar-IL samples of different concentrations. Clustering is quite distinct for lower concentrations of agar-IL samples (1% and 2%). This clustering nature attributes a closeness of the feature set to the scatterer density involved in the samples. This requires further scattering studies on

theoretical aspects to confirm the nature of dependency between the set of speckle statistical features and the scatterer density.

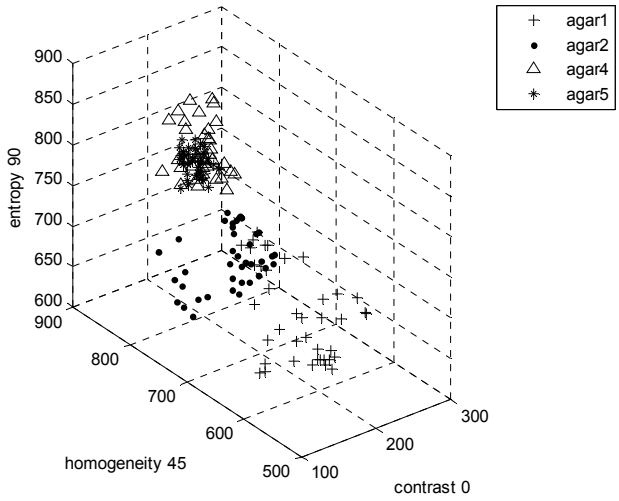

Figure 4.11: 3D scatter plot obtained for 3-feature set of entropy at 90^o, homogeneity at 45^o and contrast at 0^o obtained after speckle texture analysis of OCT images of different concentrations of agar-IL solutions.

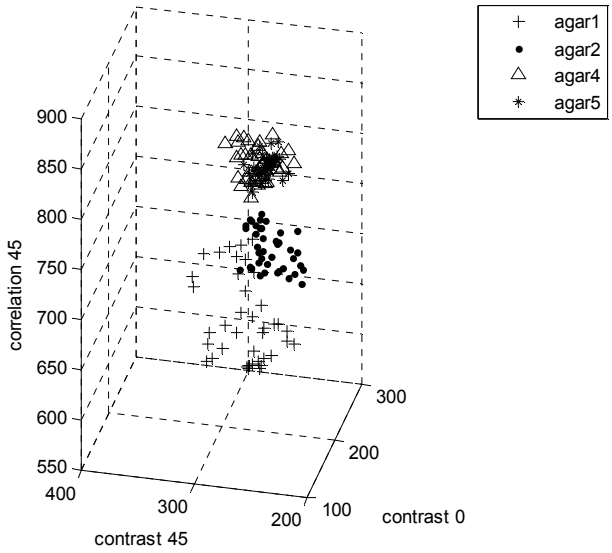

Figure 4.12: 3D scatter plot obtained for 3-feature set of contrast at 45^o, correlation at 45^o and contrast at 0^o obtained after speckle texture analysis of OCT images of different concentrations of agar-IL solutions.

Figure 4.13(a)-(d) shows the ROC curve obtained for correct classification of 1%, 2%, 4%, 5% Agar-IL sample, respectively from the whole of sample set for one of choice of a set of 3 feature classification that could be carried out among the 120 possible combinations. Farther away, the ROC curve is from the discrimination line better is the correct classification rate. Although Figure 4.13 shows one ROC curve out of the possible 120 combinations, the general trend shows a higher classification rate for 1% compared to rest of the concentrations in the whole set, which is also highly evident from the scatter plot. Following this, similar procedure of classification was tried using 3-feature set in an attempt to correctly classify normal reconstructed tissue engineered skin from those with melanoma invasion by choosing two separate ROIs epidermal region and dermal region.

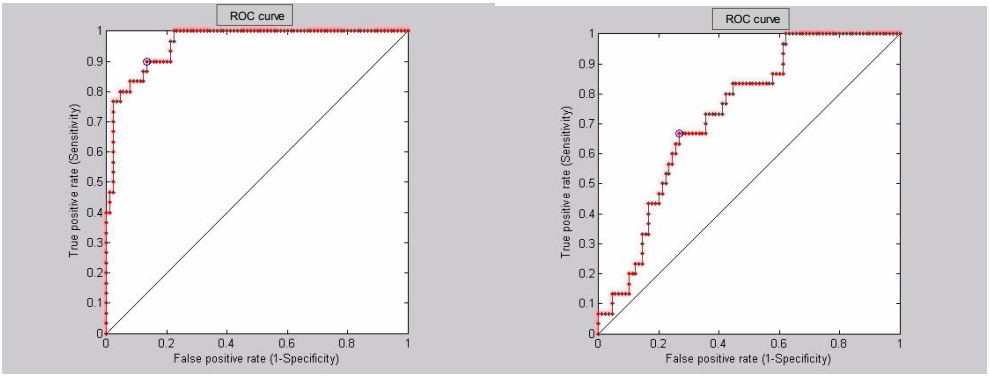

(a)

(b)

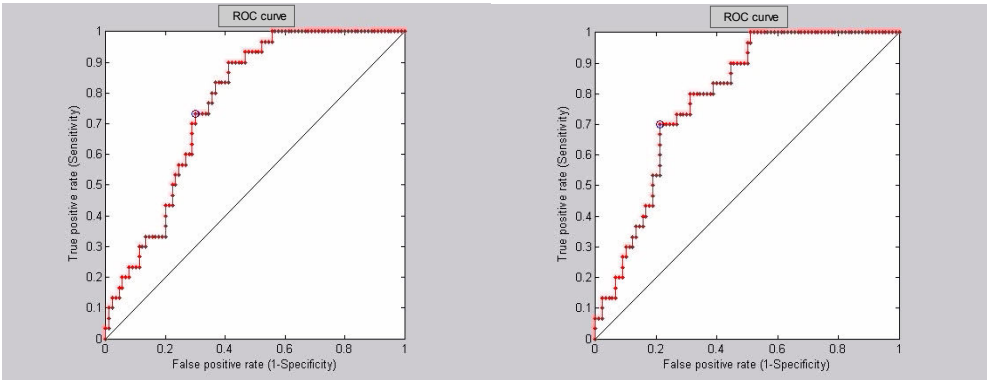

(c)

(d)

Figure 4.13(a)-(d): ROC curves obtained for classification of the sample set from the whole set (a) Agar-intralipd 1% solution sample set (b) Agar-intralipd 2% solution sample set (c) Agar-intralipd 4% solution sample set (d) Agar-intralipd 5% solution sample set

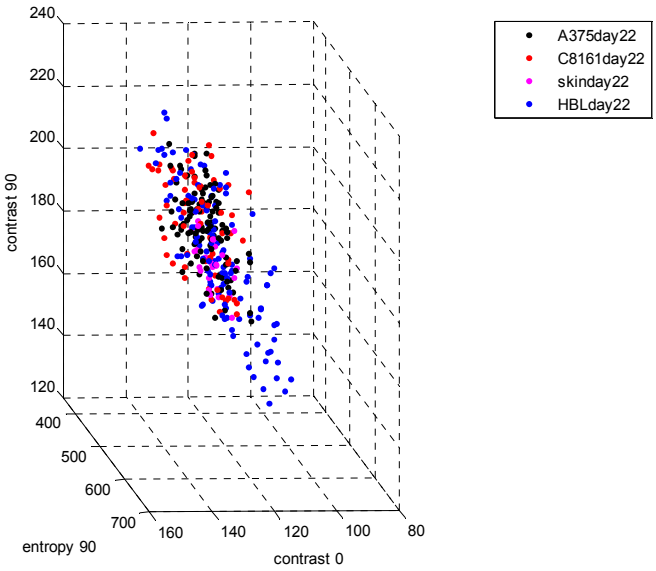

Figure 4.14: 3D scatter plot obtained for 3-feature set of contrast at 90^o, entropy at 90^o and contrast at 0^o obtained after speckle texture analysis of OCT images on epidermal growth layer on the tissue engineered normal skin and those with different melanoma cell lines.

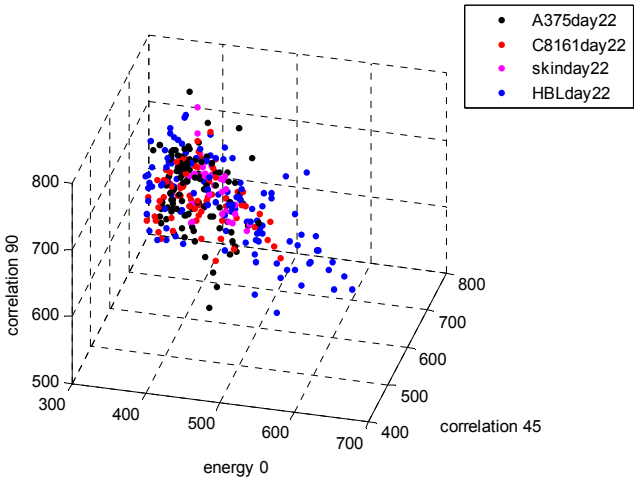

Figure 4.15: 3D scatter plot obtained for 3-feature set of energy at 0^o, correlation at 90^o and correlation at 45^o obtained after speckle texture analysis of OCT images on epidermal growth layer on the tissue engineered normal skin and those with different melanoma cell lines.

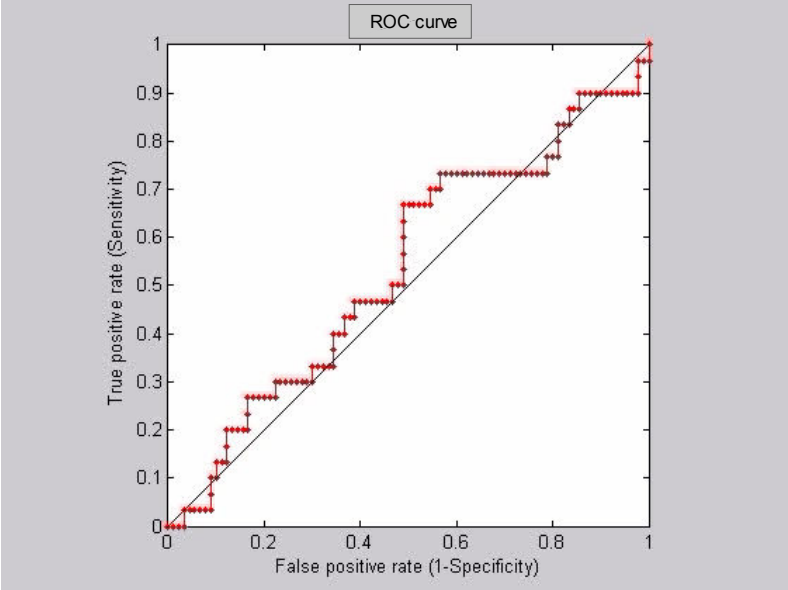

Figure 4.16: ROC curves obtained for classification of the normal reconstructed skin from the whole data set including normal reconstructed skin and melanoma invaded tissue engineered skin as imaged on Day 22 of the growth of the tissue.

Figures 4.14 and 4.15 show the 3-feature set scatter plot for the 3 melanoma cell lines in tissue engineered skin and normal reconstructed skin, although no visible distinctive behavior is noticed between the four data samples in scatter plot as compared to clustering of features seen in Figure 4.11 and 4.12. The graphs reveal that SGLDM based feature selection process based on speckle texture analysis of OCT images have not been successful in the automated classification of either different types of melanoma invasion on tissue engineered skin from one another or melanoma invaded skin types from the normal reconstructed skin. Figure 4.16 shows the ROC classification curve obtained for correctly identifying normal skin from a data set of normal skin and tissue engineered skin with different melanoma cell lines. This clearly substantiates the results revealed in Figures 4.14 and 4.15 owing to the closeness of the ROC curve to the discrimination line.

4.9: Conclusions and further scope of study

Statistical analysis of the information obtained from sub-resolution tissue surface based on the texture analysis of the speckles formed in the OCT images have been carried out in this study. Initially, this study was used for computer based classification of the OCT images obtained for agar-IL solutions of various concentrations. This was carried out based on the feature extraction and analysis based on SGLDMs obtained from OCT images. Scatter plots and ROC curves plotted reveal the ability of this statistical technique based on speckle texture analysis to correctly classify the tissue phantoms of different density of scatterers. However, the extension of this technique towards computer based classification of different types of melanoma cell lines from each other as well as of the normal reconstructed skin from the melanoma types as monitored using our OCT system for a period of over three weeks failed to produce a positive result towards correct classification. Although, OCT imaging could be potentially used to monitor the growth of epidermis onto tissue engineered skin (Smith*, et al.*, 2010a), the speckle based analysis to understand the changes in the optical properties of the tissue layers in reconstructed skin and with melanoma cell line invasion (C8161, A375-SM, HBL) and to implement this in computer based tissue discrimination algorithm was not quite successful. Further investigation into the dependency of speckle formation of the focal depth of imaging as well as other system parameters such as spatial resolution would have to be carried out to throw further light into this investigation. As shown by earlier investigators, system parameters do have a strong relation to the speckle 'noise' obtained (Gossage*, et al.*, 2006; Schmitt*, et al.*, 1999). However, during the three week over with the growth of tissue engineered skin was monitored, the system parameters would not have been fairly the same throughout. Also, the inherent biological variations occurring over the thickness of the epidermal growth could also change the relative signal

properties obtained in OCT image for the layers underneath it. Another issue with this texture-based analysis is that the optimal choice of feature set and implementation over classification is problem-specific which needs further study to establish this technique as a genuine candidate towards automated data classification of OCT images of wide range of tissues and pathologies.

4.10: References

Atlamazoglou, V., Yova, D., Kavantzas, N., & Loukas, S. (2001). Texture analysis of fluorescence microscopic images of colonic tissue sections. *Medical & Biological Engineering & Computing, 39*(2), 145-151.

Bagnaninchi, P. O., Yang, Y., Zghoul, N., Maffulli, N., Wang, R. K., & Haj, A. J. (2007). Chitosan microchannel scaffolds for tendon tissue engineering characterized using optical coherence tomography. *Tissue Engineering, 13*(2), 323-331.

Barton, J. K., & Stromski, S. (2005). Flow measurement without phase information in optical coherence tomography images. *Optics Express, 13*(14), 5234-5239.

Basset, O., Sun, Z., Mestas, J. L., & Gimenez, G. (1993). Texture analysis of ultrasonic images of the prostate by means of co-occurrence matrices. *Ultrason Imaging, 15*(3), 218-237.

Bazant-Hegemark, F., & Stone, N. (2009). Towards automated classification of clinical optical coherence tomography data of dense tissues. *Lasers Med Sci, 24*(4), 627-638.

Bewick, V., Cheek, L., & Ball, J. (2004). Statistics review 13: Receiver operating characteristic curves. *Critical Care, 8*(6), 508-512.

Briers, J. D. (2001). Laser Doppler, speckle and related techniques for blood perfusion mapping and imaging. *Physiological Measurement, 22*(4), R35-66.

Cardillo, G. (Producer). (2008). ROC curve: compute a Receiver Operating Characteristics curve.

Chang, R. F., Wu, W. J., Moon, W. K., & Chen, D. R. (2005). Automatic ultrasound segmentation and morphology based diagnosis of solid breast tumors. *Breast Cancer Research and Treatment, 89*(2), 179-185.

Conners, R. W., & Harlow, C. A. (1980). A Theoretical Comparison of Texture Algorithms. *Ieee Transactions on Pattern Analysis and Machine Intelligence, 2*(3), 204-222.

Cubeddu, R., Pifferi, A., Taroni, P., Torricelli, A., & Valentini, G. (1997). A solid tissue phantom for photon migration studies. *Phys Med Biol, 42*(10), 1971-1979.

Dainty, J. C. (1984). Laser speckle and related phenomena. *Appl Opt, 23*(16), 2661.

DeBuc, D. C. (Ed.). (2011). *A Review of Algorithms for Segmentation of Retinal Image Data Using Optical Coherence Tomography*: InTech.

Drexler, W., & Fujimoto, J. G. (Eds.). (2008). *Optical Coherence Tomography : Technology and Applications*. Berlin Heidelberg: Springer.

Drexler, W., Morgner, U., Ghanta, R. K., Kartner, F. X., Schuman, J. S., & Fujimoto, J. G. (2001). Ultrahigh-resolution ophthalmic optical coherence tomography. *Nat Med, 7*(4), 502-507.

Drexler, W., Morgner, U., Kartner, F. X., Pitris, C., Boppart, S. A., Li, X. D. (1999). In vivo ultrahigh-resolution optical coherence tomography. *Opt Lett, 24*(17), 1221-1223.

Duncan, D. D., & Kirkpatrick, S. J. (2008). Can laser speckle flowmetry be made a quantitative tool? *J Opt Soc Am A, 25*(8), 2088-2094.

Dunkers, J. P., Cicerone, M. T., & Washburn, N. R. (2003). Collinear optical coherence and confocal fluorescence microscopies for tissue engineering. *Optics Express, 11*(23), 3074-3079.

Eves, P., Katerinaki, E., Simpson, C., Layton, C., Dawson, R., Evans, G. (2003). Melanoma invasion in reconstructed human skin is influenced by skin cells--investigation of the role of proteolytic enzymes. *Clin Exp Metastasis, 20*(8), 685-700.

Fankhauser, F., & Kwasniewska, S. (Eds.). (2003). *Lasers in Opthalmology: Basic, Diagnostic and Surgical Aspects: A Review*. The Hague: Kugler Publications.

Fercher, A. F., Drexler, W., Hitzenberger, C. K., & Lasser, T. (2003). Optical coherence tomography - principles and applications. *Reports on Progress in Physics, 66*(2), 239-303.

Flock, S. T., Jacques, S. L., Wilson, B. C., Star, W. M., & van Gemert, M. J. (1992). Optical properties of Intralipid: a phantom medium for light propagation studies. *Lasers Surg Med, 12*(5), 510-519.

Gossage, K. W., Smith, C. M., Kanter, E. M., Hariri, L. P., Stone, A. L., Rodriguez, J. J. (2006). Texture analysis of speckle in optical coherence tomography images of tissue phantoms. *Physics in Medicine and Biology, 51*(6), 1563-1575.

Gossage, K. W., Tkaczyk, T. S., Rodriguez, J. J., & Barton, J. K. (2003). Texture, analysis of optical coherence tomography images: feasibility for tissue classification. *Journal of Biomedical Optics, 8*(3), 570-575.

Haralick, R. M., Shanmuga.K, & Dinstein, I. (1973). Textural Features for Image Classification. *IEEE Transactions on Systems Man and Cybernetics, Smc3*(6), 610-621.

Hillman, T. R., Adie, S. G., Seemann, V., Armstrong, J. J., Jacques, S. L., & Sampson, D. D. (2006). Correlation of static speckle with sample properties in optical coherence tomography. *Optics Letters, 31*(2), 190-192.

Hillman, T. R., Curatolo, A., Kennedy, B. F., & Sampson, D. D. (2010). Detection of multiple scattering in optical coherence tomography by speckle correlation of angle-dependent B-scans. *Optics Letters, 35*(12), 1998-2000.

Kim, N., Amin, V., Wilson, D., Rouse, G., & Udpa, S. (1998). Ultrasound image texture analysis for characterizing intramuscular fat content of live beef cattle. *Ultrasonic Imaging, 20*(3), 191-205.

Kyriacou, E., Pattichis, M. S., Pattichis, C. S., Mavrommatis, A., Christodoulou, C. I., Kakkos, S. (2009). Classification of atherosclerotic carotid plaques using morphological analysis on ultrasound images. *Applied Intelligence, 30*(1), 3-23.

Lamouche, G., Bisaillon, C. E., Vergnole, S., & Monchalin, J. P. (2008). On the speckle size in optical coherence tomography - art. no. 684724. *Coherence Domain Optical Methods and Optical Coherence Tomography in Biomedicine XII, 6847*, 84724-84724.

Li, B. P., & Meng, M. Q. H. (2009). Texture analysis for ulcer detection in capsule endoscopy images. *Image and Vision Computing, 27*(9), 1336-1342.

Lingley-Papadopoulos, C. A., Loew, M. H., Manyak, M. J., & Zara, J. M. (2008). Computer recognition of cancer in the urinary bladder using optical coherence tomography and texture analysis. *Journal of Biomedical Optics, 13*(2).

Liu, B., Cheng, H. D., Huang, J. H., Tian, J. W., Tang, X. L., & Liu, J. F. (2010). Fully automatic and segmentation-robust classification of breast tumors based on local texture analysis of ultrasound images. *Pattern Recognition, 43*(1), 280-298.

Manyak, M., Lingley-Papadopoulos, C., Loew, M., & Zara, J. (2007). Computer recognition of bladder cancer with optical coherence tomography and texture analysis. *Journal of Endourology, 21*, A30-A30.

Mariampillai, A., Standish, B. A., Moriyama, E. H., Khurana, M., Munce, N. R., Leung, M. K. K. (2008). Speckle variance detection of microvasculature using swept-source optical coherence tomography. *Optics Letters, 33*(13), 1530-1532.

Mason, C., Markusen, J. F., Town, M. A., Dunnill, P., & Wang, R. K. (2004a). Doppler optical coherence tomography for measuring flow in engineered tissue. *Biosensors & Bioelectronics, 20*(3), 414-423.

Mason, C., Markusen, J. F., Town, M. A., Dunnill, P., & Wang, R. K. (2004b). The potential of optical coherence tomography in the engineering of living tissue. *Physics in Medicine and Biology, 49*(7), 1097-1115.

Pan, Y. T., Birngruber, R., Rosperich, J., & Engelhardt, R. (1995). Low-Coherence Optical Tomography in Turbid Tissue - Theoretical-Analysis. *Applied Optics, 34*(28), 6564-6574.

Schmitt, J. M., & Kumar, G. (1996). Turbulent nature of refractive-index variations in biological tissue. *Optics Letters, 21*(16), 1310-1312.

Schmitt, J. M., Xiang, S. H., & Yung, K. M. (1999). Speckle in optical coherence tomography. *Journal of Biomedical Optics, 4*(1), 95-105.

Schmitt, R., Marx, U., Walles, H., & Heymer, A. (2010). Optical Coherence Tomography Investigation of Growth Cycles of Engineered Skin Tissue. *Optics in Tissue Engineering and Regenerative Medicine IV, 7566*(19).

Smith, L. E., Bonesi, M., Smallwood, R., Matcher, S. J., & MacNeil, S. (2010a). Using swept-source optical coherence tomography to monitor the formation of neo-epidermis in tissue-engineered skin. *Journal of Tissue Engineering and Regenerative Medicine, 4*(8), 652-658.

Smith, L. E., Lu, Z., Bonesi, M., Smallwood, R., Matcher, S. J., & MacNeil, S. (2010b). Using swept source optical coherence tomography to monitor wound healing in tissue engineered skin. *Optics in Tissue Engineering and Regenerative Medicine IV, 7566*(19).

Smith, L. E., Smallwood, R., & Macneil, S. (2010c). A Comparison of Imaging Methodologies for 3D Tissue Engineering. *Microscopy Research and Technique, 73*(12), 1123-1133.

Soh, L. K., & Tsatsoulis, C. (1999). Texture analysis of SAR sea ice imagery using gray level co-occurrence matrices. *IEEE Transactions on Geoscience and Remote Sensing, 37*(2), 780-795.

Strong, A. J., Bezzina, E. L., Anderson, P. J., Boutelle, M. G., Hopwood, S. E., & Dunn, A. K. (2006). Evaluation of laser speckle flowmetry for imaging cortical perfusion in experimental stroke studies: quantitation of perfusion and detection of peri-infarct depolarisations. *Journal of Cerebral Blood Flow & Metabolism, 26*(5), 645-653.

Tan, W., Oldenburg, A. L., Norman, J. J., Desai, T. A., & Boppart, S. A. (2006). Optical coherence tomography of cell dynamics in three-dimensional tissue models. *Optics Express, 14*(16), 7159-7171.

Tan, W., Sendemir-Urkmez, A., Fahrner, L. J., Jamison, R., Leckband, D., & Boppart, S. A. (2004). Structural and functional optical imaging of three-dimensional engineered tissue development. *Tissue Engineering, 10*(11-12), 1747-1756.

Thijssen, J. M. (2003). Ultrasonic speckle formation, analysis and processing applied to tissue characterization. *Pattern Recognition Letters, 24*(4-5), 659-675.

Thijssen, J. M., Verbeek, A. M., Romijn, R. L., de Wolff-Rouendaal, D., & Oosterhuis, J. A. (1991). Echographic differentiation of histological types of intraocular melanoma. *Ultrasound in Medicine and Biology, 17*(2), 127-138.

Touzi, R., Lopes, A., & Bousquet, P. (1988). A Statistical and Geometrical Edge Detector for Sar Images. *IEEE Transactions on Geoscience and Remote Sensing, 26*(6), 764-773.

Troy, T. L., & Thennadil, S. N. (2001). Optical properties of human skin in the near infrared wavelength range of 1000 to 2200 nm. *Journal of Biomedical Optics, 6*(2), 167-176.

Ulaby, F. T., Kouyate, F., Brisco, B., & Williams, T. H. L. (1986). Textural Information in Sar Images. *IEEE Transactions on Geoscience and Remote Sensing, 24*(2), 235-245.

van Staveren, H. J., Moes, C. J., van Marie, J., Prahl, S. A., & van Gemert, M. J. (1991). Light scattering in Intralipid-10% in the wavelength range of 400-1100 nm. *Applied Optics, 30*(31), 4507-4514.

Xi, C. W., Marks, D. L., Parikh, D. S., Raskin, L., & Boppart, S. A. (2004). Structural and functional imaging of 3D microfluidic mixers using optical coherence tomography. *Proceedings of the National Academy of Sciences of the United States of America, 101*(20), 7516-7521.

Xu, X. Q., Wang, R. K. K., & El Haj, A. (2003). Investigation of changes in optical attenuation of bone and neuronal cells in organ culture or three-dimensional constructs in vitro with optical coherence tomography: relevance to cytochrome oxidase monitoring. *European Biophysics Journal with Biophysics Letters, 32*(4), 355-362.

Yang, Y., Dubois, A., Qin, X. P., Li, J., El Haj, A., & Wang, R. K. (2006). Investigation of optical coherence tomography as an imaging modality in tissue engineering. *Physics in Medicine and Biology, 51*(7), 1649-1659.

Yogesan, K., Jorgensen, T., Albregtsen, F., Tveter, K. J., & Danielsen, H. E. (1996). Entropy-based texture analysis of chromatin structure in advanced prostate cancer. *Cytometry, 24*(3), 268-276.

CHAPTER 5

Results and Conclusions

5.1 Summary

This chapter summarises the research work carried out in the field of OCT in this thesis, which gives an overview of the results presented in the previous three chapters of this thesis work. A general overview of the range of research problems that have emerged from the insight gained by working on a quest to answer the research objectives set before the start of this study and the further studies that could be undertaken to establish fully the potential applications of the findings reported here.

5.2 Introduction

The study carried out in this thesis mainly focussed on extending the applications of OCT in the field of orthopaedics and tissue engineering further to attain the following three objectives

1. To extract depth-dependent 3D structural information of the collagen fibre orientation of articular cartilage using non-invasive technique of PS-OCT
2. To study the nature of angle-resolved backscattering differences obtained for tissues with different types of collagen fibrils using OCT
3. To study the feasibility of automated data classification of different types of melanoma invasion in tissue-engineered skin using OCT.

In the following sections, it is discussed in detail the extent of work carried out to fulfil these objectives, results obtained and inferred and the nature of further work to be carried out to establish the potential applications in the field of biomedical imaging as a spin-off from the results presented in this thesis work.

5.3 PS-OCT of articular cartilage

The main motivation behind carrying out this work is to establish PS-OCT as a non-invasive tool to extract 3D information of the orientation of the collagen fibre in articular cartilage tissues, with a potential application towards employing this study *in-vivo*. The work presented here is to the best of our knowledge, first of its kind towards a comparative study of experimental and theoretical approach towards extracting optic axis information from articular cartilage using PS-OCT. The feasibility of carrying out this work is shown here with two different implementations of PS-OCT systems: first system is a first generation time-domain based TD-PS-OCT system which follows a simple basic implementation of PS-OCT system although with a drawback of slow data acquisition owing to the mechanical moving delay line implementation in the reference arm of the interferometer as well as its bulk optics based implementation that seriously restricts its use in-vivo, second system is a recently developed version of PS-OCT which uses a sweeping laser source with the polarisation state of the incident light beam onto the system continuously modulated at a rate of 6.67MHz. Owing to the fact that the full fibre-based implementation of the set-up could not be carried out due to the occurrence of artefacts in birefringence analysis, the fact that detection arm has fully fibre-based implementation does not deter using this system for in-vivo studies.

A complete analysis employing a layered anisotropic model based on EJMC has been carried out with respect to analysing the experimental data obtained from TD-PS-OCT of articular cartilage. The technique implemented is to extract the structural orientation information from the apparent birefringence data as obtained from the phase retardance images obtained over multi-angle illumination imaging carried out on a selected site of the tissue. Employing a layered model based on the histological zones and inputting in the polar and azimuthal angle

orientation along the depth of the tissue, a visually good fit is obtained to 5 measurements of multi-angle PS-OCT data simultaneously. This implementation also involved including a noise model for TD-PS-OCT. The results led onto developing an inverse solution based on customised optimisation algorithms available in standard toolbox of Matlab. Although, employing two different optimiser algorithm together with a bootstrap Monte Carlo approach to estimating parameter accuracy yielded sensible looking fits to the experimental PS-OCT data, it opens up further research problems that requires further investigation with respect to the choice of input conditions given to optimiser as well as the formulation of the optimization problem itself.

In this study, it has been shown how EJMC based approach could be used to develop a theoretical framework to understand the depth dependent structural orientation properties of articular cartilage for a particular site chosen. It requires further investigation to report on the sensitivity of this approach towards studying the topographical variations seen across the tissue with respect to the thickness and structural orientation. Also, it would be a separate study on its own to try to investigate how EJMC based PS-OCT data extraction approach could have potential application to understanding and diagnosing different phases of osteoarthritis. Since this approach shows promise towards understanding depth-dependent information about any organised collagen fibre structures through phase retardance images non-invasively, it could have potential applications towards monitoring the growth of collagen based tissue-engineered scaffold.

With the study undertaken here, it is been shown for the first time how PS-OCT data could be used to understand the microstructure of articular cartilage, which is a topic of interest in the field of application of OCT in orthopaedics.

5.4 Angle-resolved backscattering

The motivation behind carrying out angle-resolved backscattering study to make a comparative study on tendon and articular cartilage is the previous works which has established low coherence interferometry based angle-resolved scattering as a method to study the changes in cell nuclei that aids in early stage diagnosis of dysplasia. The work was carried on the basis of a major difference in the nature and type of the collagen fibril organisation in tendon (Type I) and articular cartilage (Type II). The whole idea behind this study was to carry out a preliminary investigation towards implementing a simple non-invasive technique to understand the changes occurring during the different phases of osteoarthritis as well as cartilage repair process based on the change of the biomolecular and fibrillar arrangement during the process. The angle-resolved experimental technique is the same as that implemented in PS-OCT studies of articular cartilage, which is multi-angle incidence of tissue imaging in two orthogonal planes with respect to a surface normal. However, for this study, reflectivity profiles, as that would be obtained from a normal OCT system is used from the PS-OCT system based on the single scattering OCT model. The angle-resolved scattering profiles obtained for tendon and articular cartilage show a significant difference from one another with respect to the signal power drop obtained over oblique incidence. Tendon tissue reveals an anisotropic profile whereas articular cartilage reveals an isotropic distribution of scatterers based on the plots obtained. A simple fibril model based on RG scattering approximation was used to elucidate the results, which whilst providing general support to our initial assumption of differences in the nature and type of the scatterers involved in the tissue responsible for the difference in the angle-resolved plots obtained, is strictly not a complete analysis. As part of future work, a better 3D volumetric model explaining the results as well as an investigation towards application of this technique

towards non-invasive way of studying changes occurring during articular repair and different phases of osteoarthritis could have potential implications towards use of OCT in clinical applications in orthopaedics.

5.5 Speckle texture analysis

The motivation behind implementing a speckle based data classification scheme on tissue engineered skin come from the previous research works which reports a speckle texture analysis based binary classification of OCT images of different biological tissues and tissue phantoms with a reasonable level of specificity and sensitivity. SGDLM based statistical analysis based textural variations obtained for OCT images of tissue phantoms - different concentrations of agar-Intralipid solutions were tried initially and were successful towards obtaining a good classification scheme of separating the OCT images automatically based on the speckle textural algorithm. This was shown using the 3-feature set scatter plots, which revealed a degree of clusterness and distinction of the different concentrations of agar-Intralipid from one another. This has been further supported by ROC curves for binary classification of a particular data set from the whole sample set. This shows that although OCT as an imaging tool is unable to differentiate homogeneous and uniform looking sample types with different number of scatterer density involved, speckle texture analysis shows promising results towards differentiating tissue/phantom types based on the differences in the number of scatterers in the tissue phantom imaged. Speckle texture analysis has been shown to offer sub-OCT resolution information based on statistical measures implemented that determine the variations in the occurrence of speckle based on the change in the number of scatterers. Based on this initial success obtained with regard to speckle texture studies of tissue phantoms, a similar approach was implemented towards distinguishing normal skin composite from the different types of melanoma invasion in tissue engineered skin, with the

tissue culture and the growth of epidermis in the tissue engineered skin monitored using OCT over a period of 3 weeks. Probably owing to the fact that, over a period of 3 weeks, there was little control over uniformity of system parameters throughout the long period in which OCT imaging were carried out for this study. The variations occurring in the growth of epidermis in the tissue-engineered skin could also be a potential source of error. However, this study has highlighted the problem-specific nature of trying to implement a general computer based data automation tool.